

Chapter

3

Magnetic Methods

3.1. INTRODUCTION

3.1.1. General

Magnetic and gravity methods have much in common, but magnetics is generally more complex and variations in the magnetic field are more erratic and localized. This is partly due to the difference between the dipolar magnetic field and the monopolar gravity field, partly due to the variable direction of the magnetic field, whereas the gravity field is always in the vertical direction, and partly due to the time-dependence of the magnetic field, whereas the gravity field is time-invariant (ignoring small tidal variations). Whereas a gravity map usually is dominated by regional effects, a magnetic map generally shows a multitude of local anomalies. Magnetic measurements are made more easily and cheaply than most geophysical measurements and corrections are practically unnecessary. Magnetic field variations are often diagnostic of mineral structures as well as regional structures, and the magnetic method is the most versatile of geophysical prospecting techniques. However, like all potential methods, magnetic methods lack uniqueness of interpretation.

3.1.2. History of Magnetic Methods

The study of the earth's magnetism is the oldest branch of geophysics. It has been known for more than three centuries that the Earth behaves as a large and somewhat irregular magnet. Sir William Gilbert (1540–1603) made the first scientific investigation of terrestrial magnetism. He recorded in *de Magnete* that knowledge of the north-seeking property of a magnetite splinter (a *lodestone* or leading stone) was brought to Europe from China by Marco Polo. Gilbert showed that the Earth's magnetic field was roughly equivalent to that of a permanent magnet lying in a general north-south direction near the Earth's rotational axis.

Karl Frederick Gauss made extensive studies of the Earth's magnetic field from about 1830 to 1842, and most of his conclusions are still valid. He concluded from mathematical analysis that the magnetic field was entirely due to a source within the Earth, rather than outside of it, and he noted a probable connection to the Earth's rotation because the axis of the dipole that accounts for most of the field is not far from the Earth's rotational axis.

The terrestrial magnetic field has been studied almost continuously since Gilbert's time, but it was not until 1843 that von Wrede first used variations in the field to locate deposits of magnetic ore. The publication, in 1879, of *The Examination of Iron Ore Deposits by Magnetic Measurements* by Thalén marked the first use of the magnetic method.

Until the late 1940s, magnetic field measurements mostly were made with a magnetic balance, which measured one component of the earth's field, usually the vertical component. This limited measurements mainly to the land surface. The fluxgate magnetometer was developed during World War II for detecting submarines from an aircraft. After the war, the fluxgate magnetometer (and radar navigation, another war development) made aeromagnetic measurements possible. Proton-precession magnetometers, developed in the mid-1950s, are very reliable and their operation is simple and rapid. They are the most commonly used instruments today. Optical-pump alkali-vapor magnetometers, which began to be used in 1962, are so accurate that instrumentation no longer limits the accuracy of magnetic measurements. However, proton-precession and optical-pump magnetometers measure only the magnitude, not the direction, of the magnetic field. Airborne gradiometer measurements began in the late 1960s, although ground measurements were made much earlier. The gradiometer often consists of two magnetometers vertically spaced 1 to 30 m apart. The difference in readings not only gives the vertical gradient, but also, to a large extent, removes the effects of tempo-

ral field variations, which are often the limiting factor on accuracy.

Digital recording and processing of magnetic data removed much of the tedium involved in reducing measurements to magnetic maps. Interpretation algorithms now make it possible to produce computer-drawn profiles showing possible distributions of magnetization.

The history of magnetic surveying is discussed by Reford (1980) and the state of the art is discussed by Paterson and Reeves (1985).

3.2. PRINCIPLES AND ELEMENTARY THEORY

3.2.1. Classical versus Electromagnetic Concepts

Modern and classical magnetic theory differ in basic concepts. Classical magnetic theory is similar to electrical and gravity theory; its basic concept is that point magnetic poles are analogous to point electrical charges and point masses, with a similar inverse-square law for the forces between the poles, charges, or masses. Magnetic units in the centimeter-gram-second and electromagnetic units (cgs and emu) system are based on this concept. Système International (SI) units are based on the fact that a magnetic field is electrical in origin. Its basic unit is the dipole, which is created by a circular electrical current, rather than the fictitious isolated monopole of the cgs-emu system. Both emu and SI units are in current use.

The cgs-emu system begins with the concept of magnetic force \mathbf{F} given by Coulomb's law:

$$\mathbf{F} = (p_1 p_2 / \mu r^2) \mathbf{r}_1 \quad (3.1)$$

where \mathbf{F} is the force on p_2 , in dynes, the poles of strength p_1 and p_2 are r centimeters apart, μ is the magnetic permeability [a property of the medium; see Eq. (3.7)], and \mathbf{r}_1 is a unit vector directed from p_1 toward p_2 . As in the electrical case (but unlike the gravity case, in which the force is always attractive), the magnetostatic force is attractive for poles of opposite sign and repulsive for poles of like sign. The sign convention is that a positive pole is attracted toward the Earth's north magnetic pole; the term *north-seeking* is also used.

The magnetizing field \mathbf{H} (also called *magnetic field strength*) is defined as the force on a unit pole:

$$\mathbf{H}' = \mathbf{F}/p_2 = (p_1 / \mu r^2) \mathbf{r}_1 \quad (3.2)$$

(we use a prime to indicate that H is in cgs-emu

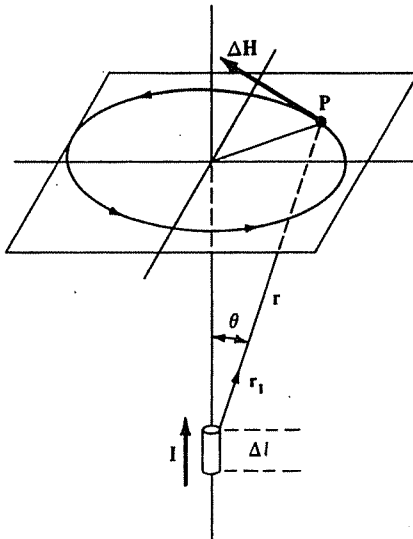


Figure 3.1. Ampère's law. A current I through a length of conductor Δl creates a magnetizing field ΔH at a point P :

$$\Delta H = (I \Delta l) \times r_1 / 4\pi r^2$$

where ΔH is in amperes per meter when I is in amperes and r and Δl are in meters.

units); H' is measured in oersteds (equivalent to dynes per unit pole).

A magnetic dipole is envisioned as two poles of strength $+p$ and $-p$ separated by a distance $2l$. The *magnetic dipole moment* is defined as

$$\mathbf{m} = 2lp\mathbf{r}_1 \quad (3.3)$$

\mathbf{m} is a vector in the direction of the unit vector \mathbf{r}_1 that extends from the negative pole toward the positive pole.

A magnetic field is a consequence of the flow of an electrical current. As expressed by Ampère's law (also called the Biot-Savart law), a current I in a conductor of length Δl creates, at a point P (Fig. 3.1), a magnetizing field ΔH given by

$$\Delta H = (I \Delta l) \times r_1 / 4\pi r^2 \quad (3.4)$$

where H has the SI dimension amperes per meter [$= 4\pi \times 10^{-3}$ oersted], r and Δl are in meters, I is in amperes, and ΔH , \mathbf{r}_1 , and $I \Delta l$ have the directions indicated in Figure 3.1.

A current flowing in a circular loop acts as a magnetic dipole located at the center of the loop and oriented in the direction in which a right-handed screw would advance if turned in the direction of the current. Its dipole moment is measured in ampere-meter² ($= 10^{10}$ pole-cm). The orbital motions of electrons around an atomic nucleus constitute circular currents and cause atoms to have magnetic mo-

ments. Molecules also have spin, which gives them magnetic moments.

A magnetizable body placed in an external magnetic field becomes magnetized by induction; the magnetization is due to the reorientation of atoms and molecules so that their spins line up. The magnetization is measured by the *magnetic polarization* M (also called *magnetization intensity* or *dipole moment per unit volume*). The lineup of internal dipoles produces a field M , which, within the body, is added to the magnetizing field H . If M is constant and has the same direction throughout, a body is said to be *uniformly magnetized*. The SI unit for magnetization is ampere-meter² per meter³ [= ampere per meter (A/m)].

For low magnetic fields, M is proportional to H and is in the direction of H . The degree to which a body is magnetized is determined by its *magnetic susceptibility* k , which is defined by

$$M = kH \quad (3.5)$$

Magnetic susceptibility in emu differs from that in SI units by the factor 4π , that is,

$$k_{\text{SI}} = 4\pi k'_{\text{emu}} \quad (3.6)$$

Susceptibility is the fundamental rock parameter in magnetic prospecting. The magnetic response of rocks and minerals is determined by the amounts and susceptibilities of magnetic materials in them. The susceptibilities of various materials are listed in Table 3.1, Section 3.3.7.

The *magnetic induction* B is the total field, including the effect of magnetization. It can be written

$$B = \mu_0(H + M) = \mu_0(1 + k)H = \mu\mu_0 H \quad (3.7a)$$

$$B' = H' + 4\pi M' = (1 + 4\pi k')H' = \mu H' \quad (3.7b)$$

when H and M (H' and M') are in the same direction, as is usually the case. The SI unit for B is the tesla = 1 newton/ampere-meter = 1 weber/meter² (Wb/m^2). The electromagnetic unit for B' is the gauss [= 10^{-4} tesla (T)]. The permeability of free space μ_0 has the value $4\pi \times 10^{-7}$ $\text{Wb}/\text{A}\cdot\text{m}$. In vacuum $\mu = 1$ and in air $\mu \approx 1$. Confusion sometimes results between H' and B' because the em units gauss and oersted are numerically equal and dimensionally the same, although conceptually different; both H' and B' are sometimes called the "magnetic field strength." In magnetic prospecting, we measure B to about 10^{-4} of the Earth's main field (which is about $50 \mu\text{T}$). The unit of magnetic induction generally used for geophysical work is the nanotesla (also

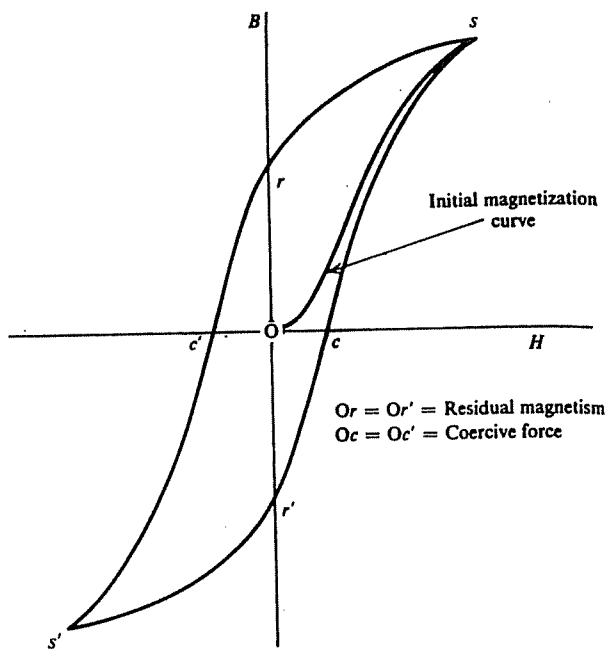


Figure 3.2. Hysteresis loop. s, s' = saturation, r and r' = remanent magnetism, c and c' = coercive force.

called the gamma, γ):

$$1\gamma = 10^{-9} \text{ T} = 1 \text{ nT}$$

There is often confusion as to whether the quantity involved in magnetic exploration is B or H . Although we measure B_e , we are interested in the Earth's field H_e . However, because B and H are linearly related [Eq. (3.7)] and usually $\mu \approx 1$, we can (and do) treat a map of B_e as if it were a map of H_e .

We also speak of *magnetic flux* or *magnetic lines of force* ϕ :

$$\phi = \mathbf{B} \cdot \mathbf{A} \quad (3.8)$$

where A is a vector area (§A.3.2). Thus $|B| = \phi/|A|$ when A and B are parallel, that is, B is the density of magnetic flux. The SI unit for magnetic flux is the weber (= $\text{T}\cdot\text{m}^2$) and the em unit is the maxwell (= 10^{-8} Wb).

3.2.2. B-H Relations: The Hysteresis Loop

The relation between B and H can be complex in ferromagnetic materials (§3.3.5). This is illustrated by hysteresis (Fig. 3.2) in a cycle of magnetization. If a demagnetized sample is subjected to an increasing magnetizing field H , we obtain the first portion of the curve in which B increases with H until it flattens off as we approach the maximum value that B can have for the sample (*saturation*). When H is decreased, the curve does not retrace the same path, but it does show a positive value of B when $H = 0$;

this is called *residual (remanent) magnetism*. When H is reversed, B finally becomes zero at some negative value of H known as the *coercive force*. The other half of the hysteresis loop is obtained by making H still more negative until reverse saturation is reached and then returning H to the original positive saturation value. The area inside the curve represents the energy loss per cycle per unit volume as a result of hysteresis (see Kip, 1962, pp. 235–7). Residual effects in magnetic materials will be discussed in more detail in Section 3.3.6. In some magnetic materials, B may be quite large as a result of previous magnetization having no relation to the present value of H .

3.2.3. Magnetostatic Potential for a Dipole Field

Conceptually the magnetic scalar potential A at the point P is the work done on a unit positive pole in bringing it from infinity by any path against a magnetic field $\mathbf{F}(r)$ [compare Eq. (2.4)]. (Henceforth in this chapter \mathbf{F} , F indicate magnetic field rather than force and we assume $\mu = 1$.) When $\mathbf{F}(r)$ is due to a positive pole at a distance r from P ,

$$A(r) = - \int_{-\infty}^r \mathbf{F}(r) \cdot d\mathbf{r} = p/r \quad (3.9)$$

However, since a magnetic pole cannot exist, we consider a magnetic dipole to get a realistic entity. Referring to Figure 3.3, we calculate A at an external point:

$$\begin{aligned} A &= \left(\frac{p}{r_1} - \frac{p}{r_2} \right) \\ &= p \left\{ \frac{1}{(r^2 + l^2 - 2lr \cos \theta)^{1/2}} \right. \\ &\quad \left. - \frac{1}{(r^2 + l^2 + 2lr \cos \theta)^{1/2}} \right\} \quad (3.10) \end{aligned}$$

We can derive the vector \mathbf{F} by taking the gradient of A [Eq. (A.17)],

$$\mathbf{F}(r) = -\nabla A(r) \quad (3.11)$$

Its radial component is $F_r = -\partial A / \partial r$ and its angular

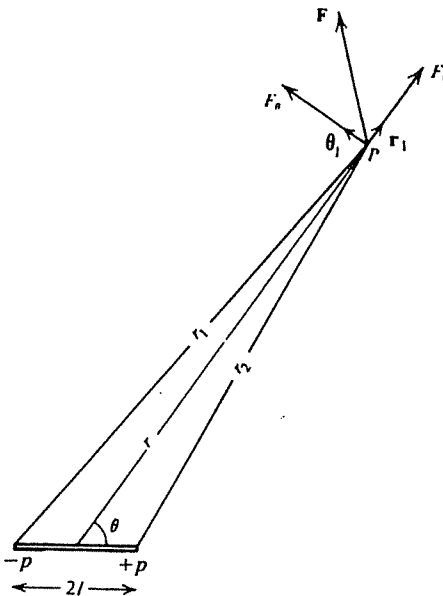


Figure 3.3. Calculating the field of a magnetic dipole.

radial component is $F_\theta = -\partial A / \partial \theta$; these are

$$\begin{aligned} F_r &= -p \left\{ \frac{r + l \cos \theta}{(r^2 + l^2 + 2rl \cos \theta)^{3/2}} \right. \\ &\quad \left. - \frac{r - l \cos \theta}{(r^2 + l^2 - 2rl \cos \theta)^{3/2}} \right\} \quad (3.12a) \end{aligned}$$

$$\begin{aligned} F_\theta &= p \left\{ \frac{l \sin \theta}{(r^2 + l^2 + 2rl \cos \theta)^{3/2}} \right. \\ &\quad \left. + \frac{l \sin \theta}{(r^2 + l^2 - 2rl \cos \theta)^{3/2}} \right\} \quad (3.12b) \end{aligned}$$

When $r \gg l$, Equation (3.10) becomes

$$A \approx |m| \cos \theta / r^2 \quad (3.13)$$

where m is the dipole moment of magnitude $m = 2lp$. Equations (3.11) and (3.13) give [§A.4 and Equation (A.33)]

$$\mathbf{F} \approx (m/r^3)(2 \cos \theta \mathbf{r}_1 + \sin \theta \mathbf{\theta}_1) \quad (3.14a)$$

where unit vectors \mathbf{r}_1 and $\mathbf{\theta}_1$ are in the direction of increasing r and θ (counterclockwise in Fig. 3.3). The resultant magnitude is

$$F = |\mathbf{F}| \approx (m/r^3)(1 + 3 \cos^2 \theta)^{1/2} \quad (3.14b)$$

and the direction with respect to the dipole axis is

$$\tan \alpha = F_\theta / F_r = (1/2) \tan \theta \quad (3.14c)$$

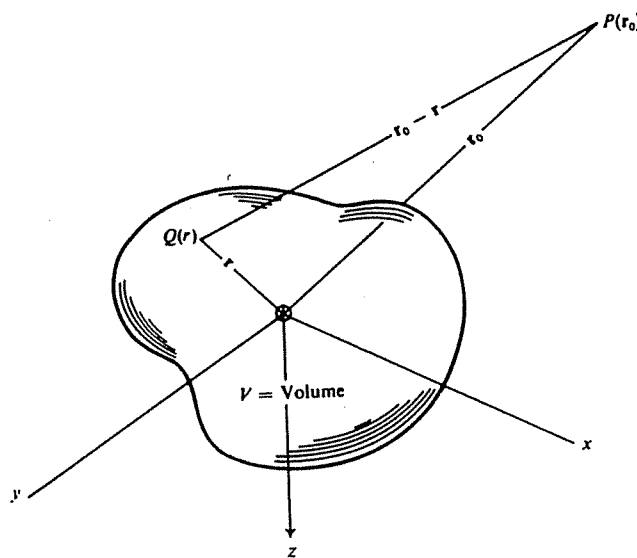


Figure 3.4. General magnetic anomaly.

Two special cases, $\theta = 0$ and $\pi/2$ in Equation (3.12), are called the *Gauss-A* (end-on) and *Gauss-B* (side-on) positions. From Equations (3.12) they are given by

$$F_r = 2mr/(r^2 - l^2)^2 \quad F_\theta = 0 \quad \theta = 0 \quad (3.15a)$$

$$F_r = 0 \quad F_\theta = m/(r^2 + l^2)^{3/2} \quad \theta = \pi/2 \quad (3.15b)$$

If $r \gg l$, these simplify to

$$\left. \begin{aligned} F_r &\approx 2m/r^3 & \theta &= 0 \\ F_\theta &\approx m/r^3 & \theta &= \pi/2 \end{aligned} \right\} \quad (3.15c)$$

3.2.4. The General Magnetic Anomaly

A volume of magnetic material can be considered as an assortment of magnetic dipoles that results from the magnetic moments of individual atoms and dipoles. Whether they initially are aligned so that a body exhibits residual magnetism depends on its previous magnetic history. They will, however, be aligned by induction in the presence of a magnetizing field. In any case, we may regard the body as a continuous distribution of dipoles resulting in a vector dipole moment per unit volume, \mathbf{M} , of magnitude M . The scalar potential at P [see Fig. 3.3 and Eq. (3.13)] some distance away from a dipole M ($r \gg l$) is

$$A = M(r)\cos\theta/r^2 = -\mathbf{M}(r) \cdot \nabla(1/r) \quad (3.16)$$

The potential for the whole body at a point outside

the body (Fig. 3.4) is

$$A = - \int_V \mathbf{M}(\mathbf{r}) \cdot \nabla \left(\frac{1}{|\mathbf{r}_0 - \mathbf{r}|} \right) dv \quad (3.17)$$

The resultant magnetic field can be obtained by employing Equation (3.11) with Equation (3.17). This gives

$$\mathbf{F}(\mathbf{r}_0) = \nabla \int_V \mathbf{M}(\mathbf{r}) \cdot \nabla \left(\frac{1}{|\mathbf{r}_0 - \mathbf{r}|} \right) dv \quad (3.18)$$

If \mathbf{M} is a constant vector with direction $\alpha = \ell\mathbf{i} + m\mathbf{j} + n\mathbf{k}$, then the operation

$$\mathbf{M} \cdot \nabla = M \frac{\partial}{\partial \alpha} = M \left(\ell \frac{\partial}{\partial x} + m \frac{\partial}{\partial y} + n \frac{\partial}{\partial z} \right) \quad (3.19)$$

[Eq. (A.18)] and

$$A = -M \frac{\partial}{\partial \alpha} \int_V \left(\frac{dv}{|\mathbf{r}_0 - \mathbf{r}|} \right) \quad (3.20)$$

The magnetic field in Equation (3.20) exists in the presence of the Earth's field \mathbf{F}_e , that is, the total field \mathbf{F} is given by

$$\mathbf{F} = \mathbf{F}_e + \mathbf{F}(\mathbf{r}_0)$$

where the directions of \mathbf{F}_e and $\mathbf{F}(\mathbf{r}_0)$ are not necessarily the same. If $\mathbf{F}(\mathbf{r}_0)$ is much smaller than \mathbf{F}_e or if the body has no residual magnetism, \mathbf{F} and \mathbf{F}_e will be in approximately the same direction. Where $\mathbf{F}(\mathbf{r}_0)$ is an appreciable fraction (say, 25% or more) of \mathbf{F}_e and

has a different direction, the component of $\mathbf{F}(r_0)$ in the direction of \mathbf{F}_e , F_D , becomes [Eq. (3.20)]

$$F_D = -\mathbf{f}_1 \cdot \nabla A = -\frac{\partial A}{\partial f} = M \frac{\partial^2}{\partial \alpha \partial f} \int_V \frac{dv}{|\mathbf{r}_0 - \mathbf{r}|} \quad (3.21a)$$

where \mathbf{f}_1 is a unit vector in the direction of \mathbf{F}_e (§3.3.2a). If the magnetization is mainly induced by \mathbf{F}_e , then

$$F_D(r_0) = M \frac{\partial^2}{\partial f^2} \int_V \frac{dv}{|\mathbf{r}_0 - \mathbf{r}|} = k F_e \frac{\partial^2}{\partial f^2} \int_V \frac{dv}{|\mathbf{r}_0 - \mathbf{r}|} \quad (3.21b)$$

The magnetic interpretation problem is clearly more complex than the gravity problem because of the dipolar field (compare §2.2.3).

The magnetic potential A , like the gravitational potential U , satisfies Laplace's and Poisson's equations. Following the method used to derive Equations (2.12) and (2.13), we get

$$\nabla \cdot \mathbf{F} = -\nabla^2 A = 4\pi\mu p$$

p is the net positive pole strength per unit volume at a point. We recall that a field \mathbf{F} produces a partial reorientation along the field direction of the previously randomly oriented elementary dipoles. This causes, in effect, a separation of positive and negative poles. For example, the x component of \mathbf{F} separates pole strengths $+q$ and $-q$ by a distance ζ along the x axis and causes a net positive pole strength $(q\zeta) dy dz = M_x dy dz$ to enter the rear face in Figure A.2a. Because the pole strength leaving through the opposite face is $\{M_x + (\partial M_x / \partial x) dx\} dy dz$, the net positive pole strength per unit volume (p) created at a point by the field \mathbf{F} is $-\nabla \cdot \mathbf{M}$. Thus,

$$\nabla^2 A = 4\pi\mu \nabla \cdot \mathbf{M}(r) \quad (3.22)$$

In a nonmagnetic medium, $\mathbf{M} = 0$ and

$$\nabla^2 A = 0 \quad (3.23)$$

3.2.5. Poisson's Relation

If we have an infinitesimal unit volume with magnetic moment $\mathbf{M} = M\mathbf{a}_1$ and density ρ , then at a distant point we have, from Equation (3.16),

$$A = -\mathbf{M} \cdot \nabla(1/r) = -M \nabla(1/r) \cdot \mathbf{a}_1 \quad (3.24)$$

From Equations (2.3a), (2.5), and (A.18), the compo-

nent of \mathbf{g} in the direction \mathbf{a}_1 is

$$g_\alpha = -dU/d\alpha = -\nabla U \cdot \mathbf{a}_1 = -\gamma\rho \nabla(1/r) \cdot \mathbf{a}_1 \quad (3.25)$$

Thus,

$$A = (M/\gamma\rho) g_\alpha \quad (3.26)$$

If we apply this result to an extended body, we must sum contributions for each element of volume. Provided that M and ρ do not change throughout the body, the potentials A and U will be those for the extended body. Therefore, Equations (3.24) to (3.26) are valid for an extended body with constant density and uniform magnetization.

In terms of fields,

$$\begin{aligned} \mathbf{F} &= -\nabla A = -(M/\gamma\rho) \nabla g_\alpha \\ &= (M/\gamma\rho) \nabla(\nabla U \cdot \mathbf{a}_1) \\ &= (M/\gamma\rho) \nabla U_\alpha \end{aligned} \quad (3.27a)$$

where $U_\alpha = dU/d\alpha$. For a component of \mathbf{F} in the direction β_1 , this becomes

$$F_\beta = (M/\gamma\rho) U_{\alpha\beta} \quad (3.27b)$$

In particular, if M is vertical, the vertical component of \mathbf{F} is

$$Z = (M/\gamma\rho) U_{zz} = (M/\gamma\rho)(\partial g_z / \partial z) \quad (3.28)$$

These relations are used to make pseudogravity maps from magnetic data.

3.3. MAGNETISM OF THE EARTH

3.3.1. Nature of the Geomagnetic Field

As far as exploration geophysics is concerned, the geomagnetic field of the Earth is composed of three parts:

1. The main field, which varies relatively slowly and is of internal origin.
2. A small field (compared to the main field), which varies rather rapidly and originates outside the Earth.
3. Spatial variations of the main field, which are usually smaller than the main field, are nearly constant in time and place, and are caused by local magnetic anomalies in the near-surface crust of the Earth. These are the targets in magnetic prospecting.

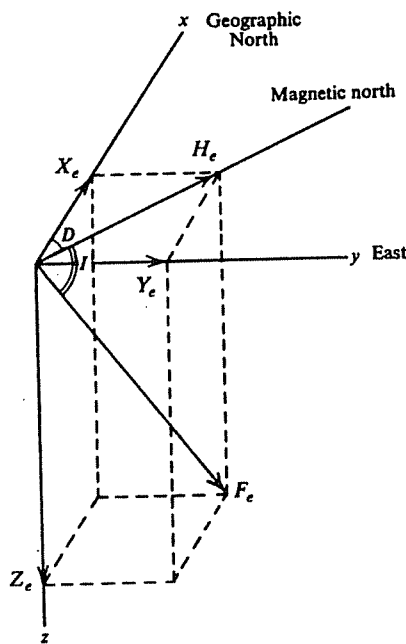


Figure 3.5. Elements of the Earth's magnetic field.

3.3.2. The Main Field

(a) *The Earth's magnetic field.* If an unmagnetized steel needle could be hung at its center of gravity, so that it is free to orient itself in any direction, and if other magnetic fields are absent, it would assume the direction of the Earth's total magnetic field, a direction that is usually neither horizontal nor in-line with the geographic meridian. The magnitude of this field, F_e , the *inclination* (or *dip*) of the needle from the horizontal, I , and the angle it makes with geographic north (the *declination*), D , completely define the main magnetic field.

The *magnetic elements* (Whitham, 1960) are illustrated in Figure 3.5. The field can also be described in terms of the vertical component, Z_e , reckoned positive downward, and the horizontal component, H_e , which is always positive. X_e and Y_e are the components of H_e , which are considered positive to the north and east, respectively. These elements are related as follows:

$$\left. \begin{aligned} F_e^2 &= H_e^2 + Z_e^2 = X_e^2 + Y_e^2 + Z_e^2 \\ H_e &= F_e \cos I \quad Z_e = F_e \sin I \\ X_e &= H_e \cos D \quad Y_e = H_e \sin D \\ \tan D &= Y_e/X_e \quad \tan I = Z_e/H_e \\ F_e &= F_e \mathbf{f}_1 = F_e (\cos D \cos I \mathbf{i} \\ &\quad + \sin D \cos I \mathbf{j} + \sin I \mathbf{k}) \end{aligned} \right\} \quad (3.29)$$

As stated earlier, the end of the needle that dips downward in northern latitudes is the north-seeking

or positive pole; the end that dips downward in southern latitudes is the south-seeking or negative pole.

Maps showing lines of equal declination, inclination, horizontal intensity, and so on, are called *isomagnetic maps* (Fig. 3.6). *Isogonic*, *isoclinic*, and *isodynamic maps* show, respectively, lines of equal declination D , inclination I , and equal values of F_e , H_e , or Z_e . Note that the inclination is large (that is, $Z_e > H_e$) for most of the Earth's land masses, and hence corrections do not have to be made for latitude variations of F_e or Z_e (≈ 4 nT/km) except for surveys covering extensive areas. The overall magnetic field does not reflect variations in surface geology, such as mountain ranges, mid-ocean ridges or earthquake belts, so the source of the main field lies deep within the Earth. The geomagnetic field resembles that of a dipole whose north and south magnetic poles are located approximately at $75^\circ\text{N}, 101^\circ\text{W}$ and $69^\circ\text{S}, 145^\circ\text{E}$. The dipole is displaced about 300 km from the Earth's center toward Indonesia and is inclined some 11.5° to the Earth's axis. However, the geomagnetic field is more complicated than the field of a simple dipole. The points where a dip needle is vertical, the *dip poles*, are at $75^\circ\text{N}, 101^\circ\text{W}$ and $67^\circ\text{S}, 143^\circ\text{E}$.

The magnitudes of F_e at the north and south magnetic poles are 60 and 70 μT , respectively. The minimum value, $\sim 25 \mu\text{T}$, occurs in southern Brazil—South Atlantic. In a few locations, F_e is larger than 300 μT because of near-surface magnetic features. The line of zero inclination (*magnetic equator*, where $Z = 0$) is never more than 15° from the Earth's equator. The largest deviations are in South America and the eastern Pacific. In Africa and Asia it is slightly north of the equator.

(b) *Origin of the main field.* Spherical harmonic analysis of the observed magnetic field shows that over 99% is due to sources inside the Earth. The present theory is that the main field is caused by convection currents of conducting material circulating in the liquid outer core (which extends from depths of 2,800 to 5,000 km). The Earth's core is assumed to be a mixture of iron and nickel, both good electrical conductors. The magnetic source is thought to be a self-excited dynamo in which highly conductive fluid moves in a complex manner caused by convection. Paleomagnetic data show that the magnetic field has always been roughly along the Earth's spin axis, implying that the convective motion is coupled to the Earth's spin. Recent exploration of the magnetic fields of other planets and their satellites provide fascinating comparisons with the Earth's field.

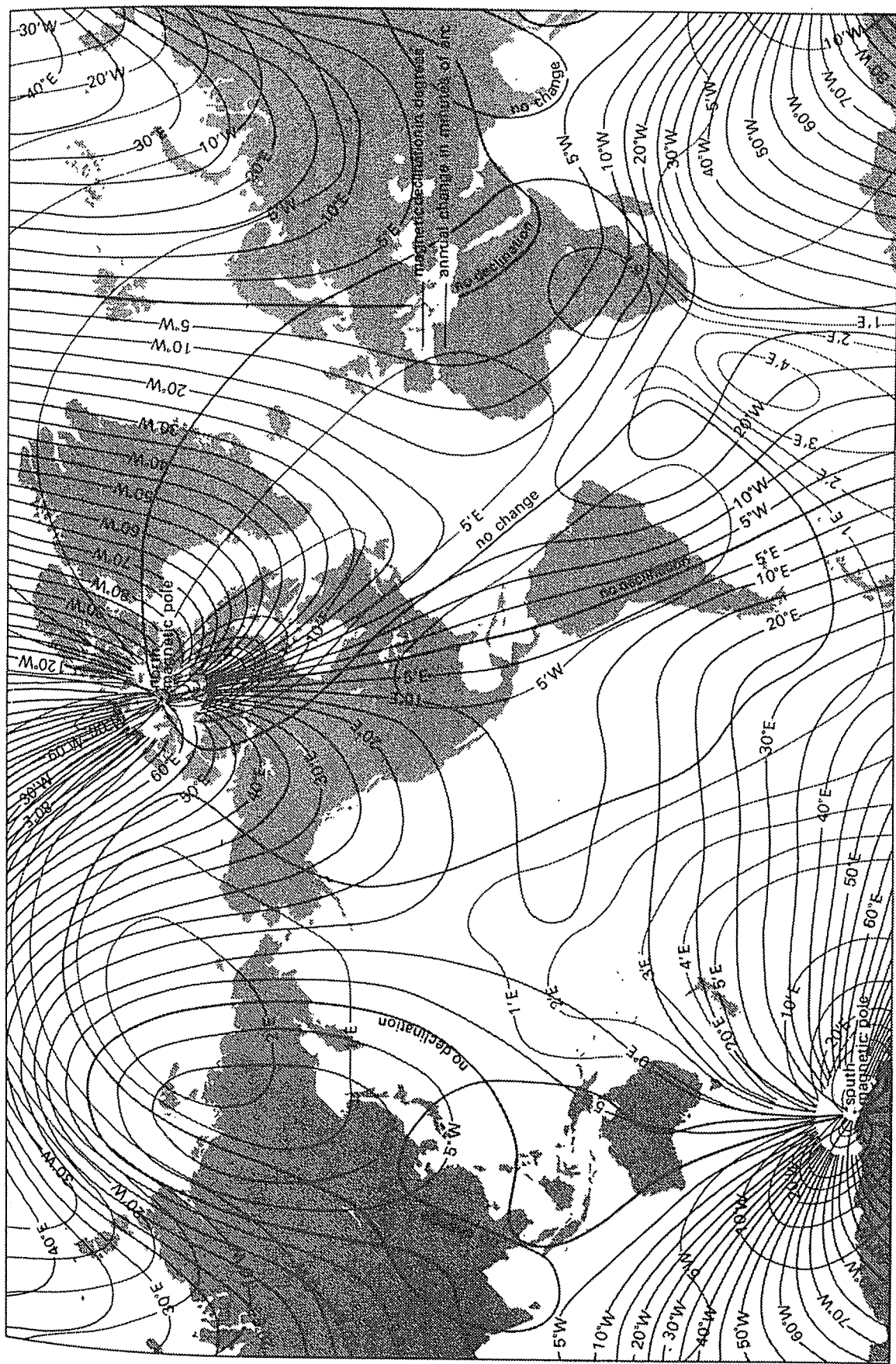


Figure 3.6. The Earth's magnetic field in 1975 (From Smith, 1982). (a) Declination (heavy lines) and annual rate of change in minutes/year (light lines)

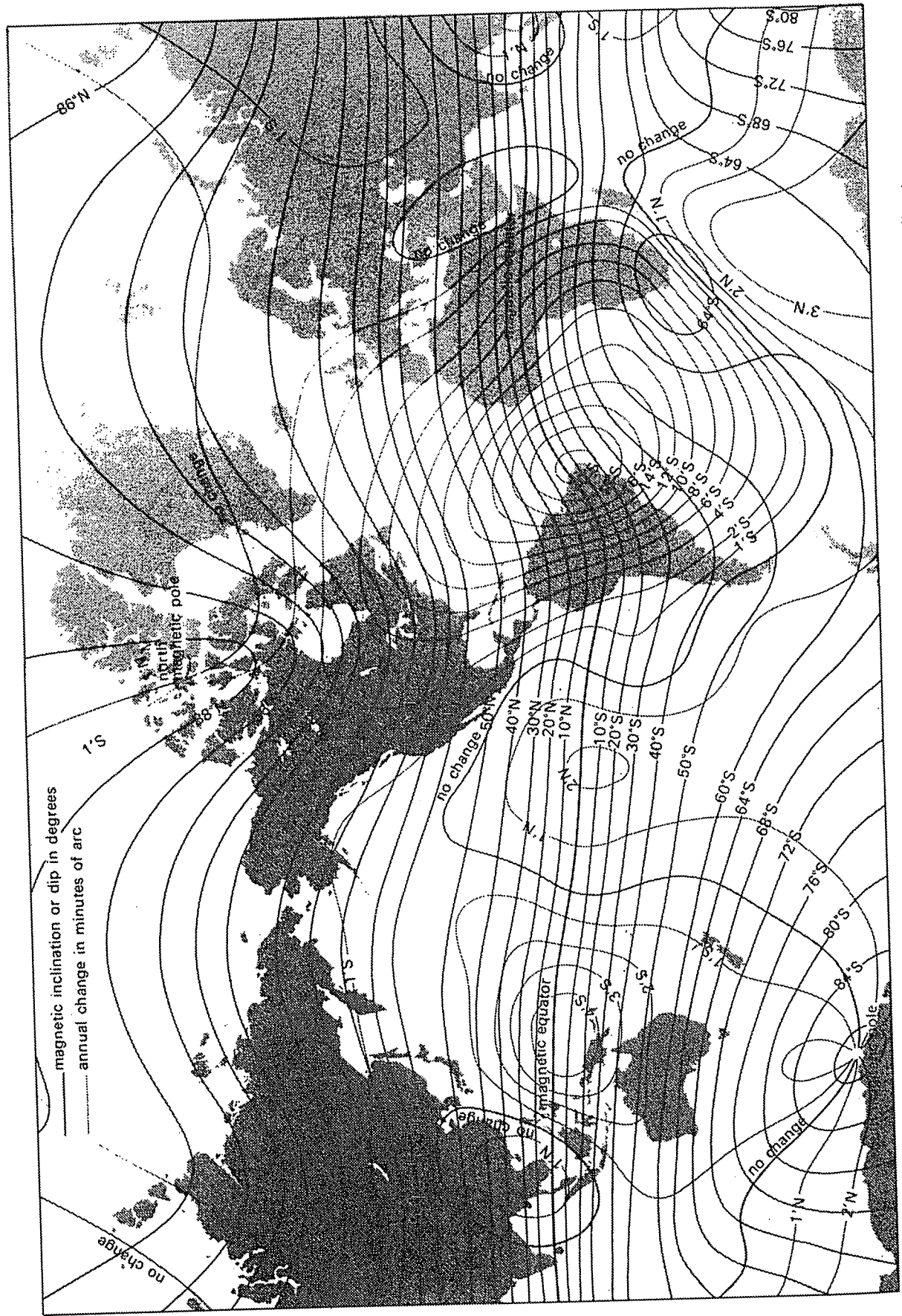


Figure 3.6. (Continued) (b) geomagnetic latitude (heavy lines) and annual rate of change in minutes/year (light lines)

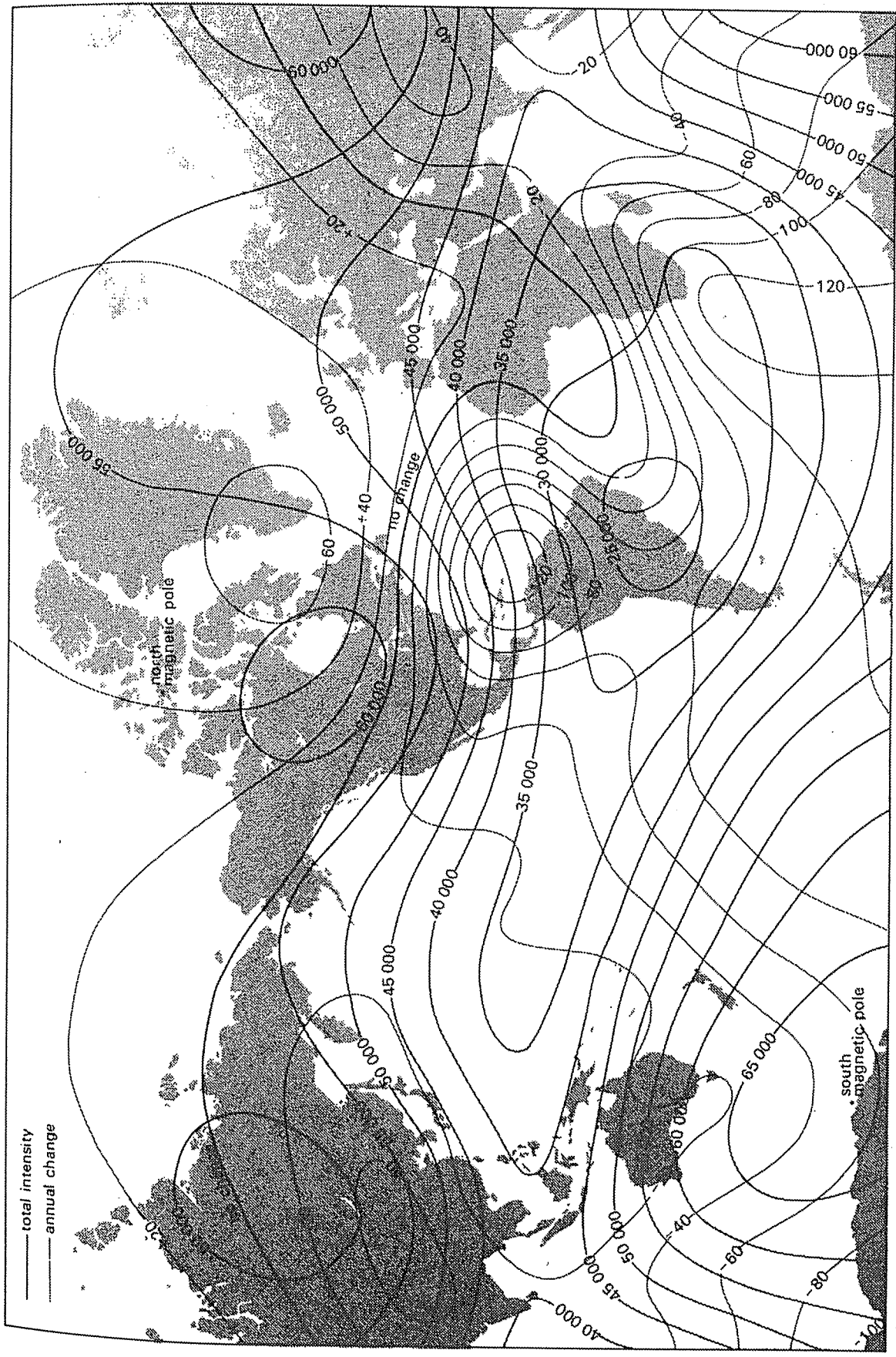


Figure 3.6. (Continued) (c) total field strength in nanotesla (heavy lines) and rate of change in nanotesla/year (light lines).

(c) *Secular variations of the main field.* Four hundred years of continuous study of the Earth's field has established that it changes slowly. The inclination has changed some 10° (75° to 65°) and the declination about 35° (10°E to 25°W and back to 10°W) during this period. The source of this wandering is thought to be changes in convection currents in the core.

The Earth's magnetic field has also reversed direction a number of times. The times of many of the periodic field reversals have been ascertained and provide a *magnetochronographic time scale*.

3.3.3. The External Magnetic Field

Most of the remaining small portion of the geomagnetic field appears to be associated with electric currents in the ionized layers of the upper atmosphere. Time variations of this portion are much more rapid than for the main "permanent" field. Some effects are:

1. A cycle of 11 years duration that correlates with sunspot activity.
2. Solar diurnal variations with a period of 24 h and a range of 30 nT that vary with latitude and season, and are probably controlled by action of the solar wind on ionospheric currents.
3. Lunar variations with a 25 h period and an amplitude 2 nT that vary cyclically throughout the month and seem to be associated with a Moon-ionosphere interaction.
4. Magnetic storms that are transient disturbances with amplitudes up to 1,000 nT at most latitudes and even larger in polar regions, where they are associated with aurora. Although erratic, they often occur at 27 day intervals and correlate with sunspot activity. At the height of a magnetic storm (which may last for several days), long-range radio reception is affected and magnetic prospecting may be impractical.

These time and space variations of the Earth's main field do not significantly affect magnetic prospecting except for the occasional magnetic storm. Diurnal variations can be corrected for by use of a base-station magnetometer. Latitude variations (≈ 4 nT/km) require corrections only for high-resolution, high-latitude, or large-scale surveys.

3.3.4. Local Magnetic Anomalies

Local changes in the main field result from variations in the magnetic mineral content of near-surface rocks. These anomalies occasionally are large enough to double the main field. They usually do not persist over great distances; thus magnetic maps generally do not exhibit large-scale regional features (although

the Canadian Shield, for example, shows a magnetic contrast to the Western Plains). Many large, erratic variations often make magnetic maps extremely complex. The sources of local magnetic anomalies cannot be very deep, because temperatures below ~ 40 km should be above the *Curie point*, the temperature ($\approx 550^\circ\text{C}$) at which rocks lose their magnetic properties. Thus, local anomalies must be associated with features in the upper crust.

3.3.5. Magnetism of Rocks and Minerals

Magnetic anomalies are caused by magnetic minerals (mainly magnetite and pyrrhotite) contained in the rocks. Magnetically important minerals are surprisingly few in number.

Substances can be divided on the basis of their behavior when placed in an external field. A substance is *diamagnetic* if its field is dominated by atoms with orbital electrons oriented to oppose the external field, that is, if it exhibits negative susceptibility. Diamagnetism will prevail only if the net magnetic moment of all atoms is zero when H is zero, a situation characteristic of atoms with completely filled electron shells. The most common diamagnetic earth materials are graphite, marble, quartz, and salt. When the magnetic moment is not zero when H is zero, the susceptibility is positive and the substance is *paramagnetic*. The effects of diamagnetism and most paramagnetism are weak.

Certain paramagnetic elements, namely iron, cobalt, and nickel, have such strong magnetic interaction that the moments align within fairly large regions called *domains*. This effect is called *ferromagnetism* and it is $\sim 10^6$ times the effects of diamagnetism and paramagnetism. Ferromagnetism decreases with increasing temperature and disappears entirely at the Curie temperature. Apparently ferromagnetic minerals do not exist in nature.

The domains in some materials are subdivided into subdomains that align in opposite directions so that their moments nearly cancel; although they would otherwise be considered ferromagnetic, the susceptibility is comparatively low. Such a substance is *antiferromagnetic*. The only common example is hematite.

In some materials, the magnetic subdomains align in opposition but their net moment is not zero, either because one set of subdomains has a stronger magnetic alignment than the other or because there are more subdomains of one type than of the other. These substances are *ferrimagnetic*. Examples of the first type are magnetite and titanomagnetite, oxides of iron and of iron and titanium. Pyrrhotite is a magnetic mineral of the second type. Practically all magnetic minerals are ferrimagnetic.

3.3.6. Remanent Magnetism

In many cases, the magnetization of rocks depends mainly on the present geomagnetic field and the magnetic mineral content. Residual magnetism (called *natural remanent magnetization*, NRM) often contributes to the total magnetization, both in amplitude and direction. The effect is complicated because NRM depends on the magnetic history of the rock. Natural remanent magnetization may be due to several causes. The principal ones are:

1. *Thermoremanent magnetization* (TRM), which results when magnetic material is cooled below the Curie point in the presence of an external field (usually the Earth's field). Its direction depends on the direction of the field at the time and place where the rock cooled. Remanence acquired in this fashion is particularly stable. This is the main mechanism for the residual magnetization of igneous rocks.
2. *Detrital magnetization* (DRM), which occurs during the slow settling of fine-grained particles in the presence of an external field. Varied clays exhibit this type of remanence.
3. *Chemical remanent magnetization* (CRM), which takes place when magnetic grains increase in size or are changed from one form to another as a result of chemical action at moderate temperatures, that is, below the Curie point. This process may be significant in sedimentary and metamorphic rocks.
4. *Isothermal remanent magnetization* (IRM), which is the residual left following the removal of an external field (see Fig. 3.2). Lightning strikes produce IRM over very small areas.
5. *Viscous remanent magnetization* (VRM), which is produced by long exposure to an external field; the buildup of remanence is a logarithmic function of time. VRM is probably more characteristic of fine-grained than coarse-grained rocks. This remanence is quite stable.

Studies of the magnetic history of the Earth (*paleomagnetism*) indicate that the Earth's field has varied in magnitude and has reversed its polarity a number of times (Strangway, 1970). Furthermore, it appears that the reversals took place rapidly in geologic time, because there is no evidence that the Earth existed without a magnetic field for any significant period. Model studies of a self-excited dynamo show such a rapid turnover. Many rocks have remanent magnetism that is oriented neither in the direction of, nor opposite to, the present Earth field. Such results support the plate tectonics theory. Paleomagnetism helps age-date rocks and determine past movements, such as plate rotations. Paleomagnetic

laboratory methods separate residual from induced magnetization, something that cannot be done in the field.

3.3.7. Magnetic Susceptibilities of Rocks and Minerals

Magnetic susceptibility is the significant variable in magnetics. It plays the same role as density does in gravity interpretation. Although instruments are available for measuring susceptibility in the field, they can only be used on outcrops or on rock samples, and such measurements do not necessarily give the bulk susceptibility of the formation.

From Figure 3.2, it is obvious that k (hence μ also) is not constant for a magnetic substance; as H increases, k increases rapidly at first, reaches a maximum, and then decreases to zero. Furthermore, although magnetization curves have the same general shape, the value of H for saturation varies greatly with the type of magnetic mineral. Thus it is important in making susceptibility determinations to use a value of H about the same as that of the Earth's field.

Since the ferrimagnetic minerals, particularly magnetite, are the main source of local magnetic anomalies, there have been numerous attempts to establish a quantitative relation between rock susceptibility and Fe_3O_4 concentration. A rough linear dependence (k ranging from 10^{-3} to 1 SI unit as the volume percent of Fe_3O_4 increases from 0.05% to 35%) is shown in one report, but the scatter is large, and results from other areas differ.

Table 3.1 lists magnetic susceptibilities for a variety of rocks. Although there is great variation, even for a particular rock, and wide overlap between different types, sedimentary rocks have the lowest average susceptibility and basic igneous rocks have the highest. In every case, the susceptibility depends only on the amount of ferrimagnetic minerals present, mainly magnetite, sometimes titanomagnetite or pyrrhotite. The values of chalcopyrite and pyrite are typical of many sulfide minerals that are basically nonmagnetic. It is possible to locate minerals of negative susceptibility, although the negative values are very small, by means of detailed magnetic surveys. It is also worth noting that many iron minerals are only slightly magnetic.

3.3.8. Magnetic Susceptibility Measurements

(a) *Measurement of k .* Most measurements of k involve a comparison of the sample with a standard. The simplest laboratory method is to compare the deflection produced on a tangent magnetometer by a

Table 3.1. Magnetic susceptibilities of various rocks and minerals.

Type	Susceptibility $\times 10^3$ (SI)	
	Range	Average
<i>Sedimentary</i>		
Dolomite	0–0.9	0.1
Limestones	0–3	0.3
Sandstones	0–20	0.4
Shales	0.01–15	0.6
Av. 48 sedimentary	0–18	0.9
<i>Metamorphic</i>		
Amphibolite		0.7
Schist	0.3–3	1.4
Phyllite		1.5
Gneiss	0.1–25	4
Quartzite		
Serpentine	3–17	6
Slate	0–35	4.2
Av. 61 metamorphic	0–70	
<i>Igneous</i>		
Granite	0–50	2.5
Rhyolite	0.2–35	
Dolerite	1–35	17
Augite-syenite	30–40	
Olivine-diabase		25
Diabase	1–160	55
Porphyry	0.3–200	60
Gabbro	1–90	70
Basalts	0.2–175	70
Diorite	0.6–120	85
Pyroxenite		125
Peridotite	90–200	150
Andesite		160
Av. acidic igneous	0–80	8
Av. basic igneous	0.5–97	25
<i>Minerals</i>		
Graphite		0.1
Quartz		-0.01
Rock salt		-0.01
Anhydrite, gypsum	-0.001 – 0.01	-0.01
Calcite		0.02
Coal		0.2
Clays		0.4
Chalcopyrite		0.7
Sphalerite		0.9
Cassiterite		
Siderite	1–4	
Pyrite	0.05–5	1.5
Limonite		2.5
Arsenopyrite		3
Hematite	0.5–35	6.5
Chromite	3–110	7
Franklinite		430
Pyrrhotite	1–6000	1500
Ilmenite	300–3500	1800
Magnetite	1200–19200	6000

prepared sample (either a drill core or powdered rock in a tube) with that of a standard sample of magnetic material (often FeCl_3 powder in a test tube) when the sample is in the Gauss-A position [Eq. (3.15a)]. The susceptibility of the sample is found from the ratio of deflections:

$$k_s = k_{std} d_s / d_{std}$$

d_s and d_{std} are the deflections for the sample and standard, respectively. The samples must be of the same size.

A similar comparison method employs an inductance bridge (Hague, 1957) having several air-core coils of different cross sections to accommodate samples of different sizes. The sample is inserted into one of the coils and the bridge balance condition is compared with the bridge balance obtained when a standard sample is in the coil. The bridge may be calibrated to give susceptibility directly, in which case the sample need not have a particular geometry (although the calibration may not be valid for samples of highly irregular shape). This type of instrument with a large diameter coil is used in field measurements on outcrop. The bridge is balanced first with the coil remote from the outcrop and then lying on it. A calibration curve obtained with a standard relates k and the change in inductance.

(b) *Measurement of remanent magnetism.* Measurement of remanent susceptibility is considerably more complicated than that of k . One method uses an astatic magnetometer, which consists of two magnets of equal moment that are rigidly mounted parallel to each other in the same horizontal plane with opposing poles. The magnetic system is suspended by a torsion fiber. The specimen is placed in various orientations below the astatic system and the angular deflections are measured. This device, in effect, measures the magnetic field gradient, so that extraneous fields must either be eliminated or made uniform over the region of the sample. Usually the entire assembly is mounted inside a three-component coil system that cancels the Earth's field.

Another instrument for the analysis of the residual component is the *spinner magnetometer*. The rock sample is rotated at high speed near a small pickup coil and its magnetic moment generates alternating current (ac) in the coil. The phase and intensity of the coil signal are compared with a reference signal generated by the rotating system. The total moment of the sample is obtained by rotating it about different axes.

Cryogenic instruments for determining two-axes remanent magnetism have been developed (Zimmerman and Campbell, 1975; Weinstock and

Overton, 1981). They achieve great sensitivity because of the high magnetic moments and low noise obtainable at superconducting temperatures.

3.4. FIELD INSTRUMENTS FOR MAGNETIC MEASUREMENTS

3.4.1. General

Typical sensitivity required in ground magnetic instruments is between 1 and 10 nT in a total field rarely larger than 50,000 nT. Recent airborne applications, however, have led to the development of magnetometers with sensitivity of 0.001 nT. Some magnetometers measure the absolute field, although this is not a particular advantage in magnetic surveying.

The earliest devices used for magnetic exploration were modifications of the mariner's compass, such as the Swedish mining compass, which measured dip I and declination D . Instruments (such as *magnetic variometers*, which are essentially dip needles of high sensitivity) were developed to measure Z_e and H_e , but they are seldom used now. Only the modern instruments, the fluxgate, proton-precession, and optical-pump (usually rubidium-vapor) magnetometers, will be discussed. The latter two measure the absolute total field, and the fluxgate instrument also generally measures the total field.

3.4.2. Fluxgate Magnetometer

This device was originally developed during World War II as a submarine detector. Several designs have been used for recording diurnal variations in the Earth's field, for airborne geomagnetics, and as portable ground magnetometers.

The fluxgate detector consists essentially of a core of magnetic material, such as mu-metal, permalloy, or ferrite, that has a very high permeability at low magnetic fields. In the most common design, two cores are each wound with primary and secondary coils, the two assemblies being as nearly as possible identical and mounted parallel so that the windings are in opposition. The two primary windings are connected in series and energized by a low frequency (50 to 1,000 Hz) current produced by a constant current source. The maximum current is sufficient to magnetize the cores to saturation, in opposite polarity, twice each cycle. The secondary coils, which consist of many turns of fine wire, are connected to a *differential amplifier*, whose output is proportional to the difference between two input signals.

The effect of saturation in the fluxgate elements is illustrated in Figure 3.7. In the absence of an external magnetic field, the saturation of the cores is

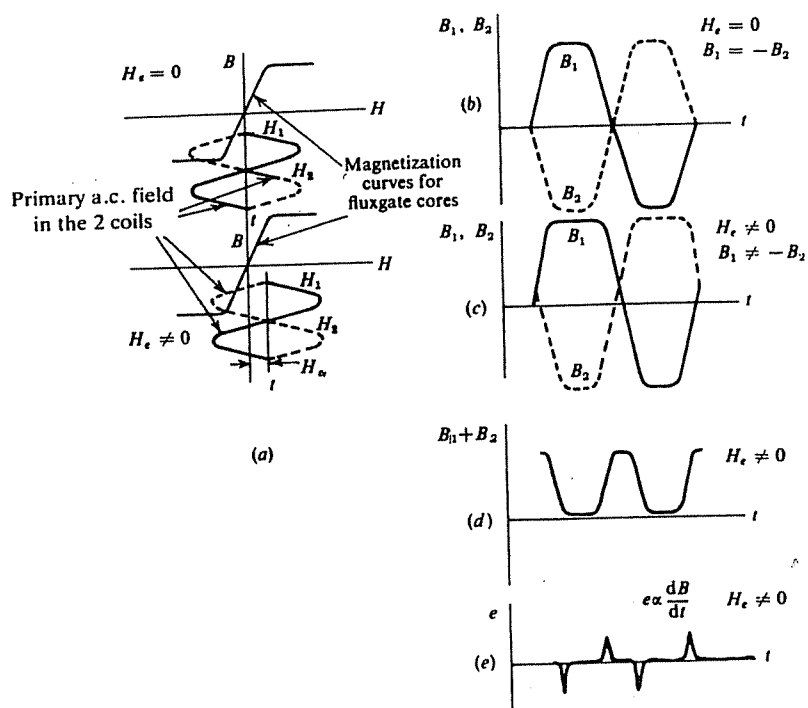


Figure 3.7. Principle of the fluxgate magnetometer. Note that $H_e = F_e$, etc. (From Whitham, 1960.) (a) Magnetization of the cores. (b) Flux in the two cores for $F_e = 0$. (c) Flux in the two cores for $F_e \neq 0$. (d) $F_1 + F_2$ for $F_e \neq 0$. (e) Output voltage for $F_e \neq 0$.

symmetrical and of opposite sign near the peak of each half-cycle so that the outputs from the two secondary windings cancel. The presence of an external field component parallel to the cores causes saturation to occur earlier for one half-cycle than the other, producing an unbalance. The difference between output voltages from the secondary windings is a series of voltage pulses which are fed into the amplifier, as shown in Figure 3.7d. The pulse height is proportional to the amplitude of the biasing field of the Earth. Obviously any component can be measured by suitable orientation of the cores.

The original problem with this type of magnetometer – a lack of sensitivity in the core – has been solved by the development and use of materials having sufficient initial permeability to saturate in small fields. Clearly the hysteresis loop should be as thin as possible. There remains a relatively high noise level, caused by hysteresis effects in the core. The fluxgate elements should be long and thin to reduce eddy currents. Improvements introduced to increase the signal-to-noise ratio include the following:

1. By deliberately unbalancing the two elements, voltage spikes are present with or without an ambient field. The presence of the Earth's field increases the voltage of one polarity more than the other and this difference is amplified.
2. Because the odd harmonics are canceled fairly



Figure 3.8. Portable fluxgate magnetometer.

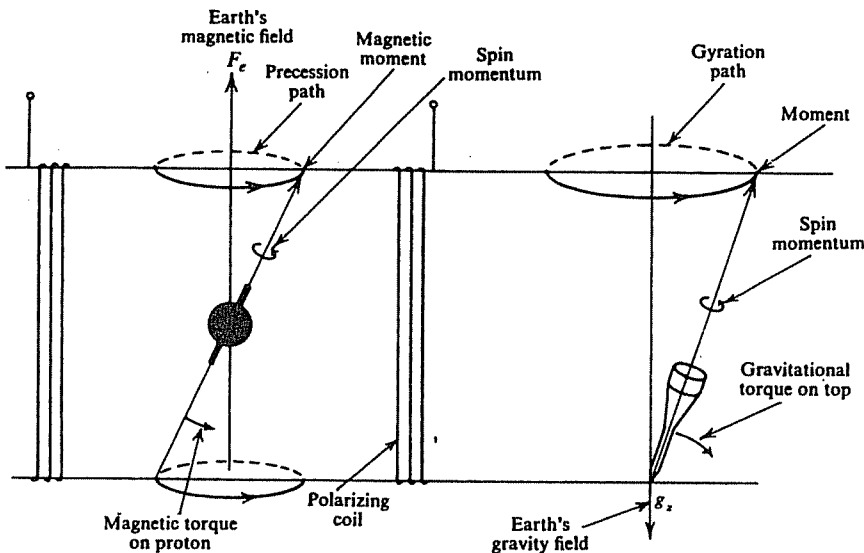


Figure 3.9. Proton precession and spinning-top analogy.

well in a reasonably matched set of cores, the even harmonics (generally only the second is significant) are amplified to appear as positive or negative signals, depending on the polarity of the Earth's field.

3. Most of the ambient field is canceled and variations in the remainder are detected with an extra secondary winding.
4. Negative feedback of the amplifier outputs is used to reduce the effect of the Earth's field.
5. By tuning the output of the secondary windings with a capacitance, the second harmonic is greatly increased; a phase-sensitive detector, rather than the difference amplifier, may be used with this arrangement.

There are several fundamental sources of error in the fluxgate instrument. These include inherent unbalance in the two cores, thermal and shock noise in cores, drift in biasing circuits, and temperature sensitivity (1 nT/°C or less). These disadvantages are minor, however, compared to the obvious advantages – direct readout, no azimuth orientation, rather coarse leveling requirements, light weight (2 to 3 kg), small size, and reasonable sensitivity. Another attractive feature is that any component of the magnetic field may be measured. No elaborate tripod is required and readings may be made very quickly, generally in about 15 s. A portable fluxgate instrument is shown in Figure 3.8.

3.4.3. Proton-Precession Magnetometer

This instrument grew out of the discovery, around 1945, of nuclear magnetic resonance. Some nuclei

have a net magnetic moment that, coupled with their spin, causes them to precess about an axial magnetic field.

The proton-precession magnetometer depends on the measurement of the free-precession frequency of protons (hydrogen nuclei) that have been polarized in a direction approximately normal to the direction of the Earth's field. When the polarizing field is suddenly removed, the protons precess about the Earth's field like a spinning top; the Earth's field supplies the precessing force corresponding to that of gravity in the case of a top. The analogy is illustrated in Figure 3.9. The protons precess at an angular velocity ω , known as the *Larmor precession frequency*, which is proportional to the magnetic field F , so that

$$\omega = \gamma_p F \quad (3.30a)$$

The constant γ_p is the *gyromagnetic ratio of the proton*, the ratio of its magnetic moment to its spin angular momentum. The value of γ_p is known to an accuracy of 0.001%. Since precise frequency measurements are relatively easy, the magnetic field can be determined to the same accuracy. The proton, which is a moving charge, induces, in a coil surrounding the sample, a voltage that varies at the precession frequency ν . Thus we can determine the magnetic field from

$$F = 2\pi\nu/\gamma_p \quad (3.30b)$$

where the factor $2\pi/\gamma_p = 23.487 \pm 0.002$ nT/Hz. Only the total field may be measured.

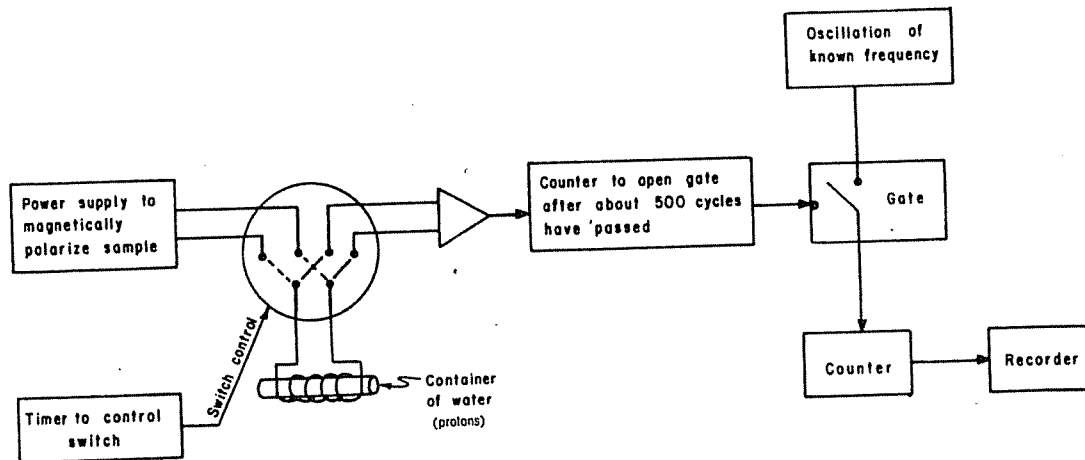


Figure 3.10. Proton-precession magnetometer. (From Sheriff, 1984.)

The essential components of this magnetometer include a source of protons, a polarizing magnetic field considerably stronger than that of the Earth and directed roughly normal to it (the direction of this field can be off by 45°), a pickup coil coupled tightly to the source, an amplifier to boost the minute voltage induced in the pickup coil, and a frequency-measuring device. The latter operates in the audio range because, from Equation (3.30b), $\nu = 2130 \text{ Hz}$ for $F_e = 50,000 \text{ nT}$. It must also be capable of indicating frequency differences of about 0.4 Hz for an instrument sensitivity of 10 nT.

The proton source is usually a small bottle of water (the nuclear moment of oxygen is zero) or some organic fluid rich in hydrogen, such as alcohol. The polarizing field of 5 to 10 mT is obtained by passing direct current through a solenoid wound around the bottle, which is oriented roughly east-west for the measurement. When the solenoid current is abruptly cut off, the proton precession about the Earth's field is detected by a second coil as a transient voltage building up and decaying over an interval of $\sim 3 \text{ s}$, modulated by the precession frequency. In some models the same coil is used for both polarization and detection. The modulation signal is amplified to a suitable level and the frequency measured. A schematic diagram is shown in Figure 3.10.

The measurement of frequency may be carried out by actually counting precession cycles in an exact time interval, or by comparing them with a very stable frequency generator. In one ground model, the precession signal is mixed with a signal from a local oscillator of high precision to produce low-frequency beats ($\approx 100 \text{ Hz}$) that drive a vibrating reed frequency meter. Regardless of the method used, the frequency must be measured to an accuracy of 0.001% to realize the capabilities of the method. Although this is not particularly difficult in

a fixed installation, it posses some problems in small portable equipment.

The proton-precession magnetometer's sensitivity ($\approx 1 \text{ nT}$) is high, and it is essentially free from drift. The fact that it requires no orientation or leveling makes it attractive for marine and airborne operations. It has essentially no mechanical parts, although the electronic components are relatively complex. The main disadvantage is that only the total field can be measured. It also cannot record continuously because it requires a second or more between readings. In an aircraft traveling at 300 km/hr, the distance interval is about 100 m. Proton-precession magnetometers are now the dominant instrument for both ground and airborne applications.

3.4.4. Optically Pumped Magnetometer

A variety of scientific instruments and techniques has been developed using the energy in transferring atomic electrons from one energy level to another. For example, by irradiating a gas with light or radio-frequency waves of the proper frequency, electrons may be raised to a higher energy level. If they can be accumulated in such a state and then suddenly returned to a lower level, they release some of their energy in the process. This energy may be used for amplification (masers) or to get an intense light beam, such as that produced by a laser.

The optically pumped magnetometer is another application. The principle of operation may be understood from an examination of Figure 3.11a, which shows three possible energy levels, A_1 , A_2 , and B for a hypothetical atom. Under normal conditions of pressure and temperature, the atoms occupy ground state levels A_1 and A_2 . The energy difference between A_1 and A_2 is very small [$\approx 10^{-8} \text{ electron volts (eV)}$], representing a fine structure due to atomic electron spins that normally are not all aligned in the

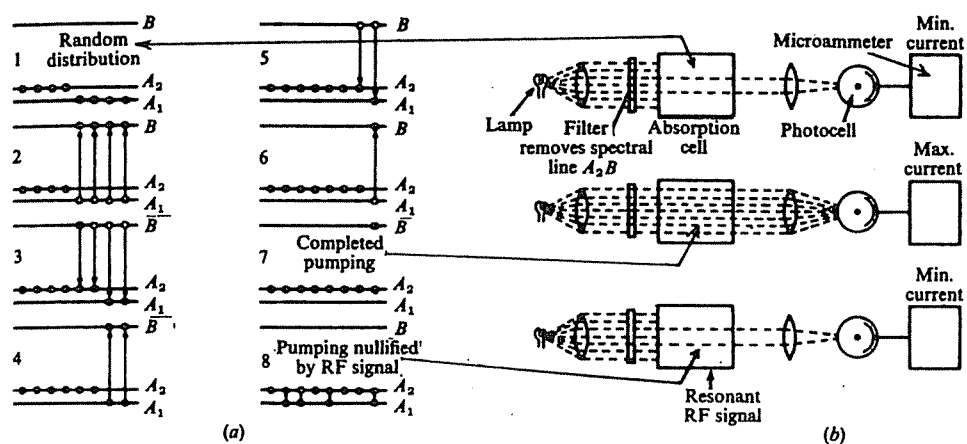


Figure 3.11. Optical pumping. (a) Energy level transitions. (b) Effect of pumping on light transmission.

same direction. Even thermal energies ($\approx 10^{-2}$ eV) are much larger than this, so that the atoms are as likely to be in level A_1 as in A_2 .

Level B represents a much higher energy and the transitions from A_1 or A_2 to B correspond to infrared or visible spectral lines. If we irradiate a sample with a beam from which spectral line A_2B has been removed, atoms in level A_1 can absorb energy and rise to B , but atoms in A_2 will not be excited. When the excited atoms fall back to ground state, they may return to either level, but if they fall to A_1 , they will be removed by photon excitation to B again. The result is an accumulation of atoms in level A_2 .

The technique of overpopulating one energy level in this fashion is known as *optical pumping*. As the atoms are moved from level A_1 to A_2 by this selective process, less energy will be absorbed and the sample becomes increasingly transparent to the irradiating beam. When all atoms are in the A_2 state, a photosensitive detector will register a maximum current, as shown in Figure 3.11b. If now we apply an RF signal, having energy corresponding to the transition between A_1 and A_2 , the pumping effect is nullified and the transparency drops to a minimum again. The proper frequency for this signal is given by $\nu = E/h$, where E is the energy difference between A_1 and A_2 and h is Planck's constant [6.62×10^{-34} joule-seconds].

To make this device into a magnetometer, it is necessary to select atoms that have magnetic energy sublevels that are suitably spaced to give a measure of the weak magnetic field of the Earth. Elements that have been used for this purpose include cesium, rubidium, sodium, and helium. The first three each have a single electron in the outer shell whose spin axis lies either parallel or antiparallel to an external magnetic field. These two orientations correspond to

the energy levels A_1 and A_2 (actually the sublevels are more complicated than this, but the simplification illustrates the pumping action adequately), and there is a difference of one quantum of angular momentum between the parallel and antiparallel states. The irradiating beam is circularly polarized so that the photons in the light beam have a single spin axis. Atoms in sublevel A_1 then can be pumped to B , gaining one quantum by absorption, whereas those in A_2 already have the same momentum as B and cannot make the transition.

Figure 3.12 is a schematic diagram of the rubidium-vapor magnetometer. Light from the Rb lamp is circularly polarized to illuminate the Rb vapor cell, after which it is refocused on a photocell. The axis of this beam is inclined approximately 45° to the Earth's field, which causes the electrons to precess about the axis of the field at the Larmor frequency. At one point in the precession cycle the atoms will be most nearly parallel to the light-beam direction and one-half cycle later they will be more antiparallel. In the first position, more light is transmitted through the cell than in the second. Thus the precession frequency produces a variable light intensity that flickers at the Larmor frequency. If the photocell signal is amplified and fed back to a coil wound on the cell, the coil-amplifier system becomes an oscillator whose frequency ν is given by

$$F = 2\pi\nu/\gamma_e \quad (3.31)$$

where γ_e is the gyromagnetic ratio of the electron.

For Rb, the value of $\gamma_e/2\pi$ is approximately 4.67 Hz/nT whereas the corresponding frequency for $F_e = 50,000$ nT is 233 kHz. Because γ_e for the electron is known to a precision of about 1 part in 10^7 and because of the relatively high frequencies involved, it

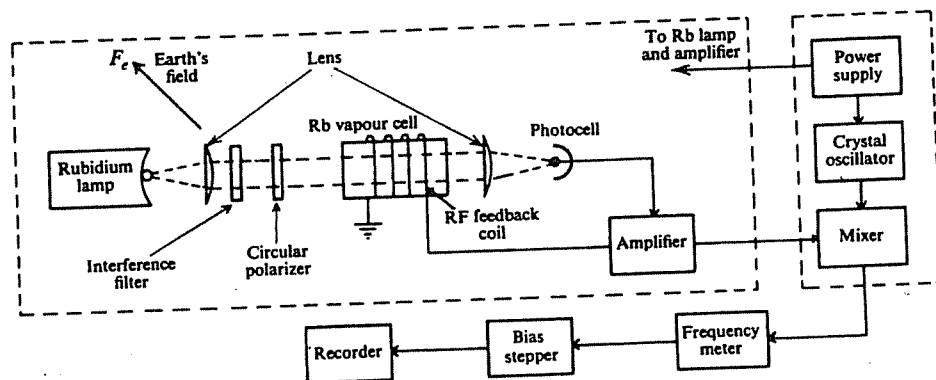


Figure 3.12. Rubidium-vapor magnetometer (schematic).

is not difficult to measure magnetic field variations as small as 0.01 nT with a magnetometer of this type.

3.4.5. Gradiometers

The sensitivity of the optically pumped magnetometer is considerably greater than normally required in prospecting. Since 1965, optically pumped rubidium- and cesium-vapor magnetometers have been increasingly employed in airborne gradiometers. Two detectors, vertically separated by about 35 m, measure dF/dz , the total-field vertical gradient. The sensitivity is reduced by pitch and yaw of the two birds. Major improvements by the Geological Survey of Canada involve reducing the vertical separation to 1 to 2 m and using a more rigid connection between the sensors. Gradient measurements are also made in ground surveys. The two sensors on a staff in the Scintrex MP-3 proton-magnetometer system, for example, measure the gradient to ± 0.1 nT/m. Gradiometer surveys are discussed further in Section 3.5.5.

3.4.6. Instrument Recording

Originally the magnetometer output in airborne installations was displayed by pen recorder. To achieve both high sensitivity and wide range, the graph would be "paged back" (the reference value changed) frequently to prevent the pen from running off the paper. Today recording is done digitally, but generally an analog display is also made during a survey. Some portable instruments for ground work also digitally record magnetometer readings, station coordinates, diurnal corrections, geological and terrain data.

3.4.7. Calibration of Magnetometers

Magnetometers may be calibrated by placing them in a suitably oriented variable magnetic field of known value. The most dependable calibration

method employs a *Helmholtz coil* large enough to surround the instrument. This is a pair of identical coils of N turns and radii a coaxially spaced a distance apart equal to the radius. The resulting magnetic field, for a current I flowing through the coils connected in series-aiding, is directed along the axis and is uniform within about 6% over a cylinder of diameter a and length $3a/4$, concentric with the coils. This field is given by

$$H \approx 9.0NI/a \quad (3.32a)$$

where I is in microamperes, H in nanoteslas, and a in meters. Because H varies directly with the current, this can be written

$$\Delta H = 9.0N\Delta I/a \quad (3.32b)$$

3.5. FIELD OPERATIONS

3.5.1. General

Magnetic exploration is carried out on land, at sea, and in the air. For areas of appreciable extent, surveys usually are done with the airborne magnetometer.

In oil exploration, airborne magnetics (along with surface gravity) is done as a preliminary to seismic work to establish approximate depth, topography, and character of the basement rocks. Since the susceptibilities of sedimentary rocks are relatively small, the main response is due to igneous rocks below (and sometimes within) the sediments.

Within the last few years it has become possible to extract from aeromagnetic data weak anomalies originating in sedimentary rocks, such as result from the faulting of sandstones. This results from (a) the improved sensitivity of magnetometers, (b) more precise determination of location with Doppler radar (§B.5), (c) corrections for diurnal and other temporal

field variations, and (d) computer-analysis techniques to remove noise effects.

Airborne reconnaissance for minerals frequently combines magnetics with airborne EM. In most cases of followup, detailed ground magnetic surveys are carried out. The method is usually indirect, that is, the primary interest is in geological mapping rather than the mineral concentration per se. Frequently the association of characteristic magnetic anomalies with base-metal sulfides, gold, asbestos, and so on, has been used as a marker in mineral exploration. There is also, of course, an application for magnetics in the direct search for certain iron and titanium ores.

3.5.2. Airborne Magnetic Surveys

(a) *General.* In Canada and some other countries, government agencies have surveyed much of the country and aeromagnetic maps on a scale of 1 mile to the inch are available at a nominal sum. Large areas in all parts of the world have also been surveyed in the course of oil and mineral exploration.

The sensitivity of airborne magnetometers is generally greater than those used in ground exploration – about 0.01 nT compared with 10 to 20 nT. Because of the initial large cost of the aircraft and availability of space, it is practical to use more sophisticated equipment than could be handled in portable instruments; their greater sensitivity is useful in making measurements several hundred meters above the ground surface, whereas the same sensitivity is usually unnecessary (and may even be undesirable) in ground surveys.

(b) *Instrument mounting.* Aside from stabilization, there are certain problems in mounting the sensitive magnetic detector in an airplane, because the latter has a complicated magnetic field of its own. One obvious way to eliminate these effects is to tow the sensing element some distance behind the aircraft. This was the original mounting arrangement and is still used. The detector is housed in a streamlined cylindrical container, known as a *bird*, connected by a cable 30 to 150 m long. Thus the bird may be 75 m nearer the ground than the aircraft. A photograph of a bird mounting is shown in Figure 3.13a.

An alternative scheme is to mount the detector on a wing tip or slightly behind the tail. The stray magnetic effects of the plane are minimized by permanent magnets and soft iron or permalloy shielding strips, by currents in compensating coils, and by metallic sheets for electric shielding of the eddy currents. The shielding is a cut-and-try process, since the magnetic effects vary with the aircraft and

mounting location. Figure 3.13b shows an installation with the magnetometer head in the tail.

(c) *Stabilization.* Since proton-precession and optically pumped magnetometers measure total field, the problem of stable orientation of the sensing element is minor. Although the polarizing field in the proton-precession instrument must not be parallel to the total-field direction, practically any other orientation will do because the signal amplitude becomes inadequate only within a cone of about 5°.

Stabilization of the fluxgate magnetometer is more difficult, because the sensing element must be maintained accurately in the *F* axis. This is accomplished with two additional fluxgate detectors that are oriented orthogonally with the first; that is, the three elements form a three-dimensional orthogonal coordinate system. The set is mounted on a small platform that rotates freely in all directions. When the sensing fluxgate is accurately aligned along the total-field axis, there is zero signal in the other two. Any tilt away from this axis produces a signal in the control elements that drive servomotors to restore the system to the proper orientation.

(d) *Flight pattern.* Aeromagnetic surveys almost always consist of parallel lines (Fig. 3.13c) spaced anywhere from 100 m to several kilometers apart. The heading generally is normal to the main geologic trend in the area and altitude usually is maintained at fixed elevations, the height being continuously recorded by radio or barometric altimeters. It is customary to record changes in the Earth's field with time (due to diurnal or more sudden variations) with a recording magnetometer on the ground. A further check generally is obtained by flying several cross lines, which verify readings at line intersections.

A *drape survey*, which approximates constant clearance over rough topography, is generally flown with a helicopter. It is often assumed that drape surveys minimize magnetic terrain effects, but Grauch and Campbell (1984) dispute this. Using a uniformly magnetized model of a mountain-valley system, four profiles (one level, the others at different ground clearance) all showed terrain effects. However, Grauch and Campbell recommend drape surveys over level-flight surveys because of greater sensitivity to small targets, particularly in valleys. The disadvantages of draped surveys are higher cost, operational problems, and less sophisticated interpretation techniques.

(e) *Effect of variations in flight path.* Altitude differences between flight lines may cause herringbone patterns in the magnetic data. Bhattacharyya (1970) studied errors arising from flight deviations

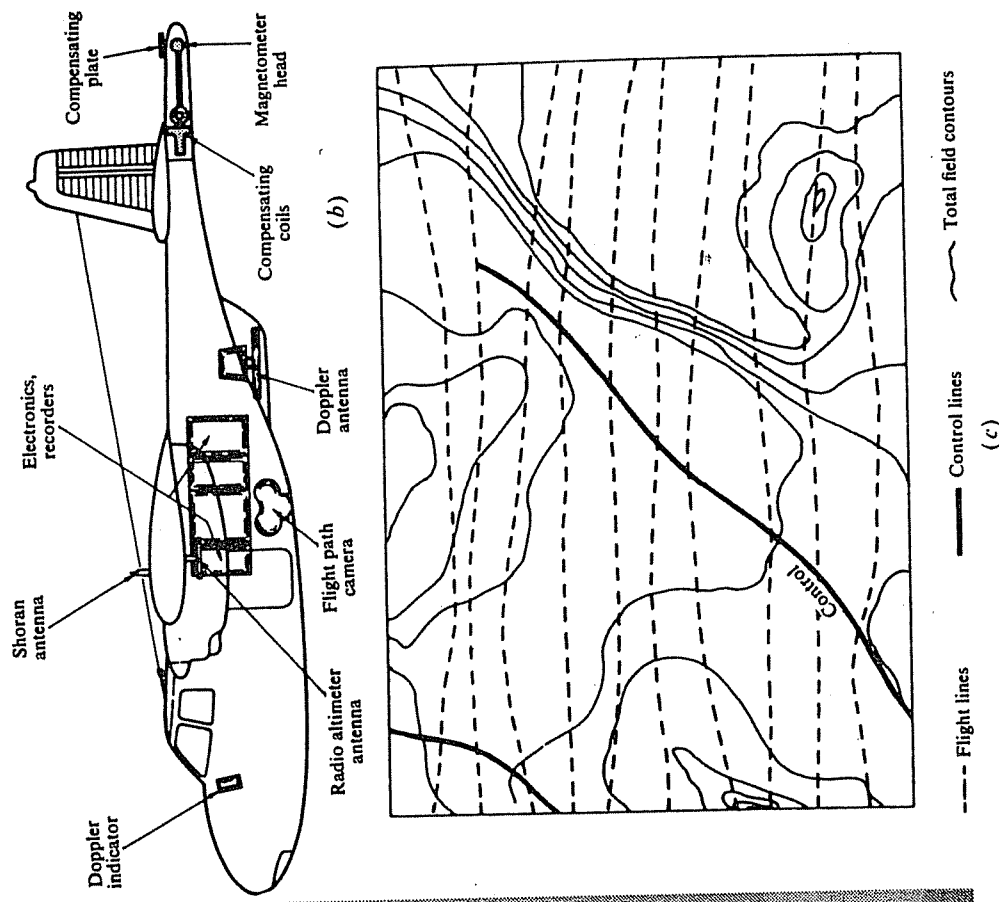
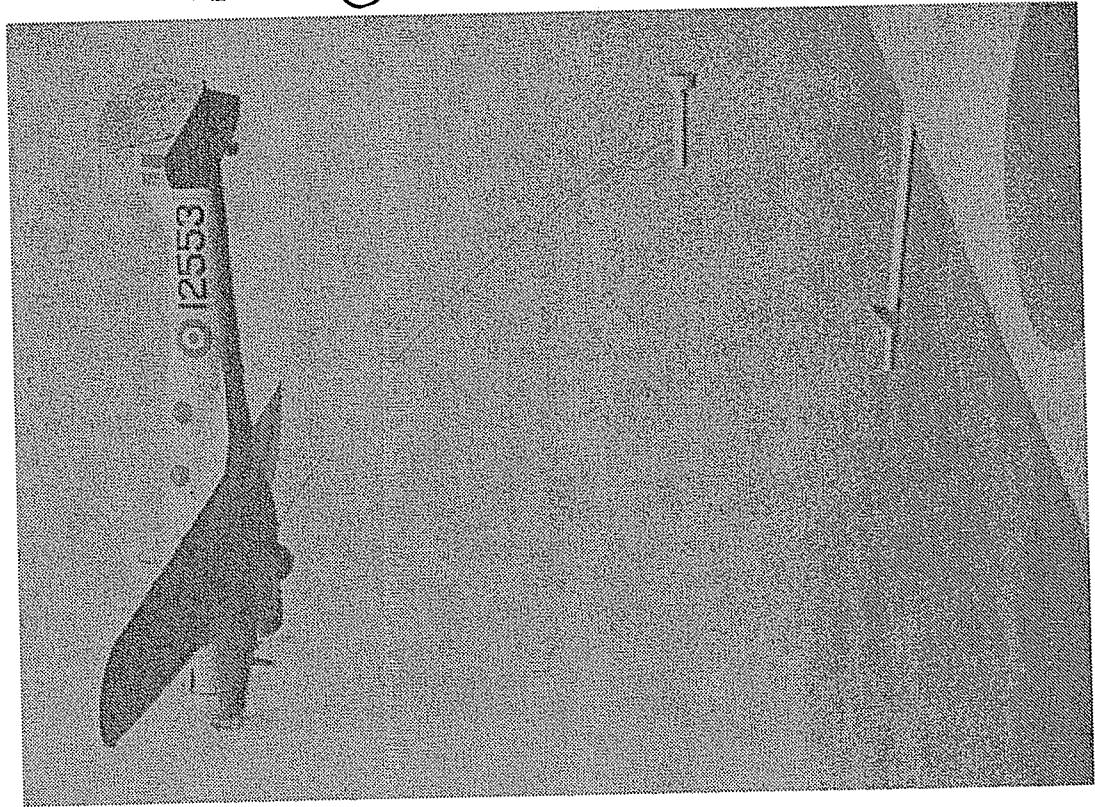


Figure 3.13. Airborne magnetics. (a) Magnetometer in a bird. (b) Magnetometer in a tail mounting. (c) Flight pattern and magnetic map.

over an idealized dike (prism) target. Altitude and heading changes produced field measurement changes that would alter interpretations based on anomaly shape measurements, such as those of slope. Such deviations are especially significant with high-resolution data.

(f) *Aircraft location.* The simplest method of locating the aircraft at all times, with respect to ground location, is for the pilot to control the flight path by using aerial photographs, while a camera takes photos on strip film to determine locations later. The photos and magnetic data are simultaneously tagged at intervals. Over featureless terrain, radio navigation (see §B.6) gives aircraft position with respect to two or more ground stations, or Doppler radar (§B.5) determines the precise flight path. Doppler radar increasingly is employed where high accuracy is required.

(g) *Corrections to magnetic data.* Magnetic data are corrected for drift, elevation, and line location differences at line intersections in a least-squares manner to force ties. Instrument drift is generally not a major problem, especially with proton and optically pumped magnetometers whose measurements are absolute values.

The value of the main magnetic field of the Earth is often subtracted from measurement values. The Earth's field is usually taken to be that of the *International Geomagnetic Reference Field* (IGRF) model.

A stationary base magnetometer is often used to determine slowly varying diurnal effects. Horizontal gradiometer arrangements help in eliminating rapid temporal variations; the gradient measurements do not involve diurnal effects. Usually no attempt is made to correct for the large effects of magnetic storms.

(h) *Advantages and disadvantages of airborne magnetics.* Airborne surveying is extremely attractive for reconnaissance because of low cost per kilometer (see Table 1.2) and high speed. The speed not only reduces the cost, but also decreases the effects of time variations of the magnetic field. Erratic near-surface features, frequently a nuisance in ground work, are considerably reduced. The flight elevation may be chosen to favor structures of certain size and depth. Operational problems associated with irregular terrain, sometimes a source of difficulty in ground magnetics, are minimized. The data are smoother, which may make interpretation easier. Finally, aeromagnetics can be used over water and in regions inaccessible for ground work.

The disadvantages in airborne magnetics apply mainly to mineral exploration. The cost for survey-

ing small areas may be prohibitive. The attenuation of near-surface features, apt to be the survey objective, become limitations in mineral search.

3.5.3. Shipborne Magnetic Surveys

Both the fluxgate and proton-precession magnetometers have been used in marine operations. There are no major problems in ship installation. The sensing element is towed some distance (150 to 300 m) astern (to reduce magnetic effects of the vessel) in a watertight housing called a *fish*, which usually rides about 15 m below the surface. Stabilization is similar to that employed in the airborne bird. Use of a ship rather than an aircraft provides no advantage and incurs considerable cost increase unless the survey is carried out in conjunction with other surveys, such as gravity or seismic. The main application has been in large-scale oceanographic surveying related to earth physics and petroleum search. Much of the evidence supporting plate tectonics has come from marine magnetics.

3.5.4. Ground Magnetic Surveys

(a) *General.* Magnetic surveying on the ground now almost exclusively uses the portable proton-precession magnetometer. The main application is in detailed surveys for minerals, but ground magnetics are also employed in the followup of geochemical reconnaissance in base-metal search. Station spacing is usually 15 to 60 m; occasionally it is as small as 1 m. Most ground surveys now measure the total field, but vertical-component fluxgate instruments are also used. Sometimes gradiometer measurements (§3.5.5) are made.

(b) *Corrections.* In precise work, either repeat readings should be made every few hours at a previously occupied station or a base-station recording magnetometer should be employed. This provides corrections for diurnal and erratic variations of the magnetic field. However, such precautions are unnecessary in most mineral prospecting because anomalies are large (> 500 nT).

Since most ground magnetometers have a sensitivity of about 1 nT, stations should not be located near any sizeable objects containing iron, such as railroad tracks, wire fences, drill-hole casings, or culverts. The instrument operator should also not wear iron articles, such as belt buckles, compasses, knives, iron rings, and even steel spectacle frames.

Apart from diurnal effects, the reductions required for magnetic data are insignificant. The vertical gradient varies from approximately 0.03 nT/m at the poles to 0.01 nT/m at the magnetic equator. The

latitude variation is rarely $> 6 \text{ nT/km}$. Thus elevation and latitude corrections are generally unnecessary.

The influence of topography on ground magnetics, on the other hand, can be very important. This is apparent when taking measurements in stream gorges, for example, where the rock walls above the station frequently produce abnormal magnetic lows. Terrain anomalies as large as 700 nT occur at steep (45°) slopes of only 10 m extent in formations containing 2% magnetite ($k = 0.025 \text{ SI unit}$) (Gupta and Fitzpatrick, 1971). In such cases, a terrain correction is required, but it cannot be applied merely as a function of topography alone because there are situations (for example, sedimentary formations of very low susceptibility) in which no terrain distortion is observed.

A terrain smoothing correction may be carried out by reducing measurements from an irregular surface $z = h(x, y)$ to a horizontal plane, say $z = 0$, above it. This can be done approximately by using a Taylor series (§A.5) with two terms:

$$Z(x, y, 0) = Z(x, y, h) - h(\partial Z / \partial z)_{z=h} \quad (3.33)$$

3.5.5. Gradiometer Surveys

The gradient of F is usually calculated from the magnetic contour map with the aid of templates. There is, however, considerable merit in measuring the vertical gradient directly in the field. It is merely necessary to record two readings, one above the other. With instrument sensitivity of 1 nT, an elevation difference of $\approx 1 \text{ m}$ suffices. Then the vertical gradient is given by

$$\partial F / \partial z = (F_2 - F_1) / \Delta z$$

where F_1 and F_2 are readings at the higher and lower elevations, and Δz is the separation distance.

Discrimination between neighboring anomalies is enhanced in the gradient measurements. For example, the anomalies for two isolated poles at depth h separated by a horizontal distance h yield separate peaks on a $\partial F / \partial z$ profile but they have to be separated by $1.4 h$ to yield separate anomalies on an F profile. The effect of diurnal variations is also minimized, which is especially beneficial in high magnetic latitudes. For most of the simple shapes discussed in Section 3.6 (especially for the isolated pole, finite-length dipole, and vertical contact of great depth extent), better depth estimates can be made from the first vertical-derivative profiles than from either the Z or F profiles. For features of the first two types, the width of the profile at $(\partial Z / \partial z)_{\max}/2$ equals the depth within a few per-

cent. For the vertical contact, half the separation between maximum and minimum values equals the depth. Gradiometer measurements are valuable in field continuation calculations (§3.7.5).

Ground gradiometer measurements (Hood and McClure, 1965) have recently been carried out for gold deposits in eastern Canada in an area where the overburden is only a few meters thick. The host quartz was located because of its slightly negative susceptibility using a vertical separation of 2 m and a station spacing of $\approx 1 \text{ m}$. Gradiometer surveys have also been used in the search for archeological sites and artifacts, mapping buried stone structures, forges, kilns, and so forth (Clark, 1986; Wynn, 1986).

Vertical gradient aeromagnetic surveys (Hood, 1965) are often carried out at 150 to 300 m altitude. Detailed coverage with 100 to 200 m line spacing is occasionally obtained at 30 m ground clearance.

Two magnetometers horizontally displaced from each other are also used, especially with marine measurements where they may be separated by 100 to 200 m. This arrangement permits the elimination of rapid temporal variations so that small spatial anomalies can be interpreted with higher confidence.

3.6. MAGNETIC EFFECTS OF SIMPLE SHAPES

3.6.1. General

Because ground surveys (until about 1968) measured the vertical-field component, whereas airborne surveys measured the total field, both vertical-component and total-field responses will be developed. Depth determinations are most important and lateral extent less so, whereas dip estimates are the least important and quite difficult. In this regard, aeromagnetic and electromagnetic interpretation are similar. In petroleum exploration the depth to basement is the prime concern, whereas in mineral exploration more detail is desirable. The potentialities of high resolution and vertical-gradient aeromagnetics are only now being exploited to a limited extent.

As in gravity and electromagnetics, anomalies are often matched with models. The magnetic problem is more difficult because of the dipole character of the magnetic field and the possibility of remanence. Very simple geometrical models are usually employed: isolated pole, dipole, lines of poles and dipoles, thin plate, dike (prism), and vertical contact. Because the shape of magnetic anomalies relates to the magnetic field, directions in the following sections are with respect to magnetic north (the x direction), magnetic east, and so forth, the z axis is positive downward, and we assume that locations are in the northern hemisphere. We use I for the field inclination, ξ for

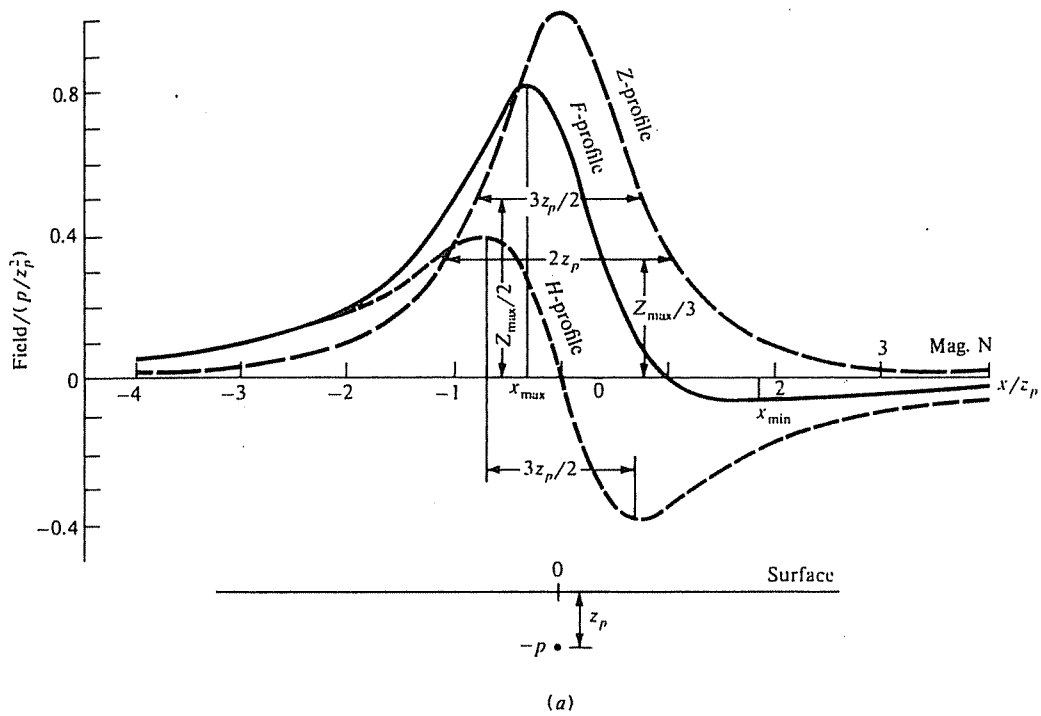


Figure 3.14. Magnetic effects of an isolated pole. (a) F , Z , and H profiles for $I = 45^\circ$.

the dip of bodies and β for the strike angle relative to magnetic north (x axis). Note that depths are measured with respect to the measurement elevation (the aircraft elevation for aeromagnetic measurements).

3.6.2. The Isolated Pole (Monopole)

Although an isolated pole is a fiction, in practice it may be used to represent a steeply dipping dipole whose lower pole is so far away that it has a negligible effect. The induced magnetization in a long, slender, near-vertical body tends to be along the axis of the body except near the magnetic equator. If the length of the body is large, we have, in effect, a single negative pole $-p$ located at $(0, 0, z_p)$.

From Equation (3.2) or Equations (3.9) and (3.11), we get for the field at $P(x, y, 0)$,

$$\mathbf{F}_p = (-p/r^2)\mathbf{r}_1 = (p/r^3)(-x\mathbf{i} - y\mathbf{j} + z_p\mathbf{k})$$

where \mathbf{r}_1 is a unit vector from $P(x, y, 0)$ toward the pole $-p$. The vertical anomaly is

$$Z = (pz_p/r^3) \quad (3.34a)$$

Usually the field of the pole, \mathbf{F}_p , is much smaller than the field of the Earth, \mathbf{F}_e , and the total field

anomaly is approximately the component of \mathbf{F}_p in the \mathbf{F}_e direction. Using Equation (3.29),

$$F \approx \mathbf{F}_p \cdot \mathbf{f}_1 = (p/r^3)(-x \cos I + z_p \sin I) \quad (3.34b)$$

[Note that the total field anomaly F , which is only a component of \mathbf{F}_p , may be smaller than Z , and that in general $F \neq (Z^2 + H^2)^{1/2}$.]

Profiles are shown in Figure 3.14a for $I = 45^\circ$; Z_{\max} is located directly over the pole. The H profile is perfectly asymmetric and its positive half intersects the Z profile nearly at $Z_{\max}/3$. The horizontal distance between positive and negative peaks of H is approximately $3z_p/2$. This profile is independent of the traverse direction only if the effect of the pole is much larger than the horizontal component of the Earth's field.

A set of total-field profiles for various values of I is shown in Figure 3.14c. F_{\max} occurs south of the monopole and F_{\min} north of it. F is zero north of the pole at $x = z \tan I$. The curves would be reflected in the vertical axis in southern latitudes. A total-field profile on a magnetic meridian becomes progressively more asymmetric as the inclination decreases (that is, as we move toward the magnetic equator). At the same time, the maximum decreases and the minimum increases and both are displaced progressively southward. The statement also applies

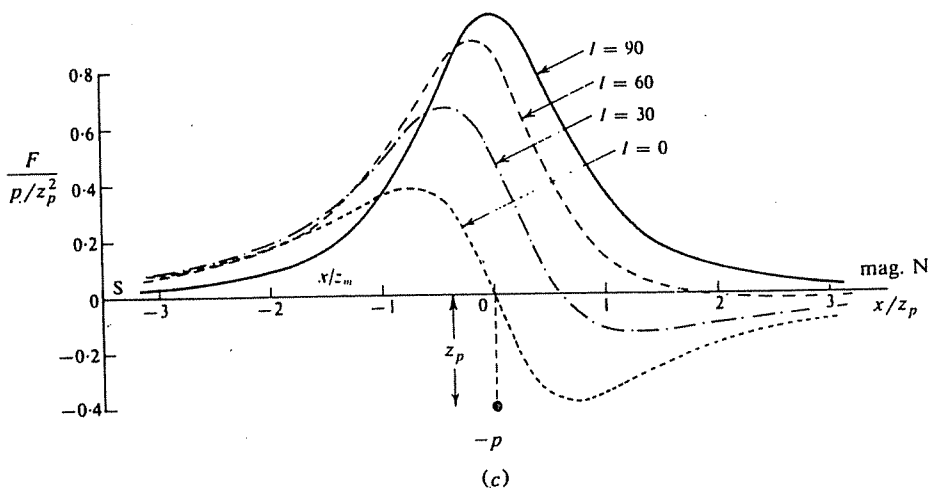
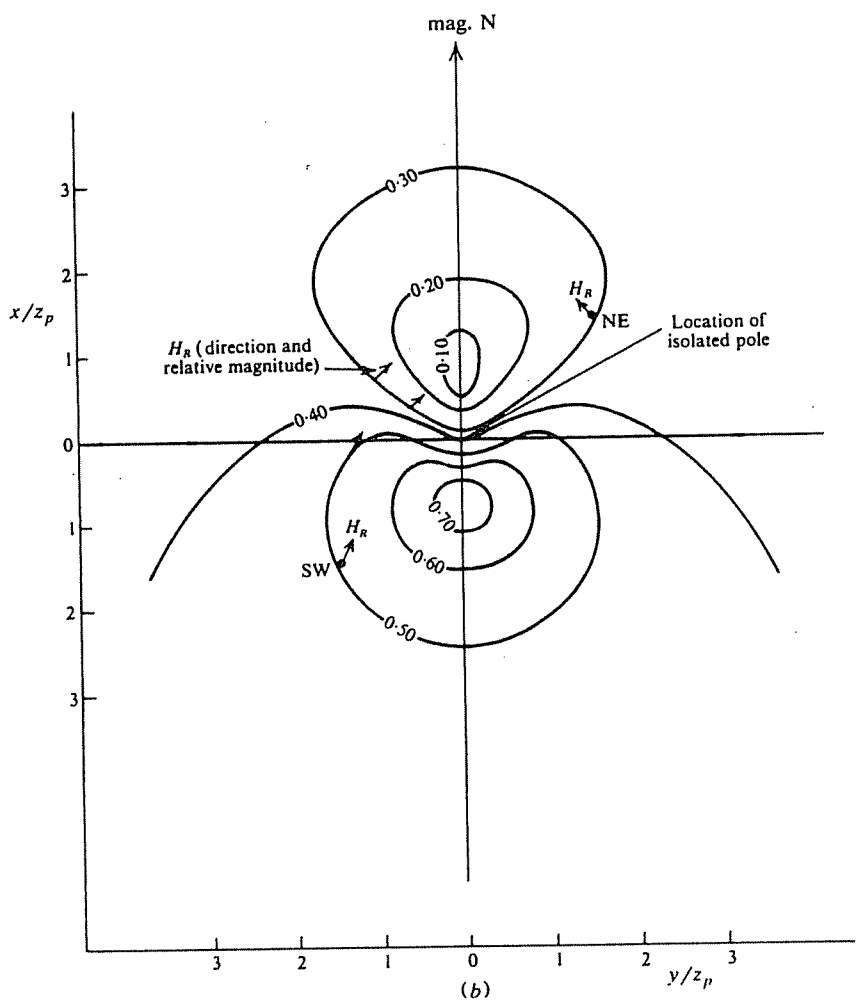


Figure 3.14. (Continued) (b) Contours of $|H_R| = |H + H_e|$ for $H_{\max} = H_e = 0.38$. (c) F profiles for various inclinations. (After Smellie, 1967.)

to the southern hemisphere if we interchange maximum and minimum.

The maximum and minimum values of F in Equation (3.34b) occur at

$$x_{\max, \min} = z_p \{ 3 \pm (9 + 8 \cot^2 I)^{1/2} \} / 4 \cot I \quad (3.35a)$$

where the plus sign gives F_{\max} . The maximum and minimum values of F (recalling that the pole is $-p$, hence p is positive) are

$$F_{\max, \min} = (p \sin I / 4z_p^2) \{ 1 \pm (9 + 8 \cot^2 I)^{1/2} \} / \{ 1 + (x_{\max, \min} / z_p)^2 \}^{3/2} \quad (3.35b)$$

There are several relations between the profile characteristics and the pole depth. When $Z = Z_{\max}/2$, $x_{1/2} = 0.75z_p$ (Fig. 3.14a), and when $Z = Z_{\max}/3$, $x_{1/3} = z_p$, where $x_{1/2}$ and $x_{1/3}$ are the half-widths at $Z_{\max}/2$ and $Z_{\max}/3$, respectively. Pole depth may also be estimated from Equations (3.35). For example,

$$z_p = 2(x_{\min} - x_{\max}) / (8 + 9 \tan^2 I)^{1/2} \quad (3.36a)$$

$$= 4(x_0 - x_{\max}) / \{ \tan I + (8 + 9 \tan^2 I)^{1/2} \} \quad (3.36b)$$

It may be difficult to locate x_{\min} and x_0 in high latitudes, however, since the curves are practically symmetrical when $I > 60^\circ$. An alternative estimate, good within 10%, is given by $z_p \approx 1.4x_{1/2}$, where $x_{1/2}$ is the half-width of the F profile.

A first vertical-derivative profile provides a good depth estimate. The width of the profile at $(1/2)(\partial Z/\partial z)_{\max}$ is equal to z_p to within a few percent.

3.6.3. The Dipole

A small three-dimensional structure containing anomalous concentrations of magnetic materials and varying in section from rod-like to spherical often may be represented by a dipole model. The dipole field was developed in Section 3.2.3. Assuming that a structure is magnetized mainly by induction in the direction of the Earth's field, the dipole dip will be that of the inclination, and the magnetic response may be obtained from Equation (3.14). If the body's intrinsic field due to remanence is much larger than the external field (an unlikely case), the magnetic

response may also be obtained from these equations, replacing the inclination I with the dip of the dipole ξ .

Figure 3.15a shows the geometry. For a traverse in the dip direction, we find F , H , and Z by resolving F_r and F_θ in Equation (3.14a) along the dipole, the vertical, and the horizontal directions, respectively. Thus,

$$\begin{aligned} F &= F_r \cos \theta - F_\theta \sin \theta = (m/r^3) (3 \cos^2 \theta - 1) \\ &= (m/r^3) \{ 3 \cos^2(I + \phi) - 1 \} \\ &= (m/r^5) \{ (3 \cos^2 I - 1)x^2 - 6xz_m \sin I \cos I \\ &\quad + (3 \sin^2 I - 1)z_m^2 \} \end{aligned} \quad (3.37a)$$

$$\begin{aligned} Z &= -(F_r \sin \phi + F_\theta \cos \phi) \\ &= -(m/r^3) (2 \cos \theta \sin \phi + \sin \theta \cos \phi) \\ &= (m/r^5) \{ (2z_m^2 - x^2) \sin I - 3xz_m \cos I \} \end{aligned} \quad (3.37b)$$

$$\begin{aligned} H &= F_r \cos \phi - F_\theta \sin \phi \\ &= (m/r^3) (2 \cos \theta \cos \phi - \sin \theta \sin \phi) \\ &= (m/r^5) \{ (2x^2 - z_m^2) \cos I - 3xz_m \sin I \} \end{aligned} \quad (3.37c)$$

where $m = 2pl$ and z_m is the depth of the dipole below the surface of measurement.

Profiles are shown in Figure 3.15b for $I = 45^\circ$. The dipole curves are somewhat sharper than for the monopole. The width, x^* , of the Z curves in Figure 3.15b at $\sim Z_{\max}/2$ is $x^* \approx z_m$. The same relation holds for the F curves in Figure 3.15b, e in the range $30^\circ \leq I \leq 90^\circ$. For $I = 0$, however, the profile is sharper and $x^* \approx 0.7z_m$ at $F_{\max}/2$. The F and Z profiles would be symmetrical on E-W traverses, with the flanks asymptotic to zero. The width of a gradiometer profile peak at $(1/2)(\partial Z/\partial z)_{\max}$ gives a good estimate of z_m .

When the dipole is polarized approximately vertically, which would be the case where $I \geq 70^\circ$, we have

$$F \approx Z = m(2z_m^2 - x^2)/r^5 \quad \text{and} \quad H = -3mxz_m/r^5 \quad (3.38a)$$

Near the magnetic equator, $I \approx 0$ and

$$F \approx H = m(2x^2 - z_m^2)/r^5 \quad \text{and} \quad Z = -3mxz_m/r^5 \quad (3.38b)$$

Curves for these limiting cases are shown in Figure 3.15c and d.

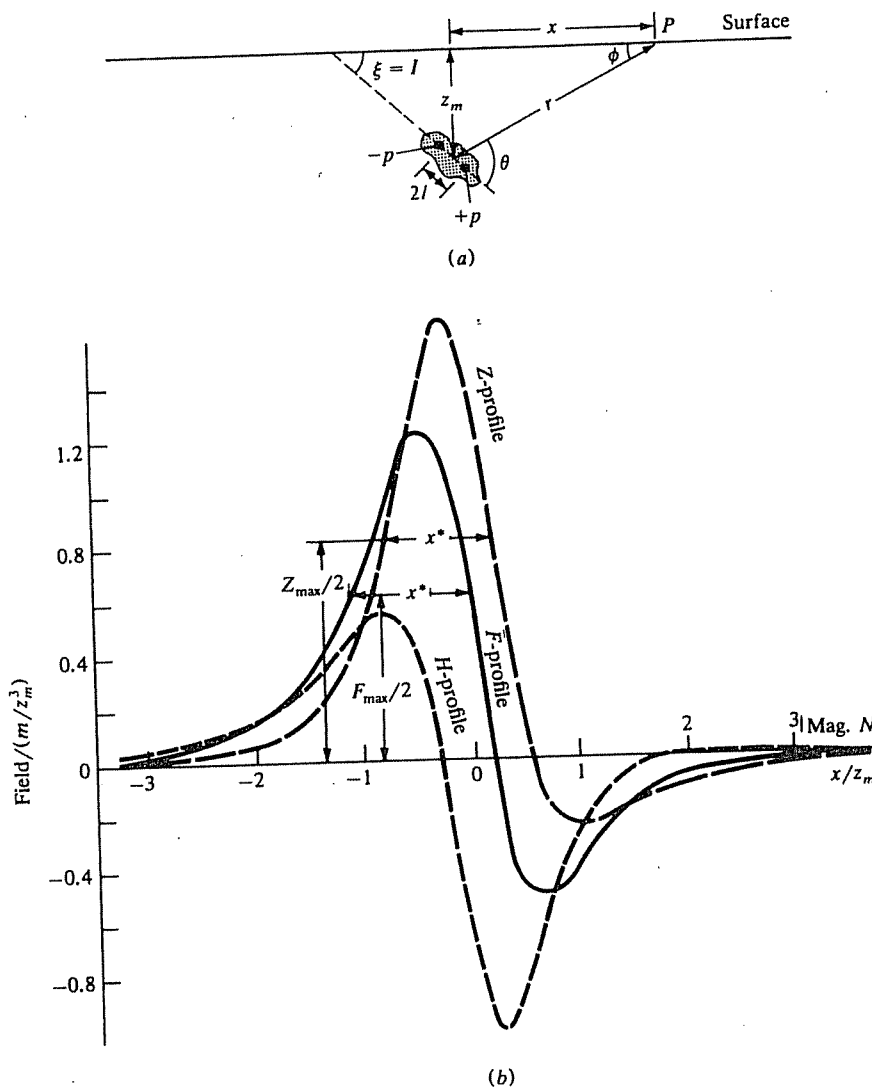


Figure 3.15. Magnetic effects of an isolated dipole. (a) Geometry. (b) Profiles for $I = 45^\circ$.

The following relations hold for the vertical dipole:

$$\left. \begin{array}{l} \text{At } x = 0, Z, F \text{ are maxima:} \\ Z_{\max} = F_{\max} = 2m/z_m^3 \\ \text{At } x = \pm 2z_m, Z, F \text{ are minima:} \\ Z_{\min} = F_{\min} = -0.036m/z_m^3 \\ \text{At } x = \pm z_m\sqrt{2} \quad Z = F = 0 \end{array} \right\} \quad (3.39a)$$

Similar relations hold for the horizontal dipole:

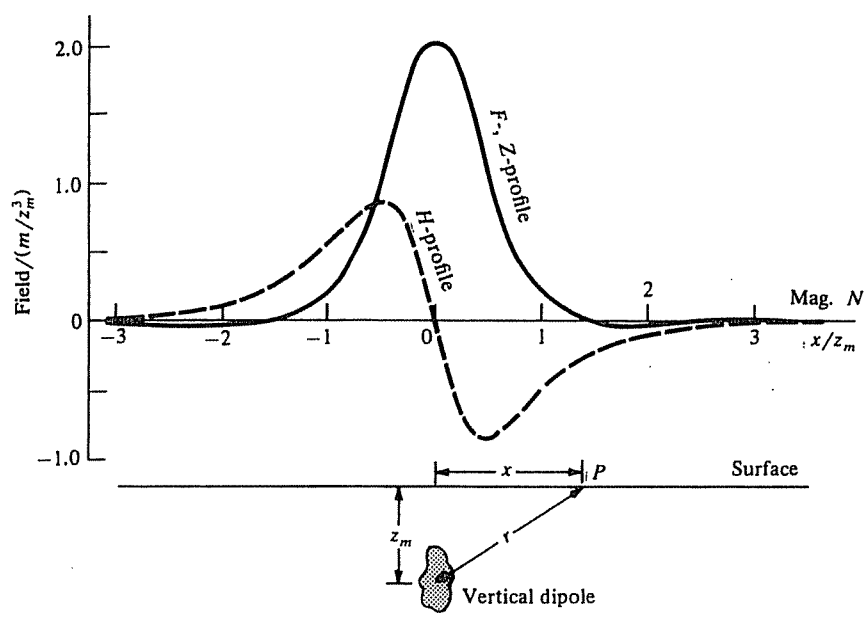
$$\left. \begin{array}{ll} \text{At } x = 0, & H_{\min} = F_{\min} = -m/z_m^3 \\ \text{At } x = \pm 1.2z_m, & H_{\max} = F_{\max} = 0.20m/z_m^3 \\ \text{At } x = \pm z_m/\sqrt{2}, & H = F = 0 \end{array} \right\} \quad (3.39b)$$

The direction of dipole dip is toward the side of the Z profile that has the steeper slope and negative tail. This tail is not pronounced, however, unless the dip $\xi < 50^\circ$. The F profiles are even more diagnostic of dip. In Figure 3.15d the Z profile is asymmetrical, with peak and trough above the ends of a long dipole for $z_m/l \ll 2$. When $z_m/l > 1$, the peak and trough occur beyond the ends and depth cannot be estimated, although a steep slope at the zero crossover would indicate a shallow source.

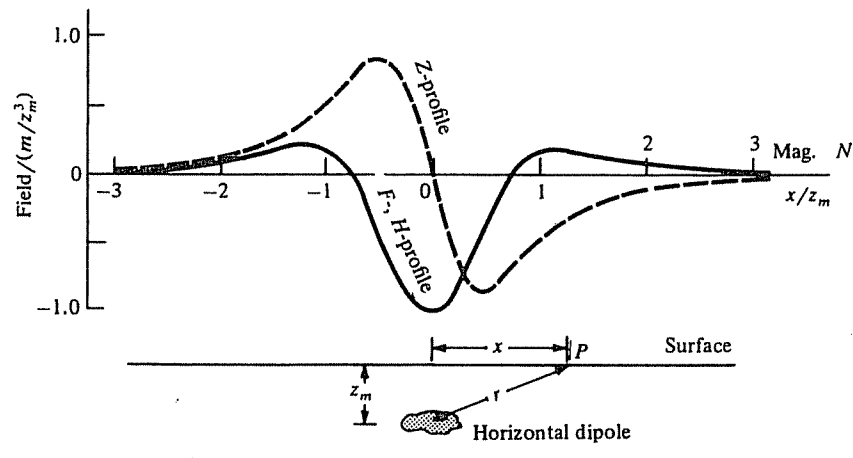
A finite dipole sometimes may be represented by a dipping sheet of finite length and depth extent [Eq. (3.58)] or by an infinite vertical dipping dike of finite strike length [Eq. (3.49)].

3.6.4. Two-Dimensional Features

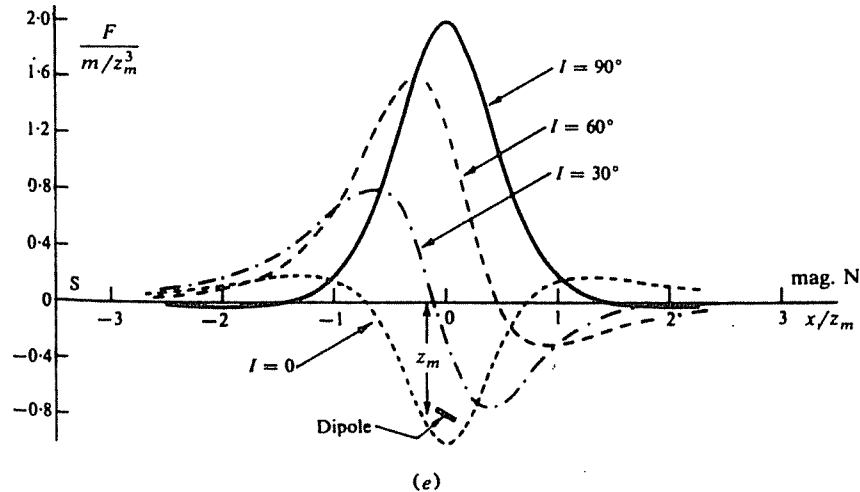
(a) General. Clearly the strike of a two-dimensional feature with respect to the earth's field will



(c)



(d)



(e)

Figure 3.15. (Continued) (c) Profiles for vertical dipole. (d) Profiles for horizontal dipole. (e) F profiles for different inclinations of field and dipole. (After Smellie, 1967.)

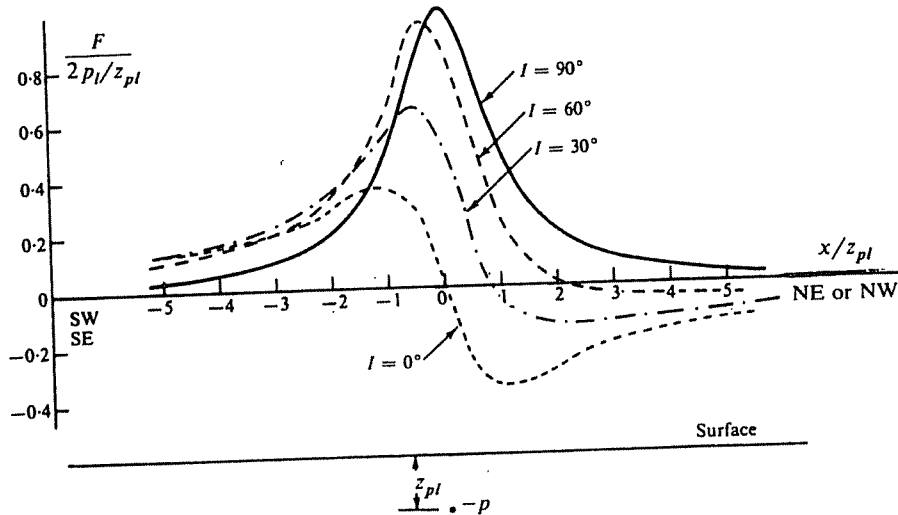


Figure 3.16. Total-field profiles normal to a line of poles striking NW–SE.

control induced magnetization, so the strike direction β will be incorporated in the expressions for various structures. Traverse direction is more critical in identifying a 2-D target. A profile approximately along strike will be unproductive. For 2-D models, it is customary to exhibit only *principal profiles* (normal to strike of the bodies). As in gravity, a magnetic body generally is considered to be 2-D when its strike length is at least 10 to 20 times larger than other dimensions. This situation is even less likely to be true in magnetics than it is in gravity, and formulas are often modified for finite strike length (Rasmussen and Pedersen, 1979).

In addition to using direct magnetic analysis, 2-D features may also be derived with relative ease from the corresponding gravity shapes by using Poisson's relation (§3.2.5).

(b) *Line of poles (thin vertical dike of infinite depth extent)*. An infinite horizontal line of poles is an approximation to a long shear or fracture zone or thin dike, which has appreciable susceptibility contrast and which extends to considerable depth. The magnetic potential is given by the logarithmic relation $A = -2p_l \ln(1/r)$, where $-p_l$ is the pole intensity per unit length [this equation comes from Eq. (3.9) following the procedure in problem 1, Chapter 2, and assuming infinitesimal cross section in Eq. (2.8)]. We pass a vertical plane through $P(x, y, 0)$ perpendicular to the line of poles and take x' and z' axes in this plane such that x' is horizontal, $z' = z$, and the line of poles intersects the z axis at a depth z_{pl} . β is the angle between the x and $-y'$ axes. The field \mathbf{F}_{pl} is in this plane and is directed down from P toward the line of poles along the vector $\mathbf{r} = (-x'\mathbf{i}' + z_{pl}\mathbf{k})$. To get derivatives of r at \mathbf{r}^2 in terms of the components of \mathbf{r} and p , we write \mathbf{r}^2 in terms of the components of \mathbf{r} and

temporarily replace $P(x', 0)$ with $P'(x', z)$. Then, $r^2 = (-x')^2 + (z_{pl} - z)^2$, $\partial r/\partial x = x'/r$, and $\partial r/\partial z = \lim_{z \rightarrow 0} \{-(z_{pl} - z)/r\} = -z_{pl}/r$. Then,

$$\begin{aligned} \mathbf{F}_{pl} &= -\nabla A = -2p_l \nabla \{\ln r\} \\ &= (2p_l/r^2)(-x'\mathbf{i}' + z_{pl}\mathbf{k}) \\ &= (2p_l/r^2)(-x' \sin \beta \mathbf{i} + z_{pl}\mathbf{k}) \end{aligned} \quad (3.40a)$$

Now the component along \mathbf{F}_e is

$$\begin{aligned} F &= \mathbf{F}_{pl} \cdot \mathbf{f}_1 \\ &= (2p_l/r^2)(-x' \sin \beta \mathbf{i} + z_{pl}\mathbf{k}) \\ &\quad \cdot (\cos I \mathbf{i} + \sin I \mathbf{k}) \\ &= (2p_l/r^2)(-x' \cos I \sin \beta + z_{pl} \sin I) \end{aligned} \quad (3.40b)$$

where $r^2 = x'^2 + z_{pl}^2$. The vertical component is

$$Z = 2p_l z_{pl}/r^2 \quad (3.40c)$$

The north-south component of H is from Equation (3.40a):

$$H = -(2p_l/r^2)x' \sin \beta \quad (3.40d)$$

Total-field principal profiles (normal to strike) are shown in Figure 3.16 for several inclinations and strike $\beta = 45^\circ$. Obviously the Z profiles are the same for any strike direction. The F curves in Figure 3.16 have the same character as for the single pole, although they are somewhat broader. For $I < 30^\circ$, the half-width of the profile at $F_{\max}/2$ is about equal to the depth. When I is smaller, the depth is roughly equal to half the horizontal distance between F_{\max} and F_{\min} .

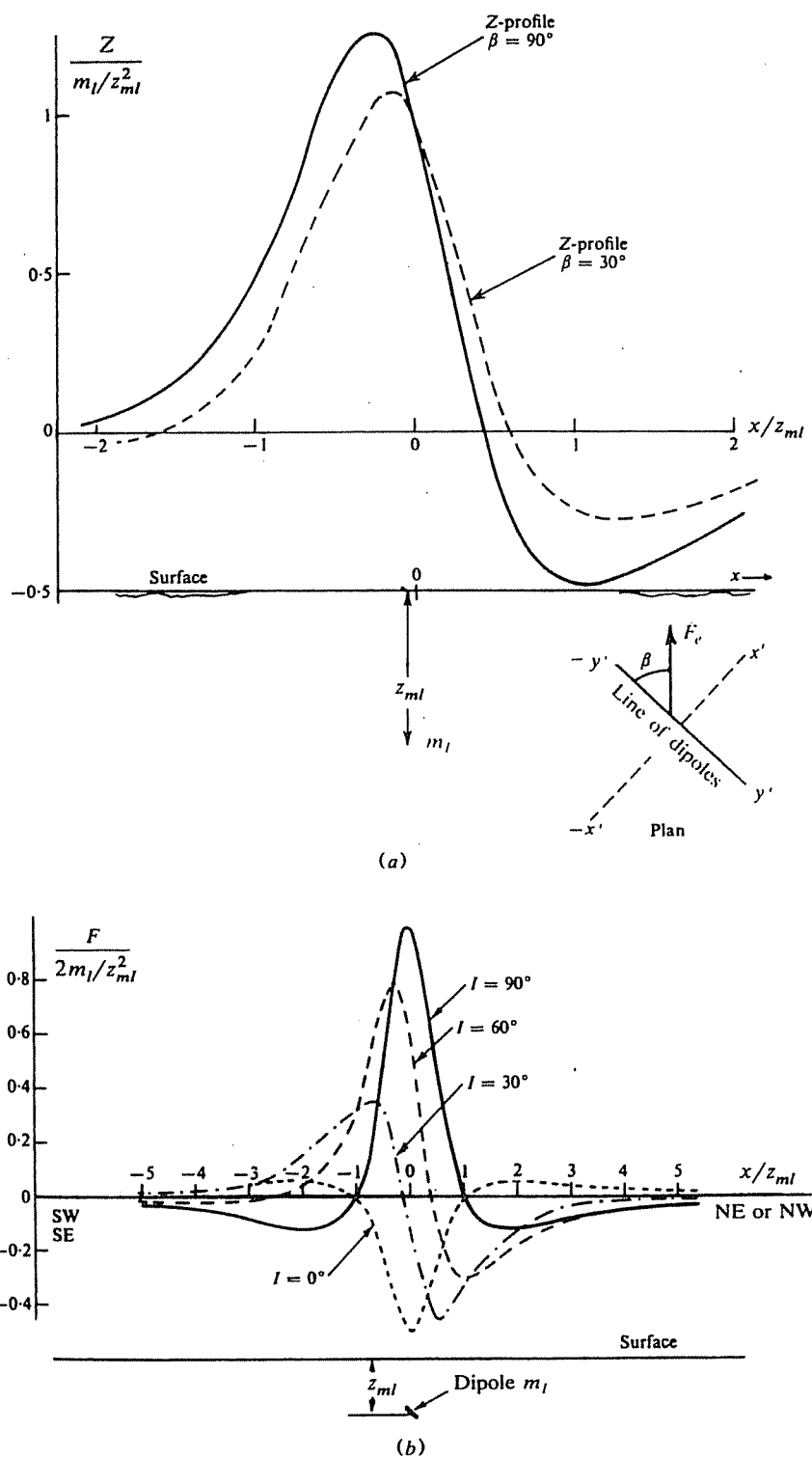


Figure 3.17. Profiles normal to a horizontal line of dipoles. (a) Vertical-field profiles, $I = 45^\circ$. (b) F profiles for $\beta = \pm 45^\circ$.

(c) *Line of dipoles (ribbon)*. The opposite extreme to a line of poles is a magnetic stringer of limited depth extent, which can be modeled by a line (ribbon) of dipoles, sometimes called a thin horizontal cylinder. We take the y' axis along the strike and derive the magnetic response along the principal profile (in the i' direction) using Poisson's relation [Eq. (3.26)]:

$$A = (m_l/\gamma\rho_l) g_a = -(m_l/\gamma\rho_l) \nabla U \cdot \alpha_l$$

where ρ_l is the density per unit length and m_l is the dipole moment per unit length in the direction $\alpha_l = -\cos I \sin \beta i' + \sin I k$. Then $U = -2\gamma\rho_l \ln(r)$ for infinitesimal cross section [Eq. (2.8)]; we now write $r^2 = x'^2 + (z_{ml} - z)^2$, differentiate, then set $z = 0$. This gives

$$\nabla U = -2\gamma\rho_l(x'i' - z_{ml}k)/r^2$$

The magnetic potential becomes

$$\begin{aligned} A &= \left\{ (-m_l/\gamma\rho_l)(-2\gamma\rho_l)(x'i' - z_{ml}k)/r^2 \right\} \cdot \alpha_l \\ &= (2m_l/r^2)(x'i' - z_{ml}k) \\ &\quad \cdot (\cos I \sin \beta i' + \sin I k) \\ &= (2m_l/r^2)(x' \cos I \sin \beta - z_{ml} \sin I) \end{aligned}$$

The field components are found from this (noting that H is along the x' axis so that the component along the x axis is $H \sin \beta$ – see Eq. (3.41c))

$$\begin{aligned} Z &= -\partial A / \partial z \\ &= (2m_l/r^4) \\ &\quad \times \left\{ (z_{ml}^2 - x'^2) \sin I - 2x' z_{ml} \cos I \sin \beta \right\} \end{aligned} \quad (3.41a)$$

$$\begin{aligned} H &= -\partial A / \partial x' \\ &= (2m_l/r^4) \\ &\quad \times \left\{ (x'^2 - z_{ml}^2) \cos I \sin \beta - 2x' z_{ml} \sin I \right\} \end{aligned} \quad (3.41b)$$

$$\begin{aligned} F &= (H \sin \beta) \cos I + Z \sin I \\ &= (2m_l/r^4) \\ &\quad \times \left\{ (x'^2 - z_{ml}^2) (\cos^2 I \sin^2 \beta - \sin^2 I) \right. \\ &\quad \left. - 4x' z_{ml} \sin I \cos I \sin \beta \right\} \end{aligned} \quad (3.41c)$$

Two principal profiles for the vertical component are shown in Figure 3.17a, one where the dipole line strikes E-W ($\beta = \pi/2$) and one for a strike N30°W ($\beta = \pi/6$). When the dipole line is in the magnetic meridian, $\beta = 0$, the curve is symmetrical with Z_{max}

directly above the center. As in the case of the dipole, the depth to the center of the dipole line is approximately equal to the width of the profile at $Z_{max}/2$.

Figure 3.17b displays total-field principal profiles for a line of dipoles striking NW (or NE) for inclinations $I = 90^\circ, 60^\circ, 30^\circ, 0^\circ$. When $0^\circ \leq I \leq 15^\circ$ and $45^\circ \leq I \leq 90^\circ$, the full width of $F_{max}/2$ is roughly the depth, whereas for $15^\circ \leq I \leq 45^\circ$, the depth is approximately the distance between F_{max} and F_{min} . These profiles are also more diagnostic of dip than Z measurements are.

3.6.5. Dipping Dike (Prism)

(a) *General case*. Magnetic anomalies caused by intrusions, flows, or iron-rich sedimentary horizons are common features in regions favorable for mineral exploration, and there is frequently a contrast in the magnetic mineral content of such features with respect to the host rock. Such features may often be simulated by a two-dimensional dipping dike (prism). A vertical dike is also commonly used in making basement depth determinations in oil prospecting.

Direct application of Poisson's relation is difficult, so we proceed as follows. We assume a dike with dip ξ and strike β , and we take the y' axis along the strike direction. We assume that magnetic polarization is in the F_e direction, that is, $M = kF_e$. The geometry is illustrated in Figure 3.18a, from which we have the following relations:

$$\begin{aligned} r_1^2 &= d^2 + (x + d \cot \xi)^2 \\ r_2^2 &= D^2 + (x + D \cot \xi)^2 \\ r_3^2 &= d^2 + (x + d \cot \xi - b)^2 \\ r_4^2 &= D^2 + (x + D \cot \xi - b)^2 \\ \phi_1 &= \tan^{-1} \left\{ d/(x + d \cot \xi) \right\} \end{aligned}$$

and so on. Starting with Equation (3.26), we have

$$A = (M/\gamma\rho) g_f = -(M/\gamma\rho) \nabla U \cdot f_1 \quad (3.42)$$

where $f_1 = (\cos I \sin \beta i' + \sin I k)$. Using Equation (3.27a) this becomes

$$\begin{aligned} \mathbf{F} &= -\nabla A = (M/\gamma\rho) \nabla(\nabla U \cdot f_1) \\ &= (M/\gamma\rho) \nabla(U_x \cos I \sin \beta + U_z \sin I) \\ &= (kF_e/\gamma\rho) \left\{ (U_{xx} \cos I \sin \beta + U_{xz} \sin I)i' \right. \\ &\quad \left. + (U_{xz} \cos I \sin \beta + U_{zz} \sin I)k \right\} \end{aligned} \quad (3.43)$$

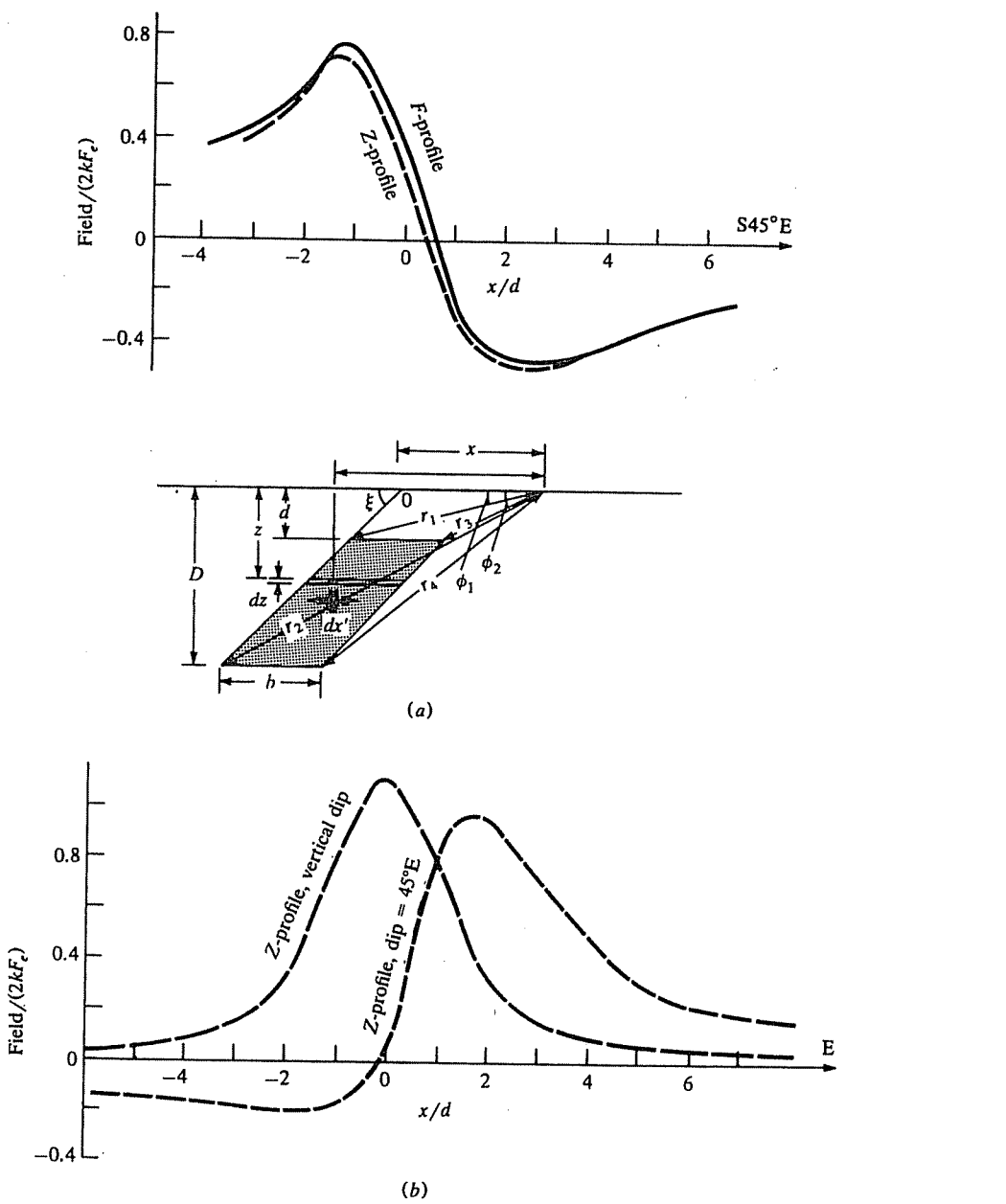


Figure 3.18. Profiles for dike model. $L = \infty$ except for (d). (a) F, Z profiles for $I = 60^\circ$, $\beta = 45^\circ$, $\xi = 45^\circ$, $b = 2d$, $D = 3.5d$. (b) Z profiles for $I = 75^\circ$, $\beta = 0^\circ$, $\xi = 45^\circ E$ and 90° , $b = 2d$, $D = \infty$.

Because U satisfies Laplace's equation (2.11a), $U_{xx} = -U_{zz}$. Differentiating Equation (2.9), we get

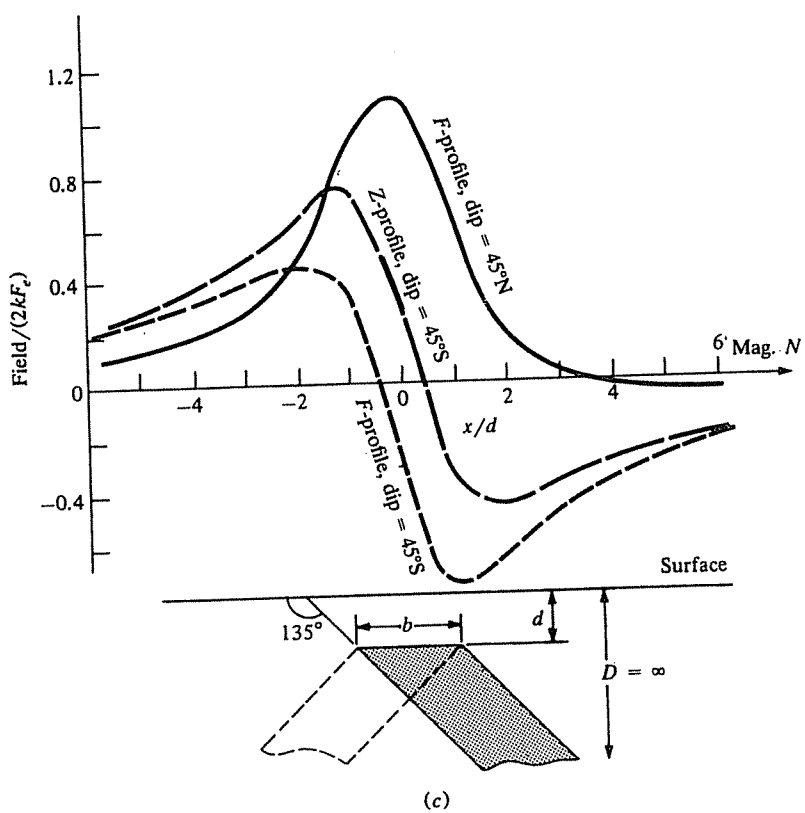
$$U_{xz} = 4\gamma\rho \int \int (xz/r^4) dx dz$$

$$U_{zz} = 2\gamma\rho \int \int \{(z^2 - x^2)/r^4\} dx dz$$

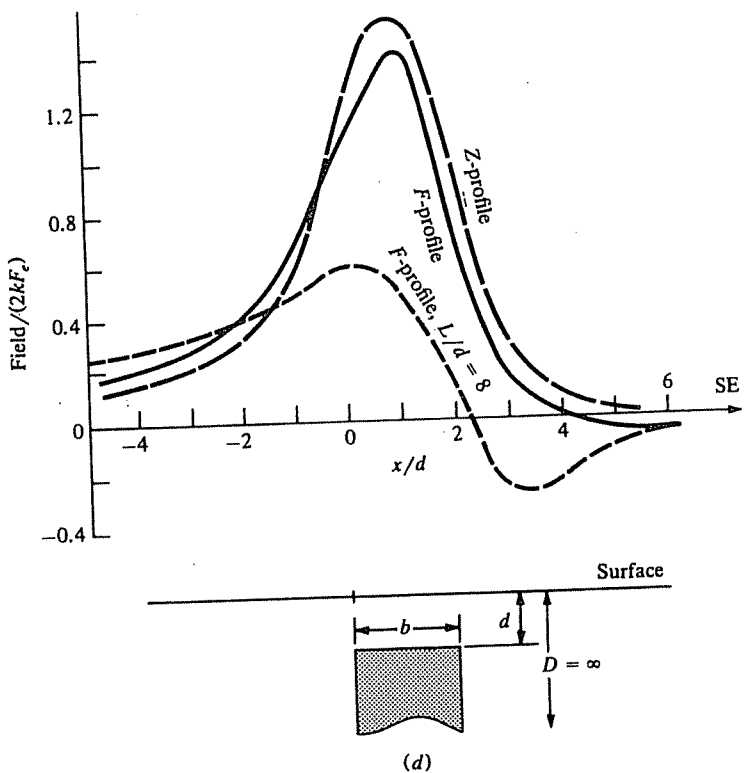
We change x and z to x' and z' , the coordinates of a point inside the dike. r^2 becomes $(x'^2 + z'^2)$.

Then,

$$\begin{aligned} U_{xz} &= 4\gamma\rho \int_{x'} \int_{z'} \frac{x'z'}{r^4} dx' dz' \\ &= 4\gamma\rho \int z' dz' \int \frac{x' dx'}{(z'^2 + x'^2)^2} \\ &= 4\gamma\rho \int z' dz' \left\{ \frac{-1}{2(z'^2 + x'^2)} \right\} \Big|_{x+z' \cot \xi - b}^{x+z' \cot \xi} \\ &= 2\gamma\rho \int_d^D \left\{ \frac{z'}{z'^2 \csc^2 \xi + 2z'x \cot \xi + x^2} \right. \\ &\quad \left. - \frac{z'}{z'^2 \csc^2 \xi + 2z'(x-b) \cot \xi + (x-b)^2} \right\} dz' \end{aligned}$$



(c)



(d)

Figure 3.18. (Continued) (c) F, Z profiles for $I = 60^\circ$, $\beta = 90^\circ$, $\xi = 45^\circ N$ and S , $b = 2d$, $D = \infty$. (d) F, Z profiles for $I = 75^\circ$, $\beta = 90^\circ$, $\xi = 90^\circ$, $b = 2d$, $D = \infty$, $2L = \infty$ and $16d$.

After some manipulation, this becomes

$$U_{xz} = 2\gamma\rho \sin \xi \{ \sin \xi \ln(r_2 r_3 / r_1 r_4) + \cos \xi (\phi_1 - \phi_2 - \phi_3 + \phi_4) \}$$

The value of U_{zz} can be found the same way; the result is

$$U_{zz} = .2\gamma\rho \sin \xi \{ \cos \xi \ln(r_2 r_3 / r_1 r_4) - \sin \xi (\phi_1 - \phi_2 - \phi_3 + \phi_4) \}$$

Substitution of the values of the derivatives in Equation (3.43) gives

$$\begin{aligned} Z = 2kF_e \sin \xi &\{ (\cos I \sin \xi \sin \beta \\ &+ \sin I \cos \xi) \ln(r_2 r_3 / r_4 r_1) \\ &+ (\cos I \cos \xi \sin \beta - \sin I \sin \xi) \\ &\times (\phi_1 - \phi_2 - \phi_3 + \phi_4) \} \end{aligned} \quad (3.44a)$$

$$\begin{aligned} H = 2kF_e \sin \xi \sin \beta & \times \{ (\sin I \sin \xi - \cos I \cos \xi \sin \beta) \ln(r_2 r_3 / r_4 r_1) \\ &+ (\cos I \sin \xi \sin \beta + \sin I \cos \xi) \\ &\times (\phi_1 - \phi_2 - \phi_3 + \phi_4) \} \end{aligned} \quad (3.44b)$$

$$\begin{aligned} F = 2kF_e \sin \xi & \left[\{ \sin 2I \sin \xi \sin \beta \right. \\ & - \cos \xi (\cos^2 I \sin^2 \beta - \sin^2 I) \} \\ & \times \ln(r_2 r_3 / r_4 r_1) \\ & \left. + \{ \sin 2I \cos \xi \sin \beta \right. \\ & + \sin \xi (\cos^2 I \sin^2 \beta - \sin^2 I) \} \\ & \times (\phi_1 - \phi_2 - \phi_3 + \phi_4) \] \end{aligned} \quad (3.44c)$$

The parameter values in these equations may sometimes be found from the interpretation of ground surveys, but generally this cannot be done for airborne work. Monopole- and dipole-line approximations (§3.6.4b, c) may occasionally be distinguished from dike-like models of considerable width in mineral exploration, but usually basement is so far removed from the aircraft in oil reconnaissance work that discrimination is impossible. The vertical dike is often used for basement depth determinations in the latter case.

(b) $E-W$ or $N-S$ strike. When the dike strikes $E-W$, $\beta = 90^\circ$ and Equations (3.44a, c) become

$$Z = 2kF_e \sin \xi \{ \sin(I + \xi) \ln(r_2 r_3 / r_4 r_1) + \cos(I + \xi) (\phi_1 - \phi_2 - \phi_3 + \phi_4) \} \quad (3.45a)$$

$$\begin{aligned} F = 2kF_e \sin \xi & \{ -\cos(\xi + 2I) \ln(r_2 r_3 / r_4 r_1) \\ & + \sin(\xi + 2I) \\ & \times (\phi_1 - \phi_2 - \phi_3 + \phi_4) \} \end{aligned} \quad (3.45b)$$

If, in addition, the dike has vertical sides, $\xi = 90^\circ$ and Equations (3.45) are simplified to

$$\begin{aligned} Z = 2kF_e & \{ \cos I \ln(r_2 r_3 / r_4 r_1) \\ & - \sin I (\phi_1 - \phi_2 - \phi_3 + \phi_4) \} \end{aligned} \quad (3.46a)$$

$$\begin{aligned} F = 2kF_e & \{ \sin 2I \ln(r_2 r_3 / r_4 r_1) \\ & + \cos 2I (\phi_1 - \phi_2 - \phi_3 + \phi_4) \} \end{aligned} \quad (3.46b)$$

For $N-S$ strike, $\beta = 0$, so

$$\begin{aligned} Z = 2kF_e \sin \xi \sin I & \{ \cos \xi \ln(r_2 r_3 / r_4 r_1) \\ & - \sin \xi (\phi_1 - \phi_2 - \phi_3 + \phi_4) \} \end{aligned} \quad (3.47a)$$

$$\begin{aligned} F = 2kF_e \sin \xi \sin^2 I & \{ (\cos \xi) \ln(r_2 r_3 / r_4 r_1) \\ & - \sin \xi (\phi_1 - \phi_2 - \phi_3 + \phi_4) \} \end{aligned} \quad (3.47b)$$

For a vertical dike with $N-S$ strike, Equations (3.47) become

$$Z = -2kF_e \sin I (\phi_1 - \phi_2 - \phi_3 + \phi_4) \quad (3.48a)$$

$$F = -2kF_e \sin^2 I (\phi_1 - \phi_2 - \phi_3 + \phi_4) \quad (3.48b)$$

(c) Dike of limited length. Dike anomalies rarely satisfy the criteria for two-dimensionality (strike length $\geq 10b$, where b is width). For a more realistic model (sometimes called a prism model) having a strike length $2L$, $D = \infty$, and $\xi = 90^\circ$, equation (3.44c) becomes

$$\begin{aligned} F = kF_e & \left\{ \sin 2I \sin \beta \left[\ln \left((r_1^2 + L^2)^{1/2} + L \right) \right. \right. \\ & - \ln \left((r_1^2 + L^2)^{1/2} - L \right) \\ & + \ln \left((r_3^2 + L^2)^{1/2} - L \right) \\ & \left. \left. - \ln \left((r_3^2 + L^2)^{1/2} + L \right) \right] \right. \\ & - (\cos^2 I \sin \beta - \sin^2 I) \\ & \times \left[\tan^{-1} \left(\frac{L}{x} \right) - \tan^{-1} \left(\frac{L}{x-b} \right) \right. \\ & \left. - \tan^{-1} \left\{ \frac{Ld}{x(r_1^2 + L^2)^{1/2}} \right\} \right. \\ & \left. + \tan^{-1} \left\{ \frac{Ld}{(x-b)(r_3^2 + L^2)^{1/2}} \right\} \right] \end{aligned} \quad (3.49)$$

(d) Discussion of principal profiles. Principal profiles are shown in Figure 3.18. In Figure 3.18a, the

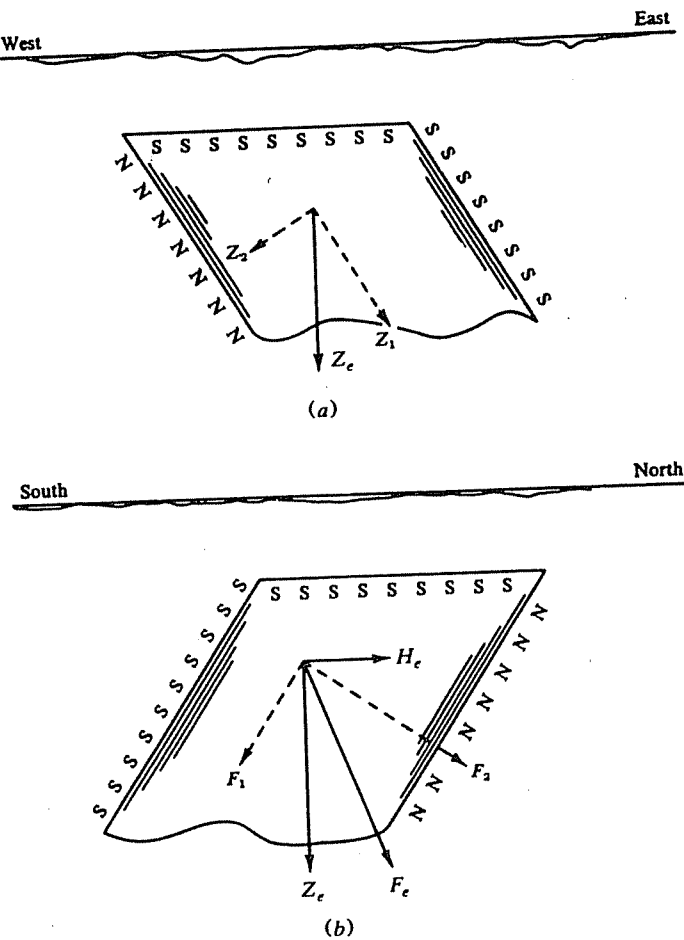


Figure 3.19. Pole distribution in a dike.

dike strikes NE-SW and dips 45° SE. In high magnetic latitudes where the H component is small, strike direction is relatively unimportant. This is clear from Equations (3.44a, c) where, if $I \approx 90^\circ$, the expressions for Z and F are practically independent of the strike direction β .

Figure 3.18b displays profiles for N-S strike. Figure 3.18c is for E-W strike. The asymmetry is less pronounced for north dips than for south dips. In high latitudes a dike with E-W strike and dip I gives a symmetrical Z profile and a nearly symmetrical F profile.

Figure 3.18d is for a vertical dike with NW or NE strike; Z and F profiles for $L = \infty$ are similar because the vertical component of F predominates. Gay (1967) takes advantage of these similarities and obtains a single family of curves for F , Z , and H over the whole range of dips and inclinations, defined by an index response parameter.

Figure 3.18d also shows the total field response over a short dike. The shape is similar to the other two curves but with lower amplitude. This profile is across the center of the dike and normal to the strike.

It is useful to provide a qualitative explanation for the character of the profiles in Figure 3.18 based on pole distribution where the magnetization is mainly induced by the Earth's field. For a dike dipping east and striking N-S as in Figure 3.19a, Z_e will produce N and S poles along the footwall and hanging wall, respectively, as can be seen by resolving Z_e into components parallel and normal to the dip. A similar explanation (Fig. 3.19b) accounts for the more pronounced asymmetry in the profile of the E-W dike dipping south in Figure 3.18c; the N poles on the footwall are produced by components of both H_e and Z_e . In fact, such a dike tends to be magnetized transversely because F_e is practically normal to the dip axis.

Depth estimates based on width of profiles are not particularly useful unless the profiles are symmetrical and the width is no greater than the depth to the top face. Under these restrictions the rule for half-width at half-maximum gives the depth to within 20%, that is, $x_{1/2} \approx d$ at $Z = Z_{\max}/2$. Several techniques based on profile slopes are effective for depth determination for the dike model (§3.7.11b). Direction of dip is usually fairly obvious from the profiles

since we know the total-field direction. The situation is complicated, however, because we cannot determine in advance the presence and direction of remanent magnetism and we have difficulty in determining the zero line for a field profile, that is, in isolating a single anomaly. A solution to finding the zero line for the dike model is given in Section 3.7.8.

The dike profiles in Figure 3.18b, c, and d were simplified by assuming infinite depth extent ($D = \infty$). They are not greatly changed for finite depth extent unless the depth extent is less than five times the width of the top face, in which case the positive tails are pulled down slightly. For very shallow dip, short strike length, and small depth extent (effectively a flat-lying plate magnetized transversely), the profiles becomes more symmetrical, with a broad maximum of small magnitude above the plate and negative tails at the flanks.

3.6.6. Dipping Sheet

The expressions for Z and F profiles over a thin sheet may be derived from Equation (3.44) by replacing the horizontal width b of the dipping dike model with $t \csc \xi$, where t is the thickness of the sheet. The principal reason for considering the thin sheet is that the expressions are simpler than for the dike and are sufficiently accurate provided the thickness t is not greater than the depth to the top d . The thin sheet geometry is also common in mineral exploration areas.

For the geometry shown in Figure 3.20a, the result is

$$\begin{aligned} Z = 2ktF_e & [(1/r_2) \{ \cos I \sin \beta \sin(\xi + \theta_2) \\ & + \sin I \cos(\xi + \theta_2) \} \\ & - (1/r_1) \{ \cos I \sin \beta \sin(\xi + \theta_1) \\ & + \sin I \cos(\xi + \theta_1) \}] \end{aligned} \quad (3.50a)$$

$$\begin{aligned} F = 2ktF_e & [(1/r_2) \{ \sin 2I \sin \beta \sin(\xi + \theta_2) \\ & - (\cos^2 I \sin^2 \beta - \sin^2 I) \\ & \times \cos(\xi + \theta_2) \} \\ & - (1/r_1) \{ \sin 2I \sin \beta \sin(\xi + \theta_1) \\ & - (\cos^2 I \sin^2 \beta - \sin^2 I) \\ & \times \cos(\xi + \theta_1) \}] \end{aligned} \quad (3.50b)$$

When the strike is E-W ($\beta = 90^\circ$), Equations (3.50) become

$$\begin{aligned} Z = 2ktF_e & \{ \sin(\xi + I + \theta_2)/r_2 \\ & - \sin(\xi + I + \theta_1)/r_1 \} \end{aligned} \quad (3.51a)$$

$$\begin{aligned} F = -2ktF_e & \{ \cos(\xi + 2I + \theta_2)/r_2 \\ & - \cos(\xi + 2I + \theta_1)/r_1 \} \end{aligned} \quad (3.51b)$$

and when the strike is N-S ($\beta = 0^\circ$),

$$Z = 2ktF_e \sin I \{ \cos(\xi + \theta_2)/r_2 - \cos(\xi + \theta_1)/r_1 \} \quad (3.52a)$$

$$\begin{aligned} F = 2ktF_e \sin^2 I & \{ \cos(\xi + \theta_2)/r_2 \\ & - \cos(\xi + \theta_1)/r_1 \} \end{aligned} \quad (3.52b)$$

If the sheet is vertical, $\xi = 90^\circ$ and Equations (3.50b), (3.51b), and (3.52b) simplify to

$$\begin{aligned} F = 2ktF_e & [(1/r_2) \{ \sin 2I \sin \beta \cos \theta_2 \\ & + (\cos^2 I \sin^2 \beta - \sin^2 I) \sin \theta_2 \} \\ & - (1/r_1) \{ \sin 2I \sin \beta \cos \theta_1 \\ & + (\cos^2 I \sin^2 \beta - \sin^2 I) \sin \theta_1 \}] \end{aligned} \quad (3.53a)$$

$$F = 2ktF_e \{ \sin(2I + \theta_2)/r_2 - \sin(2I + \theta_1)/r_1 \} \quad (3.53b)$$

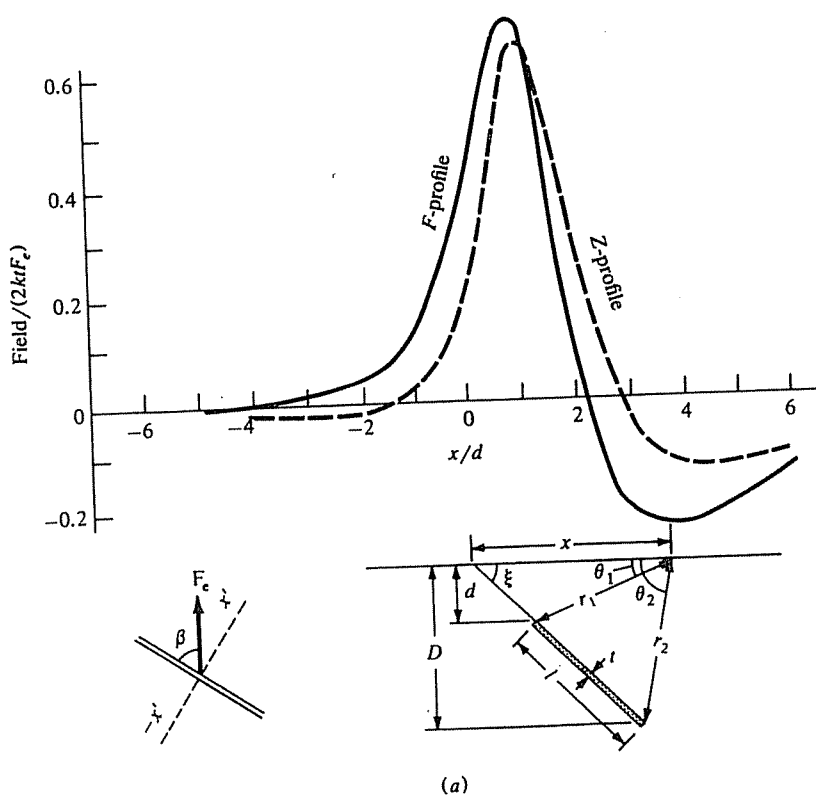
$$F = -2ktF_e \sin^2 I (\sin \theta_2/r_2 - \sin \theta_1/r_1) \quad (3.53c)$$

The profiles in Figure 3.20 for $I = 60^\circ$ are similar to, although sharper than, those for the dike. Rough dip estimates are possible when the strike of the body and total-field direction are known. Depth estimates from curve widths are fairly good when the curves are roughly symmetrical, but not practical when the sheet extends to great depth. The half-widths at $Z_{\max}/2$ for the short vertical and dipping models give $x_{1/2} \approx 1.7d$.

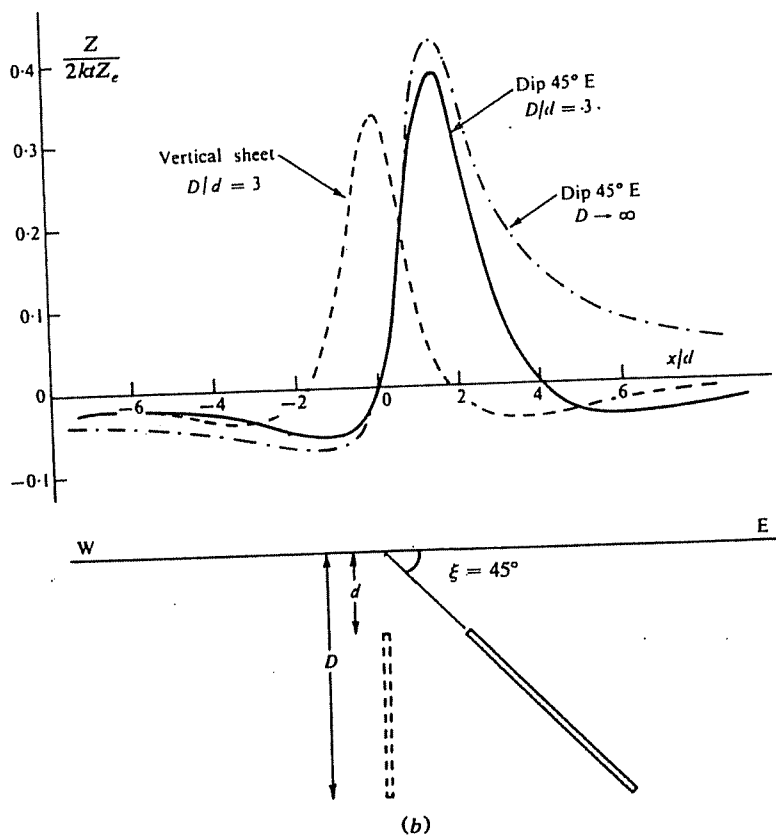
When the depth extent is very great, $r_2 \approx \infty$ and the sheet is effectively a half-plane. Then for Z and F we have from Equations (3.50),

$$\begin{aligned} Z = - & (2ktF_e/r_1) \{ \cos I \sin \beta \sin(\xi + \theta_1) \\ & + \sin I \cos(\xi + \theta_1) \} \end{aligned} \quad (3.54a)$$

$$\begin{aligned} F = - & (2ktF_e/r_1) \{ \sin 2I \sin \beta \sin(\xi + \theta_1) \\ & - (\cos^2 I \sin^2 \beta - \sin^2 I) \cos(\xi + \theta_1) \} \end{aligned} \quad (3.54b)$$

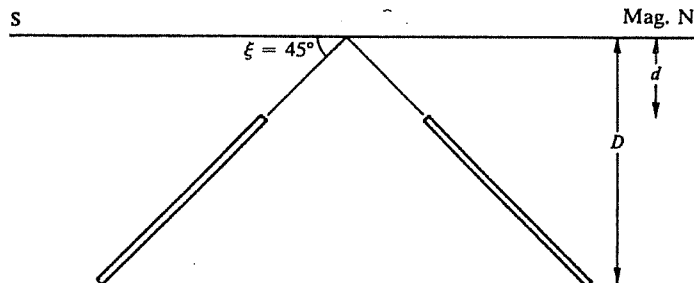
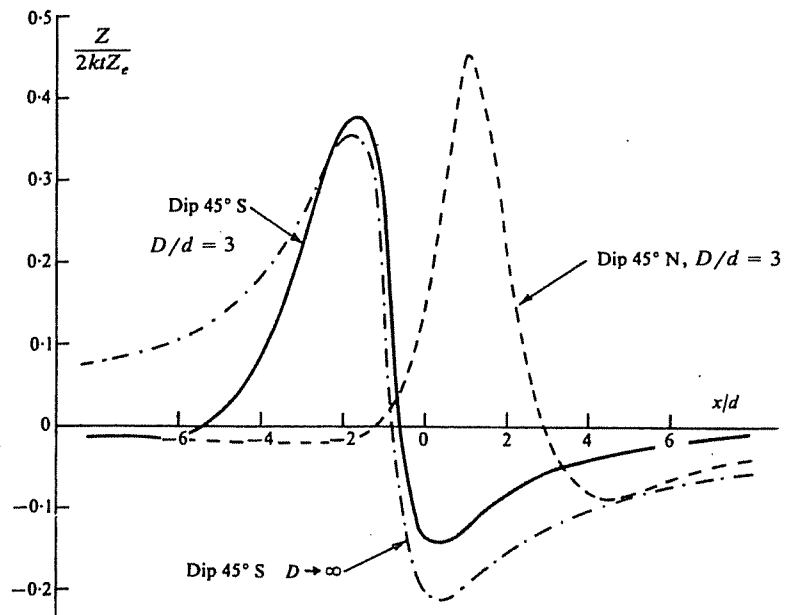


(a)



(b)

Figure 3.20. Thin sheet; $I = 60^\circ$, $D/d = 3$. (a) F , Z profiles for $\xi = 45^\circ$ NE, $\beta = 60^\circ$. (b) Z profiles for N-S strike ($\beta = 0^\circ$), $\xi = 45^\circ$ N and 90° , and effect of depth extent.



(c)

Figure 3.20. (Continued) (c) Z profiles for E-W strike, $\xi = 45^\circ\text{N}$ and 45°S , $\beta = 90^\circ$.

For this limiting case we can determine the depth and dip uniquely. Setting $dZ/dx = dF/dx = 0$, we obtain the x values for the maximum and minimum values for Z and F . This yields the following relations for Z :

$$\begin{aligned} x_m/d &= 2(\cos^2 I \sin^2 \beta + \sin^2 I)^{1/2} \\ &/(\cos I \sin \beta \sin \xi + \sin I \cos \xi) \quad (3.55a) \end{aligned}$$

$$\begin{aligned} x_{1/2}/d &= \{\cos^2 I \sin^2 \beta + \sin^2 I\}^{1/2} \\ &/(\cos I \sin \beta \cos \xi + \sin I \sin \xi) \quad (3.55b) \end{aligned}$$

where $x_m = x_{\max} - x_{\min}$ and $x_{1/2}$ is the full width at half-maximum. Likewise, writing $x'_m, x'_{1/2}$ for the

F curve, we have

$$\begin{aligned} x'_m/d &= 2 \left\{ \sin^2 2I \sin^2 \beta \right. \\ &\left. + (\sin^2 I - \cos^2 I \sin^2 \beta)^2 \right\}^{1/2} \\ &/ \left\{ \sin 2I \sin \beta \sin \xi \right. \\ &\left. + (\sin^2 I - \cos^2 I \sin^2 \beta) \cos \xi \right\} \quad (3.56a) \end{aligned}$$

$$\begin{aligned} x'_{1/2}/d &= \left\{ \sin^2 2I \sin^2 \beta \right. \\ &\left. + (\sin^2 I - \cos^2 I \sin^2 \beta)^2 \right\}^{1/2} \\ &/ \left\{ \sin 2I \sin \beta \cos \xi \right. \\ &\left. + (\sin^2 I - \cos^2 I \sin^2 \beta) \sin \xi \right\} \quad (3.56b) \end{aligned}$$

Combining Equations (3.55), we obtain the dip

angle ξ ,

$$\tan \xi = \frac{(-2x_{1/2} \cos I \sin \beta + x_m \sin I)}{(2x_{1/2} \sin I - x_m \cos I \sin \beta)} \quad (3.57a)$$

and the depth,

$$d = x_m x_{1/2} / (x_m^2 + 2x_{1/2}^2)^{1/2} \quad (3.57b)$$

When the sheet is not two dimensional, we can modify Equations (3.50) for a length $2L$. Then the principal profiles for Z and F become

$$Z = 2ktLF_e \{ (Q + R) \cos I \sin \beta + (S + T) \sin I \} \quad (3.58a)$$

$$F = 2ktLF_e \{ (Q + R) \sin 2I \sin \beta - (S + T) (\cos^2 I \sin^2 \beta - \sin^2 I) \} \quad (3.58b)$$

where

$$\left. \begin{aligned} Q &= \sin(\xi + \theta_2) / \{ r_2(r_2^2 + L^2)^{1/2} \} \\ &\quad - \sin(\xi + \theta_1) / \{ r_1(r_1^2 + L^2)^{1/2} \} \\ R &= \{ x \sin^2 \xi \cos \xi / (x^2 \sin^2 \xi + L^2) \} \\ &\quad \times \{ \cot(\xi - \theta_2) / (r_2^2 + L^2)^{1/2} \\ &\quad - \cot(\xi - \theta_1) / (r_1^2 + L^2)^{1/2} \} \\ S &= \cos(\xi + \theta_2) / \{ r_2(r_2^2 + L^2)^{1/2} \} \\ &\quad - \cos(\xi + \theta_1) / \{ r_1(r_1^2 + L^2)^{1/2} \} \\ T &= \{ x \cos^2 \xi \sin \xi / (x^2 \sin^2 \xi + L^2) \} \\ &\quad \times \{ \cot(\xi - \theta_2) / (r_2^2 + L^2)^{1/2} \\ &\quad - \cot(\xi - \theta_1) / (r_1^2 + L^2)^{1/2} \} \end{aligned} \right\} \quad (3.58c)$$

The profile is reduced in magnitude but otherwise unchanged in shape.

3.6.7. Horizontal Sheet (Plate)

When the sheet is horizontal (see Fig. 3.21a), $\xi = 0$, d becomes the depth of the sheet, and Equations (3.50) give

$$Z = -2ktF_e [(1/r_1)(\cos I \sin \beta \sin \theta_1 + \sin I \cos \theta_1) - (1/r_2)(\cos I \sin \beta \sin \theta_2 + \sin I \cos \theta_2)]$$

$$F = -2ktF_e [(1/r_1) \{ \sin 2I \sin \beta \sin \theta_1 - (\cos^2 I \sin^2 \beta - \sin^2 I) \cos \theta_1 \} - (1/r_2) \{ \sin 2I \sin \beta \sin \theta_2 - (\cos^2 I \sin^2 \beta - \sin^2 I) \cos \theta_2 \}]$$

where $r_1^2 = x^2 + d^2$, $r_2^2 = (x - l)^2 + d^2$, $\sin \theta_1 =$

d/r_1 , $\cos \theta_1 = x/r_1$, $\sin \theta_2 = d/r_2$, and $\cos \theta_2 = (x - l)/r_2$. Eliminating θ_1 and θ_2 , we get

$$\begin{aligned} Z &= -2ktF_e [(1/r_1)^2 (d \cos I \sin \beta + x \sin I) \\ &\quad - (1/r_2)^2 \{ d \cos I \sin \beta + (x - l) \sin I \}] \end{aligned} \quad (3.59a)$$

$$\begin{aligned} F &= -2ktF_e [(1/r_1)^2 \{ d \sin 2I \sin \beta \\ &\quad - x(\cos^2 I \sin^2 \beta - \sin^2 I) \} \\ &\quad - (1/r_2)^2 \{ d \sin 2I \sin \beta - (x - l) \\ &\quad \times (\cos^2 I \sin^2 \beta - \sin^2 I) \}] \end{aligned} \quad (3.59b)$$

Figure 3.21 shows profiles for horizontal plates. In Figure 3.21a, a shallow plate striking north-south produces a symmetrical Z profile. The F profile (not shown) is the same as the Z profile but reduced in magnitude by the multiplier $\sin I$. It is not possible to make good depth estimates from the width of these curves, but other techniques are available (see §3.7.8 and §3.7.11).

Over a horizontal thin sheet of finite strike length $2L$, Equation (3.59b) becomes

$$\begin{aligned} F &= -2ktF_e \{ \{ d \sin 2I \sin \beta \\ &\quad - x(\cos^2 I \sin^2 \beta - \sin^2 I) \} \\ &\quad / r_1 (1 + r_1^2/L^2)^{1/2} \\ &\quad - \{ d \sin 2I \sin \beta - (x - l) \\ &\quad \times (\cos^2 I \sin^2 \beta - \sin^2 I) \} \\ &\quad / r_2 (1 + r_2^2/L^2)^{1/2} \} \end{aligned} \quad (3.60)$$

Total-field profiles for the thin plate, illustrated in Figure 3.21b for infinite strike length and for $2L = 4l$, are remarkably similar. (This is also true for gravity profiles over a thin plate.) Unless $L < l$, the finite length does not affect the curve more than 20%.

Use of both the bottomless dike and the thin sheet models yields minimum and maximum depths, respectively, for d . Sharpness of the peak is characteristic of a shallow plate compared with the dike.

3.6.8. Semiinfinite Horizontal Sheet: Fault Approximation

If r_2 (or r_1) approaches infinity, l becomes very large and Equations (3.59) reduce to one term for a semi-infinite sheet. Profiles for vertical component and total field are illustrated in Figure 3.22. In Figure 3.22a, the strike is N-S with $I = 60^\circ$; both curves

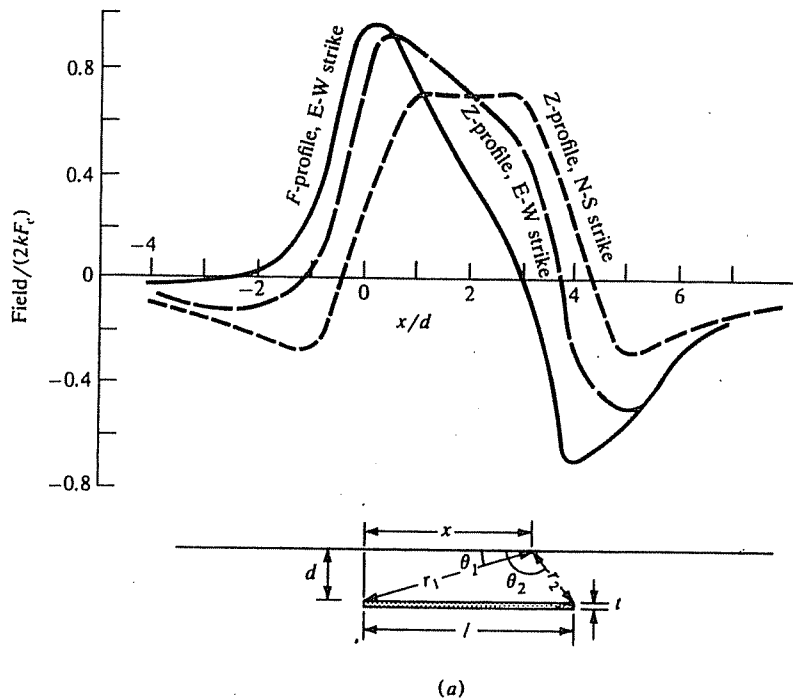


Figure 3.21. Thin horizontal plate of finite width, $t/l = 0.125$. (a) Profiles for $I = 60^\circ$, $\beta = 0^\circ$ and 90° , $d/l = 0.25$.

are antisymmetrical. The response in Figure 3.22b is similar to those from targets with steep dip. Both E-W profiles provide good depth estimates; d equals half the horizontal distance between Z_{\max} and Z_{\min} (or F_{\max} and F_{\min}). This measurement is 25% too large for the N-S profile (Fig. 3.22a).

It is necessary to traverse a considerable distance before the magnetic background is reached. For example, when $d = 30$ m, the survey should extend at least 800 m either way from the edge of the sheet. In practical situations this often cannot be done because there are likely to be other magnetic features in the vicinity.

If we introduce another semiinfinite sheet at a different depth, as shown in Figure 3.23, we have an approximation to a fault. When the fault plane has dip ξ , Equations (3.59) give

$$\begin{aligned} Z &= -2ktF_e \left[\left(1/r_1^2 \right) \{ d \cos I \sin \beta \right. \\ &\quad \left. + (x + d \cot \xi) \sin I \} \right. \\ &\quad \left. - \left(1/r_2^2 \right) \{ D \cos I \sin \beta \right. \\ &\quad \left. + (x + D \cot \xi) \sin I \} \right] \end{aligned} \quad (3.61a)$$

$$\begin{aligned} F &= -2ktF_e \left[\left(1/r_1^2 \right) \{ d \sin 2I \sin \beta \right. \\ &\quad \left. - (x + d \cot \xi) (\cos^2 I \sin^2 \beta - \sin^2 I) \} \right. \\ &\quad \left. - \left(1/r_2^2 \right) \{ D \sin 2I \sin \beta \right. \\ &\quad \left. - (x + D \cot \xi) (\cos^2 I \sin^2 \beta - \sin^2 I) \} \right] \end{aligned} \quad (3.61b)$$

where

$$r_1^2 = d^2 + (x + d \cot \xi)^2$$

$$r_2^2 = D^2 + (x + D \cot \xi)^2$$

For a vertical fault, Z and F profiles are shown in Figure 3.23a. Responses from normal faults are similar to these examples regardless of strike, but a profile over a reverse fault reflects the concentration of anomalous material in the area of overlap and resembles the response of a steeply dipping target. An estimate of the depth to the upper bed can be made in terms of $x_{1/2}$, half the distance between Z_{\max} and Z_{\min} : $0.5 \leq x_{1/2}/d \leq 1.25$. The lower limit applies when the lower bed is only slightly displaced; the upper limit applies when D/d is large. When the fault-plane dip ξ is fairly steep, $\xi \approx 90^\circ$ and D can be estimated from

$$\begin{aligned} D &\approx x_{1/2} \left[Z_m \left(1 + x_{1/2}^2/d^2 \right) \right. \\ &\quad \left. / \left\{ 2x_{1/2} (dZ/dx)_{\max} \right. \right. \\ &\quad \left. \left. - Z_m \left(1 + x_{1/2}^2/d^2 \right) \right\} \right], \end{aligned} \quad (3.62)$$

where $Z_m = Z_{\max} - Z_{\min}$ and $(dZ/dx)_{\max}$ is the maximum slope.

The fault approximation in Equations (3.61) is accurate to within a few percent provided d is larger

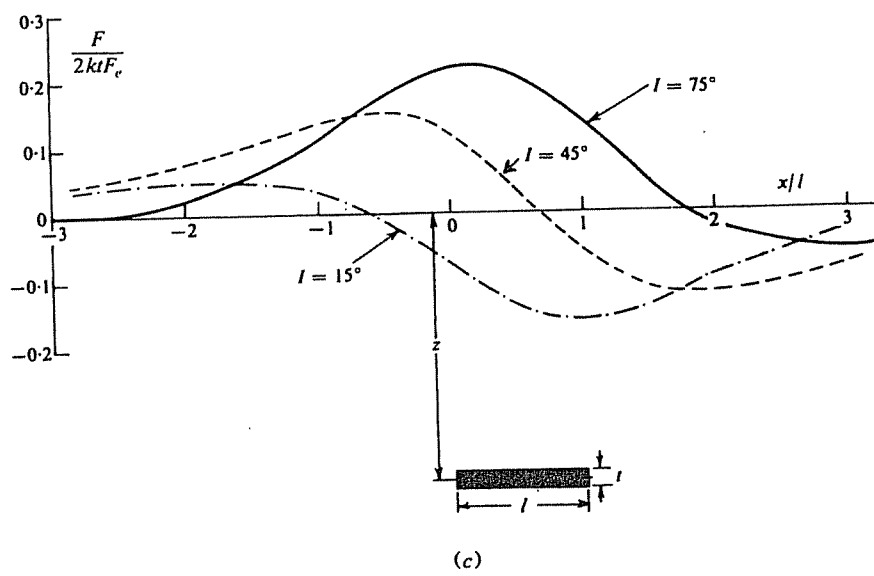
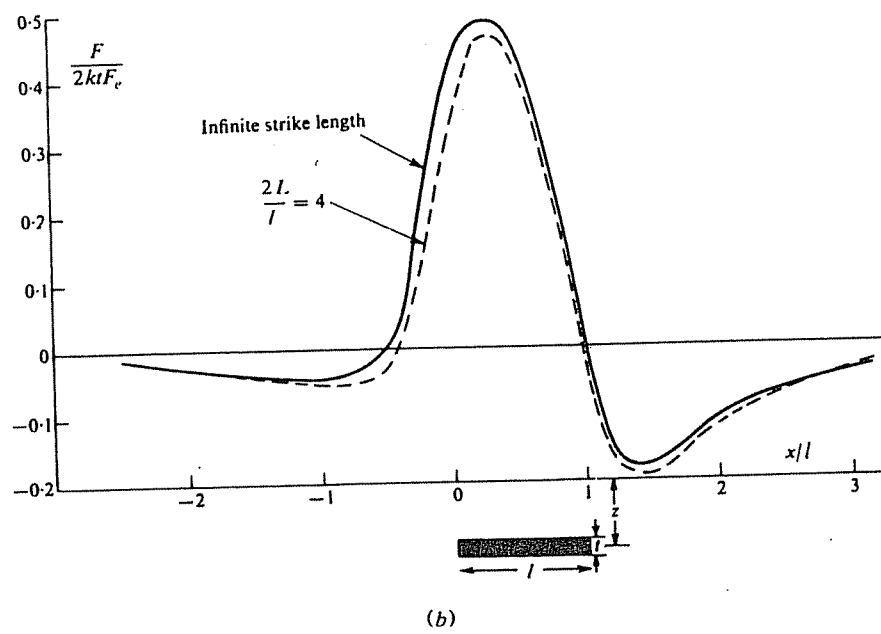


Figure 3.21. (Continued) (b) Profiles for $I = 75^\circ$, $\beta = 45^\circ$, $d/l = 0.5$. (c) Profiles for $I = 15^\circ$, $\beta = 45^\circ$, $d/l = 2$.

than $2t$. When this assumption is not valid, it is necessary to use the dike model (§3.6.5). With $r_3 = r_4 = \infty$ and $\phi_3 = \phi_4 = \pi$, the Z and F expressions for the horizontal slab are identical to Equations (3.44) to (3.48) with the terms in r_3 , r_4 , ϕ_3 , and ϕ_4 omitted (see Fig. 3.24). Figure 3.24 shows F profiles over a single horizontal bed with N-S strike and face angles of 45° and 135° . The curves are reflections of each other in both axes.

To simulate a fault, we add a similar slab at a different depth (as in Fig. 2.32), for example, for

E-W strike and strike length $2L$, we get

$$Z = 2kF_e \sin \xi [Q \ln(r_2 r_7 / r_1 r_8) + R(\phi_1 - \phi_2 - \phi_7 + \phi_8)] \quad (3.63a)$$

$$F = 2kF_e \sin \xi [S \ln(r_2 r_7 / r_1 r_8) + T(\phi_1 - \phi_2 - \phi_7 + \phi_8)] \quad (3.63b)$$

where Q , R , S , and T are as in Equations (3.58c). [Note that ξ in Eqs. (3.63) and in the factors Q , R , S , and T is the slope of the fault plane.]

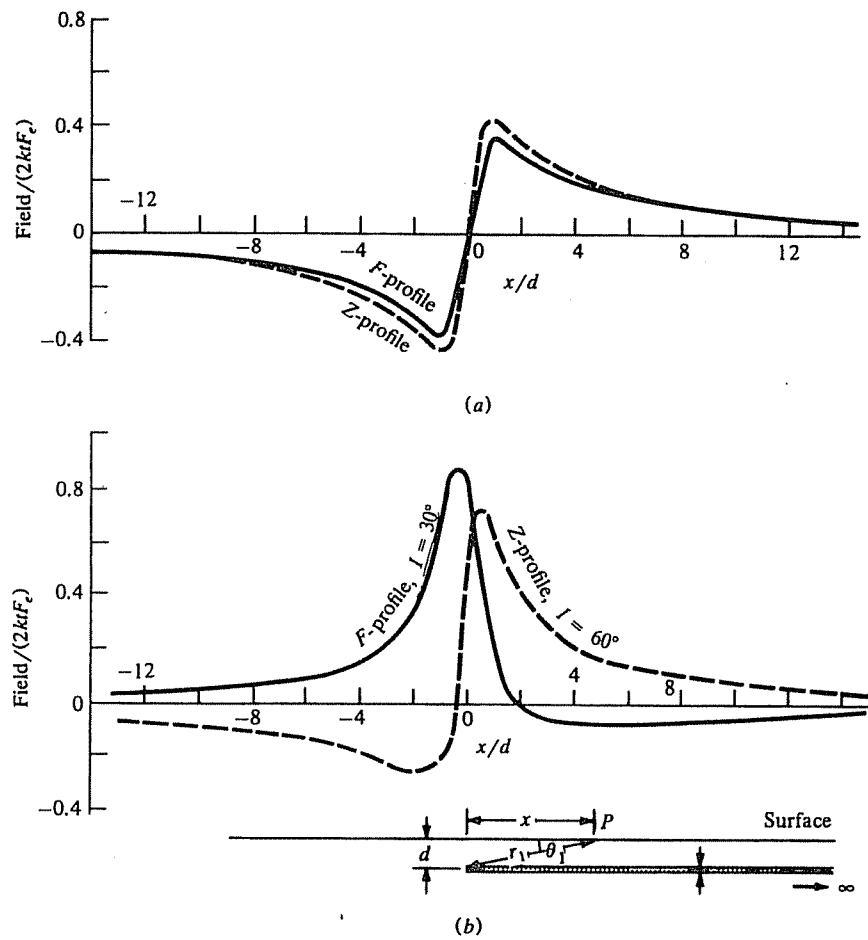


Figure 3.22. Semiinfinite horizontal sheet. F, Z profiles for (a) N-S strike, $I = 60^\circ$; (b) E-W strike, $I = 60$ and 30° .

3.6.9. Contact between Beds of Different Susceptibilities

A common magnetic structure results from the contact of two slabs with contrasting susceptibility values (see Fig. 3.25). Because a uniform continuous slab creates no magnetic anomaly, the effect of the contact is the same as that of the semiinfinite slab to the left with susceptibility $\Delta k = k' - k$. From Equation (3.44), we have

$$\begin{aligned} Z = 2 \Delta k F_e \sin \xi &\{ (\cos I \sin \xi \sin \beta \\ &+ \sin I \cos \xi) \ln(r_2/r_1) \\ &+ (\cos I \cos \xi \sin \beta \\ &- \sin I \sin \xi)(\phi_1 - \phi_2) \} \quad (3.64a) \end{aligned}$$

$$\begin{aligned} F = 2 \Delta k F_e &\left[\sin \xi \{ \sin 2I \sin \xi \sin \beta \right. \\ &- \cos \xi (\cos^2 I \sin^2 \beta - \sin^2 I) \} \ln(r_2/r_1) \\ &+ \{ \sin 2I \cos \xi \sin \beta \\ &+ \sin \xi (\cos^2 I \sin^2 \beta - \sin^2 I) \} (\phi_1 - \phi_2) \] \quad (3.64b) \end{aligned}$$

Figure 3.25 shows profiles over vertical and dipping contacts of considerable depth extent. When $\phi_2 = \pi/2$, Equation (3.64b) becomes, for a vertical contact striking N-S

$$\begin{aligned} F &= 2 \Delta k F_e \sin^2 I \{ \pi/2 - \tan^{-1}(d/x) \} \\ &= 2 \Delta k F_e \sin^2 I \tan^{-1}(x/d) \quad (3.65) \end{aligned}$$

The difference between the limiting value of F at $x = \pm \infty$ is

$$\Delta F = F_{\max} - F_{\min} = 2\pi \Delta k F_e \sin^2 I$$

The maximum slope occurs over the contact and is given by $(dF/dx)_{x=0} = 2 \Delta k F_e \sin^2 I / d$. We can calculate the susceptibility contrast and depth of the bed:

$$\Delta k = \Delta F \sin^2 I / 2\pi F_e \quad \text{and} \quad d = \Delta F / \pi (dF/dx)_{x=0} \quad (3.66)$$

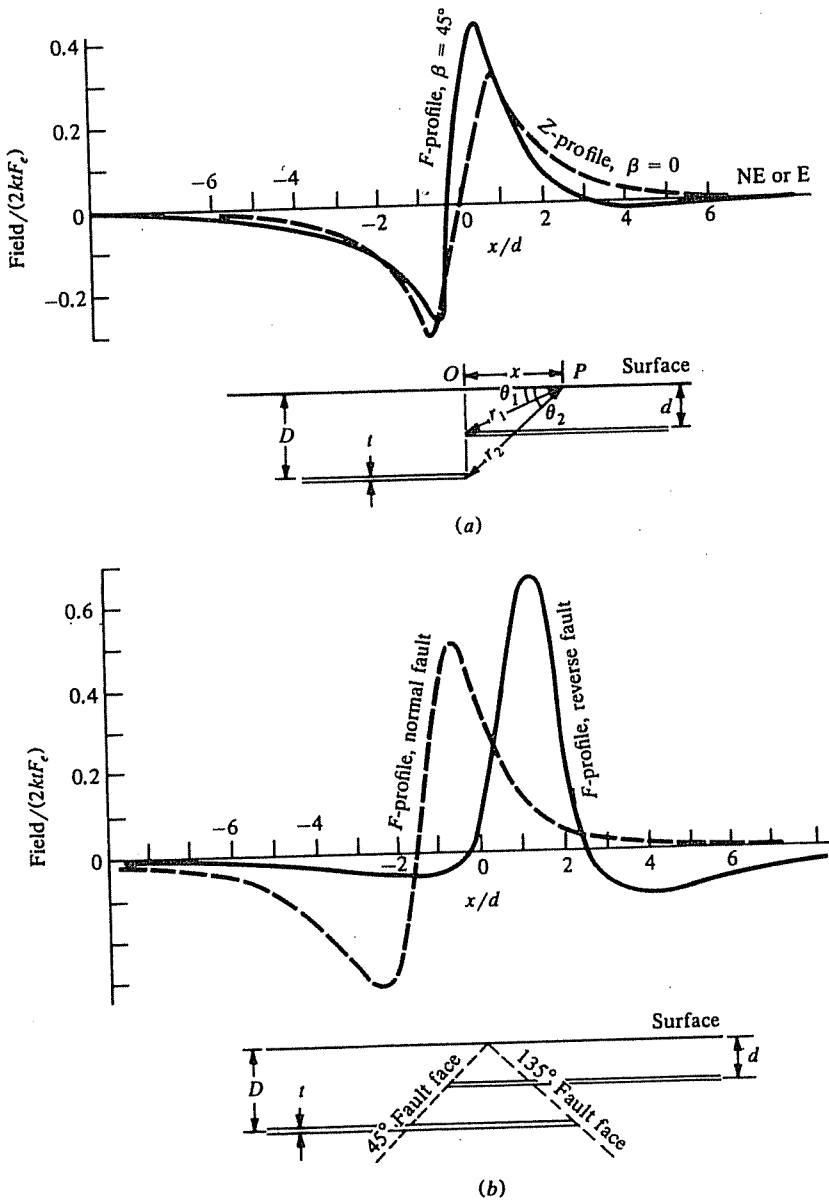


Figure 3.23. Thin-sheet fault approximation; $D = 2d$, $I = 60^\circ$. (a) F , Z profiles for vertical faults striking N-S and SE-NW ($\beta = 0^\circ, 45^\circ$). (b) F profiles for normal and reverse faults striking E-W; fault dip $45^\circ, 135^\circ$.

This calculation is not simple in practice because long traverses are required to locate F_{\max} and F_{\min} and they are usually obscured by other anomalies.

The curve in Figure 3.25a for E-W strike is similar to profiles over dikes dipping east (Figures 3.18b and 3.20b) and it would be difficult to recognize that it represents a steeply dipping contact. In Figure 3.25b, a contact with a slant face produces a curve that gives some indication of the model. One curve (broken line) also resembles a dipping sheet; the other resembles a dipping dike.

A gradiometer profile of dF/dx defines the location of a vertical contact better than either Z or F

profiles. The depth is equal to the separation of maximum and minimum values.

3.6.10. Demagnetization

In the preceding examples, we assumed that the induced magnetization is the product of k , the volume susceptibility of the body, and the external field F_e . In fact this is true only for rod-like shapes magnetized along the axis and having a cross section small in comparison to their length, such as the dipole of Equations (3.37). In general, the resultant field inside the body is different from F_e . This is

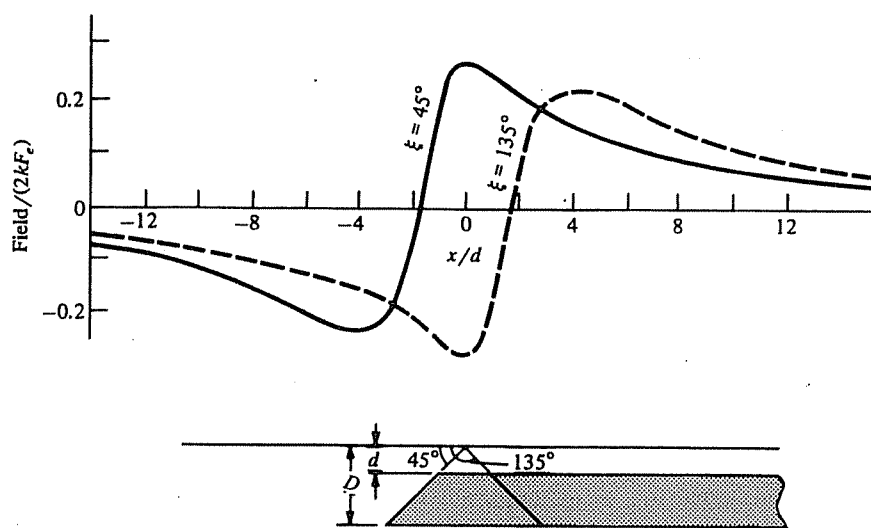
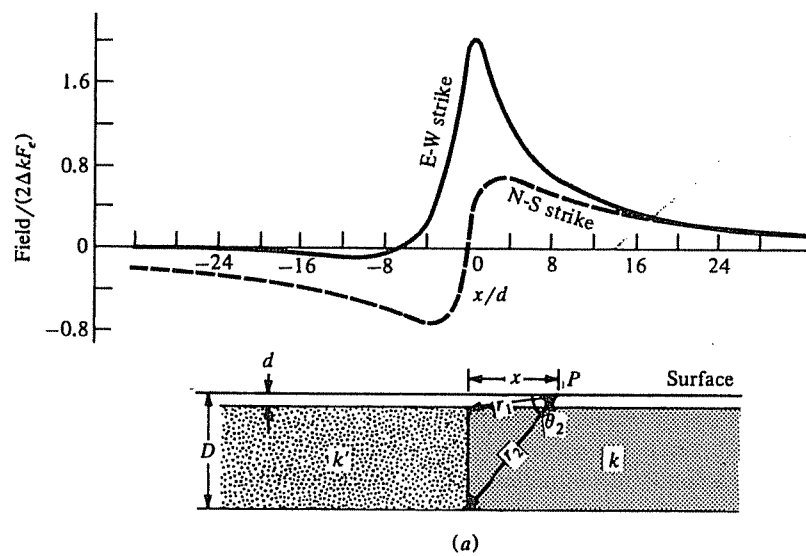
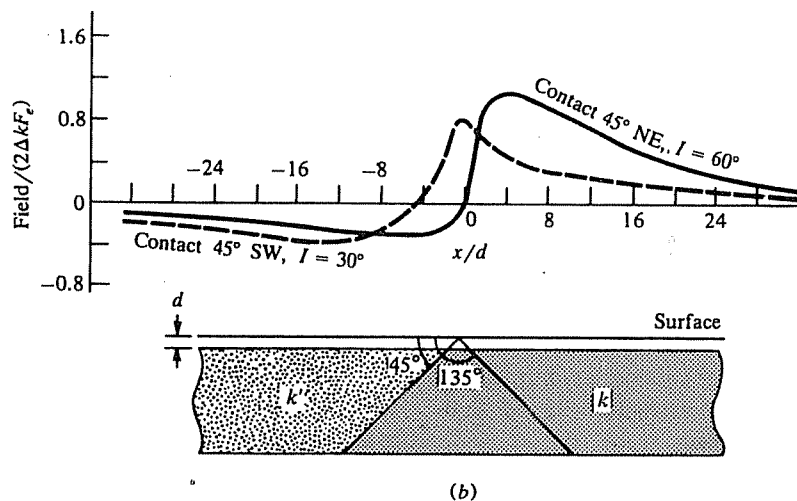


Figure 3.24. F profiles for a semiinfinite horizontal slab striking N-S, $I = 45^\circ$, dip of slab terminus 45 and 135° , $D = 3d$.



(a)



(b)

Figure 3.25. F profiles for contact between two horizontal slabs of different susceptibilities; $\Delta k = k - k'$, $D = 10d$. (a) Vertical contact ($\xi = 90^\circ$), $I = 60^\circ$, $\beta = 0$ and 90° . (b) Sloping contact ($\xi = 45^\circ$) for $I = 30$ and 60° , $\beta = 45^\circ$.

usually called *demagnetization*. The effect can be accommodated by replacing the susceptibility k by an *apparent susceptibility* k_a :

$$k_a = k/(1 + Nk) \quad 0 < N < 4\pi \quad (3.67)$$

Maximum demagnetization occurs in thin sheets magnetized normal to the face; in this case, $N = 4\pi$. For the sphere $N = 4\pi/3$. The effect is quite small unless $k \geq 0.1$ SI units. Demagnetization is significant only in massive pyrrhotite and in rocks containing $> 5\text{--}10\%$ magnetite. Sometimes an additional factor of $(1 - \cos^2 D \cos^2 \Delta I)$ is included to allow for the resultant magnetization being in a different direction from I ; ΔI is the difference in inclination and D is the declination.

3.7. PROCESSING AND INTERPRETATION

3.7.1. General

Magnetic survey results are displayed as a set of profiles or a magnetic contour map. In sedimentary areas there may be some similarity between magnetic and gravity maps, but in general magnetic anomalies are more numerous, more erratic, less persistent, and of larger magnitude than gravity anomalies. Consequently, regional-residual separation is much more complex. Considerable success has been achieved with bandpass, matching, and nonlinear filter operators. Downward continuation is not suitable in areas of complex shallow magnetics, characteristic of mineral exploration regions. It might be used for estimating the thickness of sediments in petroleum surveys, but it is not used much for this purpose. Instead, depths are determined by semiempirical depth rules or techniques like Werner deconvolution. Second-derivative analysis is useful in mineral prospecting to enhance small-scale features near the surface, whereas upward continuation may be used to suppress them. Upward continuation may also be used to reduce topographic effects in ground magnetic work. Equation (3.33) is a crude form of upward continuation.

Aeromagnetic data are often treated as follows:

1. Reduction of data to a uniform grid by one-dimensional interpolation perpendicular to flight direction.
2. Preprocessing, which might involve continuation, calculation of derivatives, extraction of the vertical component, and so forth.
3. Summation of several profiles to attenuate background noise.
4. Filtering and setting a threshold to locate anomalous areas.

5. Analyzing the profiles for the locations and orientations of anomalies.
6. Interpolating profiles normal to strike and centered on anomalies, for more detailed analysis.
7. Comparing profiles with curves developed from models.

Comparing field measurements with the results expected for simple models, such as discussed in Section 3.6, is done to determine the location, depth, size, shape, attitude, and, possibly, the susceptibility of the magnetic bodies responsible for the anomalies. Although simplified both geometrically and with regard to magnetization, matching curves (*parametric analysis*) with model curves provides reasonably rapid analysis and may be sufficient, especially where data are poor and/or incomplete.

Considerable effort has been expended to develop workable inversion procedures for magnetics, and, in spite of the nonunique nature of the problem, several effective algorithms have been developed, to which numerous references in the literature attest (Bhattacharyya, 1964; Hartman, Teskey, and Friedberg, 1971; Al-Chalabi, 1971; McGrath and Hood, 1973; Barnett, 1976; Teskey, 1980). Werner deconvolution (§3.7.10) is one such algorithm. The conventional starting point for magnetic data inversion might be a least-squares fit, ridge regression (Leite and Leao, 1985), and so on, as in Section 2.7.9, but magnetic inversion is more complex than gravity inversion because there are more variables.

3.7.2. Crude Interpretation and Structural Aspects

Because of the erratic and complex character of magnetic maps, interpretation is often only qualitative. Indeed, interpretation is something of a fine art. An interpreter experienced in magnetics can usually see structure merely by looking at a magnetic map, much as one can visualize surface features from the contours of a topographic map. Frequently magnetic features are rather directly related to surface outcrops and a magnetic map may be a fair substitute for a surface geology map where surface features are obscured by alluvium. Often there is a connection between magnetism and topography, as well as with buried geologic structures, particularly in mineral exploration areas. A visual study of the magnetic maps can be fruitful for preliminary interpretation. In this regard, experience is essential. Remanent magnetization, however, can produce significant effects and lead to incorrect interpretation if overlooked.

In sedimentary regions, particularly where the basement depth exceeds 1,500 m, the magnetic con-

tours are normally smooth and variations are small, reflecting the basement rocks rather than near-surface features. The larger anomalies usually are caused by susceptibility variations rather than basement relief. Consequently, anomaly magnitude is not of much value in finding basement depth, and depth calculations are usually based upon anomaly shape measurements, especially sharpness.

Regions where igneous and metamorphic rocks predominate, like the Precambrian Canadian Shield and the Appalachians, usually exhibit complex magnetic variations. Deep features are frequently camouflaged by higher frequency magnetic effects originating nearer the surface. Techniques for separating deep and shallow anomalies are similar to those discussed for gravity features in Section 2.6.

Magnetic anomalies often lie in trends. From a study of aeromagnetic maps of primarily sedimentary areas in western and central North America and Venezuela, Affleck (1963) found that the dominant direction within single magnetic-tectonic provinces is usually NE-SW or NW-SE and the trend normally terminates at the province boundaries. Moderate to weak features trending E-W or N-S often are superimposed on these. These weaker trends frequently extend across province boundaries and are probably of more recent origin. A cursory study of the Canadian Appalachian region (the Maritime provinces and eastern Quebec south of the St. Lawrence) and northern Saskatchewan and Alberta appears to confirm the trends. Large-scale northeast trends are obvious on the east and west flanks of the Canadian Shield.

3.7.3. Data Processing Operations: The Fourier Transform

As with gravity and seismic data processing, mathematical operations, such as convolution and correlation, can accomplish filtering, residualizing, continuation, and so on. Operations can be performed in the spatial, or wavenumber, domain (often called the frequency domain because wavenumber is spatial frequency). Fourier transforms (§A.9) are particularly useful in magnetics for (i) resolution of specific anomalies by downward or upward continuation, (ii) changing the effective field inclination (reduction to the pole) or conversion of total-field data to vertical-component data, (iii) calculation of derivatives, (iv) general filtering – separating anomalies caused by sources of different size and depth, and (v) modeling (Bhattacharyya and Navolio 1976). For literature on transformations of potential field data, see Dean (1958), Bhattacharyya (1965, 1966), Gunn (1975), and Spector and Grant (1985).

We usually write relations using two-dimensional Fourier transforms $f(x, y) \leftrightarrow F(u, v)$ (Eq. (A.57)) in the form

$$f(x, y) = (1/2\pi)^2 \int \int F(u, v) e^{j2\pi(ux+vy)} du dv \quad (3.68a)$$

$$F(u, v) = \int \int f(x, y) e^{-j2\pi(ux+vy)} dx dy \quad (3.68b)$$

(x, y) are spatial coordinates and (u, v) are wave-number coordinates.

The important characteristic of transformations is that information is not lost in the process, and in many cases operations are easier to perform in the transform domain. For example, the output-input expression $g(x, y) \rightarrow f(x, y) * w(x, y)$ for convolution in the spatial domain is (§A.10)

$$g(x, y) = \int \int f(x - \alpha, y - \beta) w(\alpha, \beta) d\alpha d\beta \quad (3.69a)$$

where $w(\alpha, \beta)$ is the convolution operator (also called a *weighting function* or *filter*). In the wave-number domain, this becomes simple multiplication:

$$G(u, v) = F(u, v) W(u, v) \quad (3.69b)$$

The relations between sources and their potential fields may be considered convolution operations, and transforms can be used to determine source characteristics from field operations, as discussed in the following sections.

3.7.4. Derivatives

Derivatives tend to sharpen the edges of anomalies and enhance shallow features. First and second vertical derivative maps are the most common ones made. Derivative maps may be made by the same techniques used for gravity data (§2.6.5). The first vertical derivative is also measured in gradiometer surveys.

3.7.5. Continuation

Field continuation was discussed in Section 2.6.7 as it applies to gravity. Adapting Equation (2.48) to magnetics, we have, for upward continuation (where z is positive downward),

$$F(x', y', -h) = \frac{h}{2\pi} \int \int \frac{F(x, y, 0) dx dy}{\{(x - x')^2 + (y - y')^2 + h^2\}^{1/2}} \quad (3.70)$$

Table 3.2. Coefficients for upward continuation.

i	r_i	$K(r_i, 1)$	$K(r_i, 2)$	$K(r_i, 3)$	$K(r_i, 4)$	$K(r_i, 5)$
0	0	0.11193	0.04034	0.01961	0.01141	0.00742
1	1	0.32193	0.12988	0.06592	0.03908	0.02566
2	$\sqrt{2}$	0.06062	0.07588	0.05260	0.03566	0.02509
3	$\sqrt{5}$	0.15206	0.14559	0.10563	0.07450	0.05377
4	$\sqrt{8}$	0.05335	0.07651	0.07146	0.05841	0.04611
5	$\sqrt{13}$	0.06586	0.09902	0.10226	0.09173	0.07784
6	5	0.06650	0.11100	0.12921	0.12915	0.11986
7	$\sqrt{50}$	0.05635	0.10351	0.13635	0.15474	0.16159
8	$\sqrt{136}$	0.03855	0.07379	0.10322	0.12565	0.14106
9	$\sqrt{274}$	0.02273	0.04464	0.06500	0.08323	0.09897
10	25	0.03015	0.05998	0.08917	0.11744	0.14458

The left side is the total field at the point $P(x', y', -h)$ above the surface on which $F(x, y, 0)$ is known. The calculation procedure is to replace the integral with a weighted sum of values taken on a regular grid.

The empirical formula of Henderson (1960) gives the field at the elevation h above the surface in terms of values $F(r_i)$, the average value $\bar{F}(r_i)$ over a circle of radius r_i centered at the point $(x, y, 0)$:

$$F(x, y, -h) = \sum \bar{F}(r_i) K(r_i, -h) \quad (3.71)$$

where $K(r_i, -h)$ are weighting coefficients (listed in Table 3.2 for $h = 1$ to 5). These coefficients give the upward continued field within 2%.

Another solution for continuation (in either direction) is by means of a Maclaurin expansion [Eq. (A.40)]:

$$\begin{aligned} F(x, y, h) &= F(x, y, 0) + h \frac{\partial F(x, y, 0)}{\partial z} \\ &\quad + (h^2/2!) \frac{\partial^2 F(x, y, 0)}{\partial z^2} \\ &\quad + (h^3/3!) \frac{\partial^3 F(x, y, 0)}{\partial z^3} + \dots \end{aligned} \quad (3.72)$$

[compare with Eq. (3.33)]. For a first approximation, the first two terms involving F and $\partial F/\partial z$ are often sufficient, and the simultaneous measurement of total field and vertical gradient provides these values. The $\partial^2 F/\partial z^2$ term can be found from maps of F , as indicated in Section 2.6.5, and, if necessary, the $\partial^3 F/\partial z^3$ term can be found in a similar manner from maps of $\partial F/\partial z$.

The Fourier transform provides another technique for field continuation. The integrand in Equation (3.70) is the product of $F(x, y, 0)$ and $(h/2\pi)\{(x - x')^2 + (y - y')^2 + h^2\}^{-3/2}$. Using the symmetry theorem [Eq. (A.60)] and the convolution theorem [Eq. (A.67a)], we get

$$\begin{aligned} X(t)Y(t) &\leftrightarrow 2\pi x(-\omega) * y(-\omega) \\ &= 2\pi x(\omega) * y(\omega) \end{aligned}$$

Thus, applying this result and Equation (A.62), we obtain for the transform of Equation (3.70),

$$\mathcal{F}_n(u, v) = (-2\pi/uv) \mathcal{F}_0(u, v) * \mathcal{W}(u, v) \quad (3.73)$$

where $\mathcal{F}_h(u, v) \leftrightarrow F(x', y', -h)$, $\mathcal{F}_0(u, v) \leftrightarrow F(x, y, 0)$, and $\mathcal{W}(u, v) \leftrightarrow w(x, y) = (h/2\pi)(x^2 + y^2 + h^2)^{-3/2}$.

The continuation filter is

$$\begin{aligned} \mathcal{W}(u, v) &= (h/2\pi) \int \int (x^2 + y^2 + h^2)^{-3/2} \\ &\quad \times e^{-j2\pi(ux+vy)} dx dy \\ &= (h/2\pi) e^{-2\pi h(u^2 + v^2)^{3/2}} \end{aligned} \quad (3.74)$$

For upward continuation, we know $F_0(x, y, 0)$ and the unknown is $F_h(x, y, -h)$, whose transform is

$$\begin{aligned} \mathcal{F}_h(u, v) &= \mathcal{F}_0(u, v)(h/2\pi) \\ &\quad \times \exp\left\{-2\pi h(u^2 + v^2)^{1/2}\right\} \end{aligned} \quad (3.75)$$

Thus the calculation of $\mathcal{F}_h(u, v)$ is straightforward.

Hanson and Miyazaki (1984) use a continuation method that is effective where surface relief is large and rocks are highly magnetic. As in gravity, upward continuation smooths the data, whereas downward continuation emphasizes high frequencies.

3.7.6. Spectral Analysis

The Fourier transform expresses a magnetic field as an integral of sine and/or cosine waves, each defining a wave of amplitude $A(\kappa)$ and phase $\phi(\kappa)$, where $\kappa/2\pi = 1/\lambda$ is the wavenumber. Plotting $A(\kappa)$ gives the amplitude spectrum and $A^2(\kappa)$ gives the power spectrum.

The expression for the field of an anomalous body often can be written as the product of three functions in the wavenumber domain (their convolution in the spatial domain):

- (i) f_a , amplitude factor, which is equal to $(4\pi M)^2$, where M is the magnetic moment/unit volume.
- (ii) f_h , the depth factor, $\exp\{-2h(u^2 + v^2)^{1/2}\}$, where h is the pole depth.
- (iii) f_B , the field-orientation factor, $\{l \cos \beta + m \sin \beta\}^2 + n^2 = (lu + mv)^2/(u^2 + v^2) + n^2$, where β is the angle between the body's orientation and magnetic north and l , m , and n are the direction cosines of the field \mathbf{F}_e .

For bodies that are large compared to their depth, we require two additional factors:

- (iv) The size factor: for a rectangular prism, $(\sin ua \sin vb)/(ua vb)^2$, where $2a$ and $2b$ are the prism dimensions.
- (v) The polarization-orientation factor involving the direction cosines of the polarization vector.

We thus write the field of a point pole or dipole in terms of factors (i) to (iii) as

$$F(x, y, 0) = f_a(x, y) * f_h(x, y, h) * f_\beta(x, y) \quad (3.76a)$$

or, in the wavenumber domain,

$$\mathcal{F}(u, v, 0) = \mathcal{F}_a(u, v) \mathcal{F}_h(u, v, h) \mathcal{F}_\beta(u, v) \quad (3.76b)$$

The effect of any of these factors may be removed by deconvolving in the space domain or by dividing in the wavenumber domain.

Numerous other filter operations can be used to separate deep from shallow, large from small, and three-dimensional from two-dimensional effects. Gunn (1975) discusses a solution for the magnetized rectangular prism. Hahn, Kind, and Mishra (1976) estimate depth from Fourier spectra.

3.7.7. Reduction to the Pole

This operation changes the actual inclination to the vertical. It can be performed (Baranov, 1957; Spector and Grant, 1985) by convolving the magnetic field with a filter whose wavenumber response is the product of a polarization-orientation factor and the field-orientation factor in items (v) and (iii) of Section 3.7.6. This transformation simplifies total-field maps and is a relatively easy operation at high magnetic latitudes where $Z \approx F$, but becomes more difficult near the magnetic equator (Silva, 1986).

3.7.8. Use of Master Curves for Dikes of Great Depth Extent

It is often difficult to establish a background or datum level for magnetic measurements and to locate a dike with respect to the profile. Hence, matching field results with profiles obtained from simple shapes can be difficult. An analysis (Koulomzine, Lamontagne, and Nadeau, 1970) for prisms and dikes of infinite depth extent solves this problem with master (or characteristic) curves that give depth, dip, and width of a prism or dike.

We rewrite Equation (3.44a) making the width $2b$ instead of b (Fig. 3.18a) and shifting the origin to a

point above the midpoint of the top of the dike. If we assume infinite depth extent so that $r_2 = r_4 = \infty$, $\phi_2 = \phi_4$, we have

$$\begin{aligned} Z = 2kF_e \sin \xi &\{ (\cos I \sin \xi \sin \beta \\ &+ \sin I \cos \xi) \ln(r_3/r_1) \\ &+ (\cos I \cos \xi \sin \beta \\ &- \sin I \sin \xi)(\phi_1 - \phi_3) \} \end{aligned}$$

where $r_1^2 = d^2 + (x + b)^2$, $r_3^2 = d^2 + (x - b)^2$, $\phi_1 = \cot^{-1}(x + b)/d$, and $\phi_3 = \cot^{-1}(x - b)/d$. Dividing by d to obtain the dimensionless parameters $X = x/d$ and $B = b/d$, we obtain

$$\begin{aligned} Z = M &\{ \cot^{-1}(X + B) - \cot^{-1}(X - B) \} \\ &+ (N/2) \ln \left[\left\{ (X - B)^2 + 1 \right\} \right. \\ &\quad \left. / \left\{ (X + B)^2 + 1 \right\} \right] \quad (3.77) \end{aligned}$$

where

$$M = 2kF_e \sin \xi \{ (\cos I \sin \beta \cos \xi - \sin I \sin \xi) \}$$

and

$$N/2 = 2kF_e \sin \xi \{ (\cos I \sin \beta \sin \xi + \sin I \cos \xi) \}$$

The first term is the symmetric component S and the second term is the antisymmetric component A . Over the center of the dike, S has a maximum and $A = 0$.

If we chose two conjugate points X_1 and X_2 on the dike profile such that the sum of the Z values is equal to Z_0 , the value of Z at $X = 0$, that is,

$$Z_1 + Z_2 = Z_0 \quad (3.78)$$

Then, because

$$(S_1 + A_1) + (S_2 + A_2) = (S_0 + A_0) = S_0$$

we have

$$S_1 + S_2 = S_0 = Z_0 \quad A_1 + A_2 = 0 \quad (3.79)$$

For the antisymmetric component,

$$\begin{aligned} \ln \left[\left\{ (X_1 - B)^2 + 1 \right\} / \left\{ (X_1 + B)^2 + 1 \right\} \right] \\ + \ln \left[\left\{ (X_2 - B)^2 + 1 \right\} \right. \\ \left. / \left\{ (X_2 + B)^2 + 1 \right\} \right] = 0 \\ \{ (X_1 - B)^2 + 1 \} \{ (X_2 - B)^2 + 1 \} \\ = \{ (X_1 + B)^2 + 1 \} \{ (X_2 + B)^2 + 1 \} \end{aligned}$$

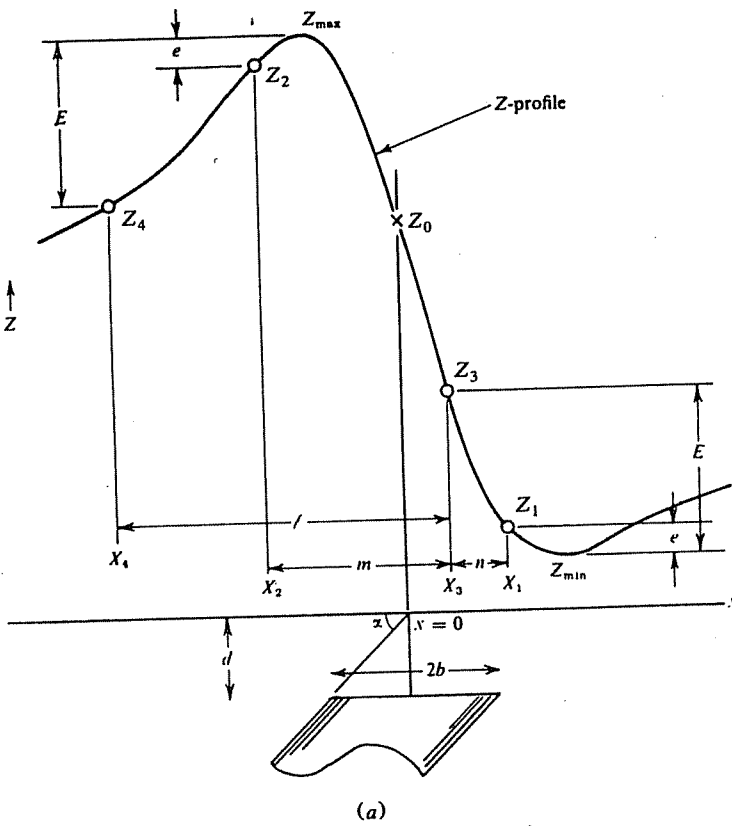


Figure 3.26. Two-dimensional dike of infinite depth extent. (a) Location of conjugate points and $X = 0$.

Solving for $X_1 X_2$, this gives

$$X_1 X_2 = -(1 + B^2) \quad (3.80)$$

Initially we do not know either the location of the dike center, $X = x = 0$, or the datum level $Z = 0$. Two pairs of conjugate points, X_1, X_2 and X_3, X_4 , are chosen such that Equation (3.78) is satisfied, and, in addition, $Z_{\max} - Z_2 = Z_1 - Z_{\min} = e$ and $Z_{\max} - Z_4 = Z_3 - Z_{\min} = E$ (Fig. 3.26a). Writing $l = X_3 - X_4$, $m = X_3 - X_2$, $n = X_1 - X_3$, and using the relation $X_1 X_2 = X_3 X_4$ [Eq. (3.74)], we find that

$$\left. \begin{aligned} X_1 &= n(n+l)/(l-m+n) \\ X_2 &= -m(l-m)/(l-m+n) \\ X_3 &= mn/(l-m+n) \\ X_4 &= (m-l)(n+l)/(l-m+n) \end{aligned} \right\} \quad (3.81)$$

We can now locate the point $X = 0$ and get Z_0 . For the best accuracy, X_3 and X_4 should be located close to the midpoint of the anomaly, and X_1 and X_2 near the maximum and minimum. $Z(0)$ is the point on the profile located a horizontal distance X_3 from Z_3 , X_2 from Z_2 , and so forth. Thus the datum line $Z = 0$ can be drawn at a distance above Z_{\min} equal to the vertical distance between Z_{\max} and Z_0 . This

follows from Equation (3.78) if we put $Z_1 = Z_{\max}$ and $Z_2 = Z_{\min}$, that is, $-Z_{\min} = Z_{\max} - Z_0$.

The analysis may now be carried further to establish the dike parameters. First, from the definitions of symmetric and antisymmetric functions,

$$\left. \begin{aligned} S(X) &= (1/2)\{Z(X) + Z(-X)\} \\ A(X) &= (1/2)\{Z(X) - Z(-X)\} \end{aligned} \right\} \quad (3.82)$$

we can plot $S(X)$ and $A(X)$ by taking points that are equidistant either side of $X = 0$. On these profiles we mark points $S_{3/4}$, $S_{1/2}$, and $A_{1/2}$ with corresponding abscissae $X_{3/4}$, $X_{1/2}$, and $X_{e/2}$; also X_e (Fig. 3.26b). By a development similar to that used for Equation (3.81), it can be shown that

$$\left. \begin{aligned} d &= x_{1/2}(\phi^2 - 1)/2 = 2x_{1/2}D \\ 2b &= x_{1/2}\{4 - (\phi^2 - 1)^2\}^{1/2} = 2x_{1/2}W \\ d &= x_e(1 - \mu)^2/2\mu = 2x_e\mathcal{D} \\ 2b &= x_e\{4\mu^2 - (1 - \mu)^4\}^{1/2}/\mu = 2x_e\mathcal{W} \end{aligned} \right\} \quad (3.83)$$

where $\phi = x_{1/2}/x_{3/4}$, $\mu = x_e/x_{e/2}$, $D = (\phi^2 - 1)/4$, $\mathcal{D} = (1 - \mu)^2/4\mu$, $W = \{4 - (\phi^2 - 1)^2\}^{1/2}/2$, $\mathcal{W} = (1/2\mu)\{4\mu^2 - (1 - \mu)^4\}^{1/2}$, $x_{1/2} = X_{1/2}d$, and so forth. Finally, we can find the dip angle ξ

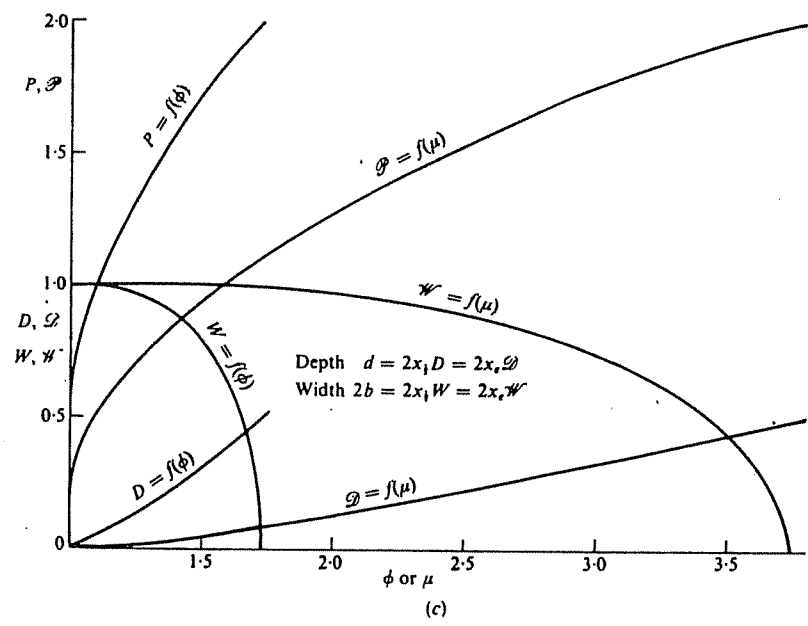
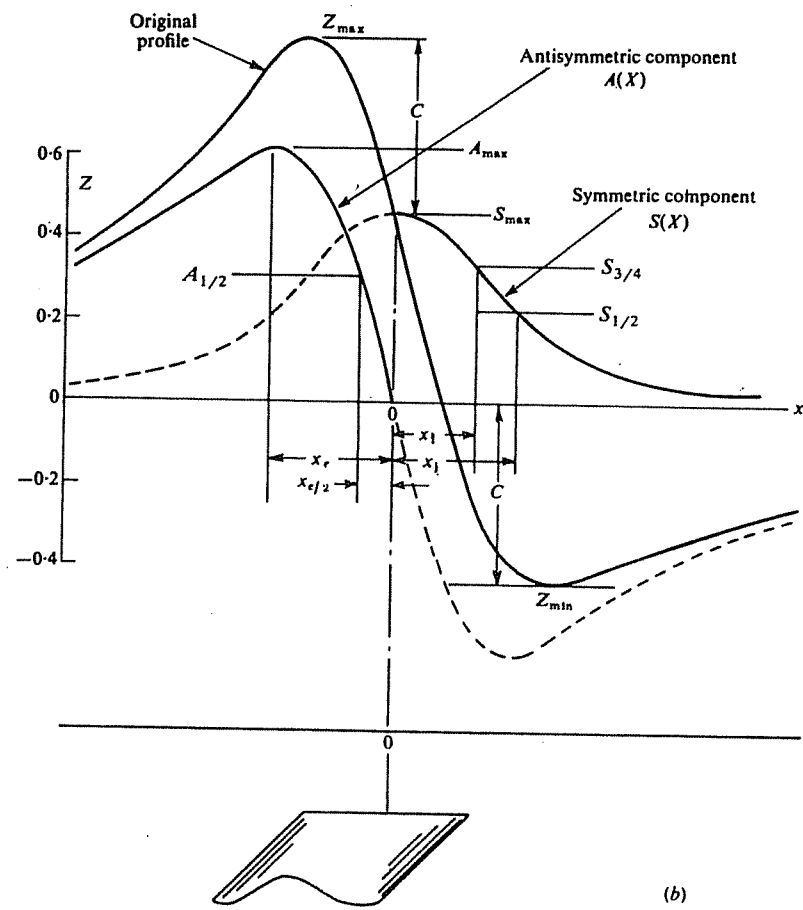


Figure 3.26. (Continued) (b) Symmetric and antisymmetric components. (c) Master curves.

from the relation

$$\xi = \pi - \cot^{-1} \left(\frac{H_e \sin \beta}{Z_e} \right) + \tan^{-1} \left\{ \frac{A(X)_{\max}}{S(X)_{\max}} \cdot \frac{\frac{4 \tan^{-1} B}{\ln \{(x_e - B)/(x_e + B)\}}}{\} } \right\} \quad (3.84a)$$

or

$$\xi = \pi - \cot^{-1} \left(\frac{H_e \sin \beta}{Z_e} \right) + \tan^{-1} \left\{ \frac{A(X)_{\max}}{S(X)_{\max}} \cdot \frac{\frac{4 \tan^{-1} B}{\ln \{(x_{1/2} - B)/(x_{1/2} + B)\}}}{\} } \right\}. \quad (3.84b)$$

Six master curves involving functions of d , b , and ξ for the symmetric and antisymmetric components of the dike profile are shown in Figure 3.26c. The dip-angle functions P and \mathcal{P} in Figure 3.26 are related to known quantities in the following expansions of Equation (3.84):

$$\begin{aligned} \xi &= \{ \pi - \cot^{-1}(H_e \sin \beta / Z_e) \} \\ &= \tan^{-1}(\mathcal{E}P) \text{ or } \tan^{-1}(\mathcal{E}\mathcal{P}), \end{aligned} \quad (3.85a)$$

where $\mathcal{E} = A(X)_{\max} / S(X)_{\max}$,

$$\begin{aligned} P &= \frac{4 \tan^{-1}(W/2D)}{\ln \{(1 - W)/(1 + W)\}} \\ \mathcal{P} &= \frac{4 \tan^{-1}(\mathcal{W}/2\mathcal{D})}{\ln \{(1 - \mathcal{W})/(1 + \mathcal{W})\}} \end{aligned} \quad (3.85b)$$

Because Equation (3.83) gives W , D , \mathcal{W} , and \mathcal{D} in terms of ϕ and μ , and these in turn can be found from the curves, P and \mathcal{P} are fully determined.

We can solve for the total-field anomaly in similar fashion. The analysis for the dike of infinite depth extent has been extended to cover a prism of finite length and depth extent. Because of the extra terms, it is necessary to provide more master curves, but the procedure is similar. Master curves for other models are also available (Grant and Martin, 1966; Martin, 1966; Gay, 1967). The second reference contains the following models, in addition to the prism: horizontal slab, plate, rod, and dipping sheet. (The method can be extended to dikes or prisms in gravity interpretation.)

3.7.9. Matched Filtering

Where the problem is locating a signal in a data set, matched filtering provides a powerful method if the

spectrum of the sought-for signal is known. A *matched filter* is a filter that has the same spectrum as the sought-for signal. One way to carry out matched filtering involves using the Hilbert transform (Sheriff and Geldart, 1983: §10.3.11) to separate the symmetric and antisymmetric anomaly components (§3.7.8). Both total-field and gradient data may be processed in this way (Naudy, 1971; Nabighian, 1984).

3.7.10. Werner Deconvolution

Werner (1953) proposed a method for isolating a magnetic anomaly from the interference produced by nearby anomalies. This led to automated procedures for interpreting magnetic data, now known as *Werner deconvolution* (Hartman, Teskey, and Friedberg, 1971; Jain, 1976; Kilty, 1983).

The magnetic anomaly for a dipping dike can be written in empirical form as

$$F(x) = \{ M(x - x_0) + Nz \} / \{ (x - x_0)^2 + z^2 \} \quad (3.86a)$$

where x_0 is the surface point directly above the center of the top of the dike, z is the depth to the top, x is the point of measurement, and the x axis is normal to the strike. M and N are unknown functions of the dike geometry and mineralization. Rearranging Equation (3.86a) in the form

$$x^2 F(x) = a_0 + a_1 x + b_0 F(x) + b_1 x F(x) \quad (3.86b)$$

where $a_0 = -Mx_0 + Nz$, $a_1 = M$, $b_0 = -x_0^2 - z^2$, and $b_1 = 2x_0$, we find that $x_0 = b_1/2$ and $z = (-4b_0 - b_1^2)^{1/2}/2$. Thus we can determine x_0 and z by measuring F at four stations and solving Equation (3.86b) for a_0 , a_1 , b_0 , and b_1 .

Extending the problem beyond an isolated anomaly. Werner assumed that the noise or interference caused by neighboring magnetic anomalies could be taken into account by extending the polynomial, so that the measured field \mathcal{F} becomes

$$\mathcal{F} = F(x) + c_0 + c_1 x + \cdots + c_n x^n \quad (3.87)$$

where $F(x)$ is given by Equation (3.86a) so that $(n + 5)$ unknown quantities are involved. Usually the polynomial is first or second order only, so that six or seven stations are sufficient for a solution.

The scope of this analysis has been enlarged to include models other than dikes: basement topography, magnetic interfaces (which use dF/dx rather

Table 3.3. Empirical depth estimation methods for magnetic anomalies.

Method	Half-width	Peak-to-Zero	Vertical grad.	Flank slope
Component measured	F, Z	F, Z, H	$F, \partial F / \partial z$, $Z, \partial Z / \partial z$	F, Z
<i>Model</i>				
Monopole	$1.3x_{1/2}$	$1.3x_{p0}$	$-2F / (\partial F / \partial z)$	
Dipole	$2x_{1/2}$	$1.3/x_{p0} \leq 2$	$-3F / (\partial F / \partial z)$	
Monopole line	$x_{1/2}$	x_{p0}	$-F / (\partial F / \partial z)$	
Dipole line	$2x_{1/2}$	x_{p0}	$-2F / (\partial F / \partial z)$	
General	$0.7 \leq x_{1/2} \leq 1.3$	x_{p0}	$-nF / (\partial F / \partial z)$	$0.5 \leq x_f \leq 1.5$

Note: $x_{1/2}$ is the full width at half-peak amplitude, x_{p0} is the horizontal distance from peak to zero-crossing, n is an empirically determined index factor, and x_f is the horizontal distance over which slope is straight line.

than F), faults, and contacts. This type of analysis is also suitable for gravity interpretation.

There are limitations to Werner deconvolution, such as resolution between neighboring bodies and lack of discrimination among parameters, leading to a relation between, say, dip angle and susceptibility. The data are sensitive to geological and measurement noise (signal/noise = 100 produces 20% scatter in depth and position estimates). However, the technique is attractive because of ease of access to the computer and consequent speed in handling large quantities of data.

3.7.11. Depth Estimates

(a) *Smith rules for maximum depth.* As in Section 2.7.12, which dealt with depth estimates for gravity anomalies, there are corresponding limiting values in magnetics derived by Smith (1961). If the magnetization M is parallel throughout a body, though not necessarily uniform or even in the same sense, and if $|M|_{\max}$, $|\partial Z / \partial x|_{\max}$, and $|\partial Z^2 / \partial x^2|_{\max}$ are absolute values of the maxima of M and the first and second derivatives of F or Z along the x profile, then the depth z_u to the upper surface is given by

$$\left. \begin{aligned} z_u &\leq 5|M|_{\max} / |\partial F / \partial x|_{\max} \\ z_u^2 &\leq 30|M|_{\max} / |\partial F^2 / \partial x^2|_{\max} \end{aligned} \right\} \quad (3.88a)$$

For Z profiles, where M is everywhere vertical and in the same direction (down or up), the numerical factors are reduced to 2.6 and 3.1, respectively.

For two-dimensional magnetic features having infinite length in the y direction, in which the total magnetization is parallel throughout, the equivalent expressions become

$$\left. \begin{aligned} z &\leq 4|M|_{\max} / |\partial F / \partial x|_{\max} \\ z^2 &\leq 5|M|_{\max} / |\partial F^2 / \partial x^2|_{\max} \end{aligned} \right\} \quad (3.88b)$$

Where the body is uniformly magnetized by induction, we may replace M_{\max} by kF_e or $kF_e/(1 + Nk)$ as in Equation (3.67).

Because we do not normally have a value of M_{\max} , estimates obtained by combining the two limits are even cruder than the equivalent relations for gravity. For a semiinfinite thin sheet, the result is within 50%, but it appears to be even poorer for three-dimensional features.

(b) *Empirical depth rules.* A number of rules-of-thumb for depth estimation have developed from practical experience in magnetic interpretation. These relate to profile shapes; for example, they often use horizontal widths at some fraction of the peak value for symmetrical curves and horizontal distances from peak-to-zero values for asymmetric curves. Peters (1949) was probably the first to relate depth to the horizontal extent of portions of sloping flanks, and variations of slope techniques are among the most popular. The vertical gradient is also used in such rules (Barongo, 1985). A summary of such rules is given in Table 3.3.

Slope methods are widely used, especially for aeromagnetic interpretation. Graphical techniques use the sloping flanks of profiles to estimate depth (Nettleton, 1971; Spector, 1979). In Figure 3.27a, S is the horizontal extent of the portion of the curve that is nearly linear at the maximum slope. Two additional line segments have been drawn tangent to the profile at half the maximum slope; the distance between the points of tangency is P . The depth of the source beneath these portions of the curve is given by

$$h = k_1 S \quad 1.67 \leq k_1 \leq 2.0$$

(generally $k_1 \approx 1.82$) (3.89a)

$$h = k_2 P \quad (\text{generally } k_2 \approx 0.63) \quad (3.89b)$$

The use of both methods provides a check on the

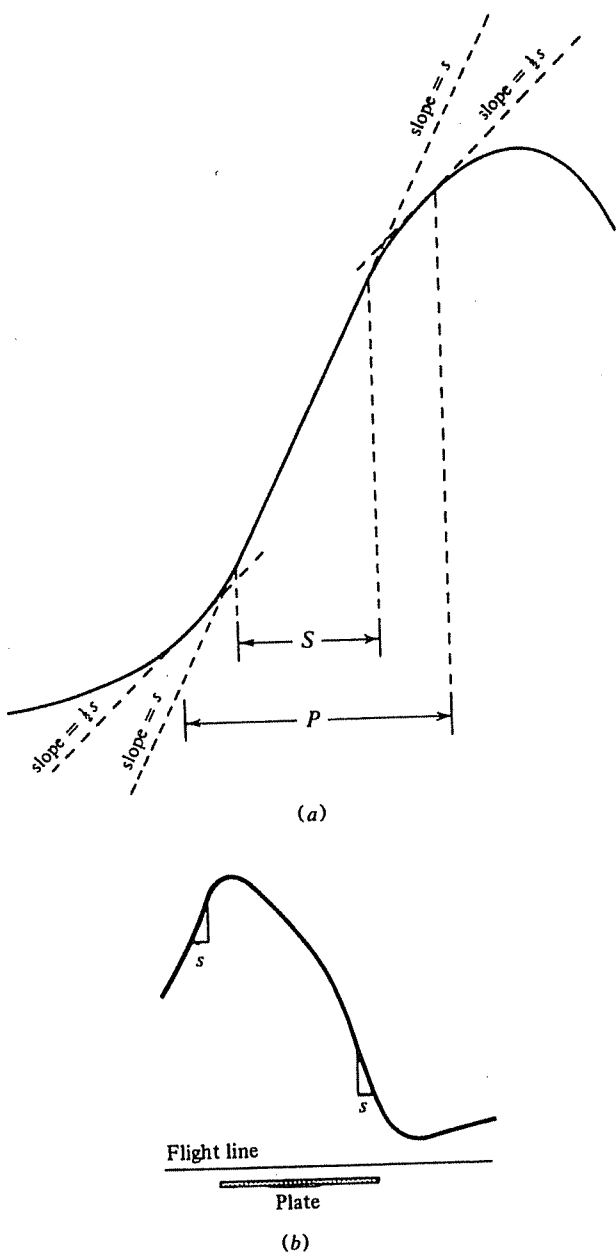


Figure 3.27. Determining anomaly depth from the slope of a magnetic profile. (a) Maximum-slope (S) and half-slope (P) measurements. (b) Maximum-slope measurements on a thin plate anomaly.

depth estimates and the care with which the graphical analysis is done. This method generally yields reasonable results for horizontal basement models with steeply dipping contacts; thus, it is suitable in the analysis of airborne data. It is much simpler and faster and provides more depth estimates than analysis by model curve fitting. It can be carried out on original field profiles and so need not wait on map preparation; it can also be applied to analysis of maps (Rao and Babu, 1984).

Use of slope techniques requires corrections. When flight lines are not normal to the local geological strike, horizontal distances are too large and

should be multiplied by a cosine factor. Correction also has to be made for the flight elevation to give values with respect to sea level (or to an arbitrary datum).

3.8. FIELD EXAMPLES

3.8.1. Ground Surveys

(1) The first example shows the inherent complexity of ground magnetic data and the difficulties in accurately interpreting them. Figure 3.28 displays magnetic contours and two vertical component profiles

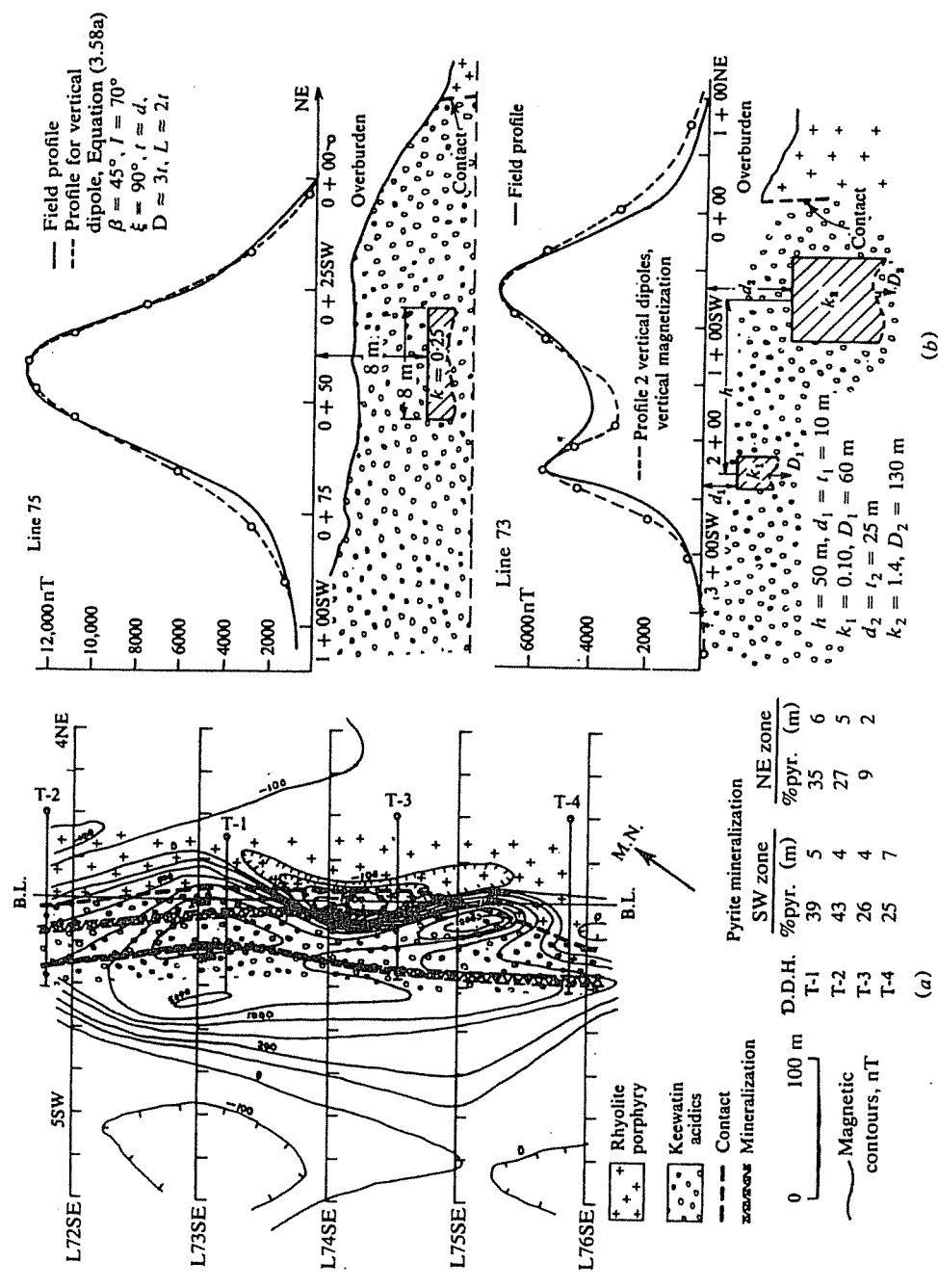


Figure 3.28. Ground magnetic survey over pyrite mineralization, Barraute, northwest Quebec. (a) Magnetic map.
 (b) Attempt to match profiles on lines 75SE and 73SE.

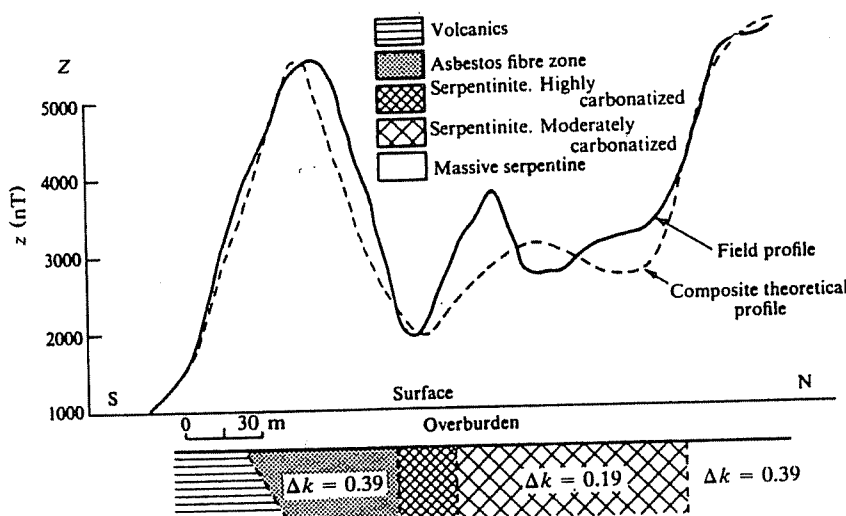


Figure 3.29. Vertical component ground magnetic profile in an area of asbestos mineralization near Matheson, Ontario.

normal to the strike of pyrite mineralization. There are two parallel pyrite zones in acidic flows, near a contact between the latter and rhyolite porphyry. Both have a strike length greater than 300 m and the zone nearer the contact appears to pinch out on line 75.

Although the pyrite mineralization is clearly associated with a magnetic trend in the area, the large magnetic anomalies on lines 73 and 75 could only be due to magnetite or possibly pyrrhotite, since the susceptibility of pyrite is relatively low (Table 3.1). However, there is no specific indication of these minerals in the drill logs of holes 1 to 4.

Because the overburden near the diamond drill holes was generally quite thick (25 m at T-1, for example), it was originally assumed to be at least 15 m throughout the grid. However, a shallow seismic refraction survey carried out later on line 75 showed bedrock only 1.5 to 3 m below the surface in the vicinity of the pyrite zones, dropping off abruptly to 15 to 25 m northeast of the acidic flow-rhyolite contact. Thus the magnetite sources may be very close to the surface and of small depth extent.

The source for the single 13 μT peak on line 75 appears to be a finite steeply dipping sheet at very shallow depth. Using Equation (3.58a) with $\beta = 45^\circ$, $I = 70^\circ$, $\xi = 90^\circ$, and $Z_e = 36 \mu\text{T}$, and fitting the profiles at three points (including the maximum), we obtain a reasonable fit with $t \approx d \approx 8 \text{ m}$, $D \approx 25 \text{ m}$, $2L \approx 30 \text{ m}$, and $k = 3 \text{ SI unit}$ (See Fig. 3.28b). However, when we try to match the double peak profile on line 73 by assuming two vertical sheets of identical cross section separated by 50 m and inductively magnetized in the earth's field, Equation (3.58a) produces the following parameters: $d \approx t = 2.5 \text{ m}$,

$D = 70 \text{ m}$, $2L = 90 \text{ m}$, $k_1 = 1.3 \text{ SI}$, and $k_2 = 1.9 \text{ SI}$. This results in a reasonable match of the central trough and the northeast flank, but the southwest flank is much too large. A better fit (shown in Fig. 3.28b) was obtained with the two vertical sheets illustrated, but the trough between them is too deep. Also, the depth extent must be less than 120 m because the bodies were not encountered in holes T-1 and T-3. Although this interpretation is certainly not definitive, it is clear that the magnetic sources are shallow, have limited strike length, steep dip, and large susceptibility contrast. This last fact indicates high magnetite content and possibly large remanence, which may be responsible for the disagreements (Green, 1960).

(2) The magnetic method is particularly useful in exploring for asbestos because of its occurrence in ultrabasic intrusive rocks rich in magnetite. When olivine (Mg_2SiO_4) is altered to serpentine ($\text{Mg}_3\text{SiO}_5(\text{OH})_4$) and magnesite (MgCO_3) by the addition of water and carbon dioxide, the asbestos is associated with high magnetic susceptibility and massive serpentinite. Figure 3.29 shows a vertical component profile over an asbestos prospect near Matheson in northern Ontario and the geologic section under a 15 m overburden. High magnetic responses correspond to the asbestos and massive serpentinite zones with lows over the volcanics and highly carbonized serpentine. A reasonable match to the field profile was obtained by assuming dikes of considerable depth extent using Equation (3.44a) with $r_2 \approx r_4$, $\phi_2 \approx \phi_4$, $\beta = \pi/2$, and all contacts vertical except the left one, which dips 30° . The presence of asbestos in the massive serpentinite zones can only be established by drilling.